

UNIVERSITY OF OKLAHOMA  
GRADUATE COLLEGE

REFORMULATION OF THE SOLUTION DIFFUSION THEORY OF OSN AND OSRO:  
INFLUENCE OF SORPTION, DIFFUSION, PRESSURE, INTERACTIONS AND SWELLING  
ON MEMBRANE PERFORMANCE

A THESIS  
SUBMITTED TO THE GRADUATE FACULTY  
in partial fulfillment of the requirements for the  
Degree of  
MASTER OF SCIENCE

By  
KELLY BYE  
Norman, Oklahoma

2021

REFORMULATION OF THE SOLUTION DIFFUSION THEORY OF OSN AND OSRO:  
INFLUENCE OF SORPTION, DIFFUSION, PRESSURE, INTERACTIONS AND SWELLING  
ON MEMBRANE PERFORMANCE

A THESIS APPROVED FOR THE DEPARTMENT OF CHEMICAL, BIOLOGICAL, AND  
MATERIALS ENGINEERING

BY THE COMMITTEE CONSISTING OF

Dr. Michele Galizia, Chair

Dr. Ngoc Bui

Dr. Dimitrios Papavassiliou

© Copyright by Kelly Bye 2021

All Rights Reserved

## ABSTRACT

Organic solvent nanofiltration (OSN) and organic solvent reverse osmosis (OSRO) have the potential to revolutionize the chemical industry if used in a widespread manner. Many researchers focus on developing new materials which surpass the upper bound, however little research is focused on understanding fundamental transport mechanisms behind OSN and OSRO. This paper analyzes the validity of the solution diffusion model to describe solvent transport through glassy polymers. Flux decline in glassy polymers is often attributed membrane compaction, which is commonly used as evidence that the pore flow model describes flow through glassy polymers. However, this paper demonstrates how the cause of flux decline is thermodynamic in origin using the NELF model, and cause by a limit in concentration gradient in the membrane being reached. The validity of this hypothesis is verified with a system of PTMSP and ethanol. The role of solvent concentration in membranes is often understated in the development of new materials. Molecular interactions play a significant role in sorption as well as overall concentration. Celazole PBI membranes were tested in a wide variety of solvents, resulting in a non-monotonous sorption trend with lower alcohols. Lower alcohols can form competitive hydrogen bonds with Celazole, causing plasticization. This leads to a significant reduction in Celazole's otherwise strong chemical, thermal, and physical properties. This finding is supported numerically through an analysis of the isosteric heat of sorption as well as in situ FTIR. These findings highlight the importance of testing materials in realistic conditions in order to determine their separations properties.

## TABLE OF CONTENTS

<b>Chapter 1: Introduction</b> .....	<b>1</b>
<b>Chapter 2: Theory</b> .....	<b>10</b>
2.1 Small Molecule Sorption in Glassy Polymers .....	10
2.2 Clustering .....	13
2.3 Small Molecule Diffusion in Polymers .....	13
2.4 Formulation of a Thermodynamic-Diffusion Model for OSN and OSRO .....	17
2.5 Equilibrium and Non-Equilibrium Lattice Fluid Models .....	21
<b>Chapter 3: Experimental</b> .....	<b>24</b>
3.1 Membrane Fabrication .....	24
3.2 Pure Fluid Sorption .....	25
3.3 Mixed Liquid Sorption .....	28
3.4 Polymer Dilation .....	28
3.5 Liquid Solvent Permeability .....	29
3.6 Vapor Sorption and Diffusion Measurements .....	29
3.7 Mechanical Properties Measurement .....	29
<b>Chapter 4: Results and Discussion</b> .....	<b>32</b>
<b>4.1 Formulation of the Solution Diffusion Theory: Analysis of Flux Decline</b> .....	<b>32</b>
4.1.1 Liquid Ethanol Sorption in PTMSP .....	32
4.1.2 Liquid Ethanol Diffusion Coefficient in PTMSP .....	38
4.1.3 Liquid Ethanol Permeability in PTMSP .....	41
<b>4.2 Role of Molecular Interactions on Celazole® Performance</b> .....	<b>44</b>
4.2.1 Pure Liquid Sorption .....	44
4.2.2 Polymer Dilation .....	48
4.2.3 Mixed Liquid Sorption .....	50
4.2.4 Methanol Vapor Sorption and Diffusion .....	53
4.2.5 Fractional Free Volume Analysis .....	62
4.2.6 Mechanical Properties .....	65

4.2.7 Methanol Sorption in PBI at Multiple Temperatures .....	67
4.2.8 Use of FTIR Spectroscopy to Shed Fundamental Details on the Mechanism of Plasticization in OSN Membranes .....	70
4.2.9 Sorption Equilibrium and Kinetics Obtained via FTIR Spectroscopy .....	72
4.2.10 Evolution of the PBI Spectrum During Methanol Sorption: Competitive Hydrogen Bonding Mechanism .....	78
<b>Chapter 5: Conclusions and Recommendations .....</b>	<b>84</b>
<b>Literature Cited .....</b>	<b>86</b>
<b>Appendices .....</b>	<b>99</b>
Supporting Information .....	99
Publications, Oral Presentations, Awards .....	111
VITA .....	112

## Chapter 1: Introduction

Membrane-based organic solvent separations have drawn interest in industrial applications for their potential to reduce the energy intensity of organic solvent separations. These separations are most often Organic Solvent Nanofiltration (OSN) or Organic Solvent Reverse Osmosis (OSRO), in which small molecules selectively permeate through membranes based on a combination of size sieving ability as well as thermodynamic interactions between the solvent and the polymer. As shown in Fig.1, OSN separates solvents from bulky solutes (typically 200 - 1000 Daltons in size), while OSRO separates similar molecules (50 – 200 Daltons in size), such as isomers [1].

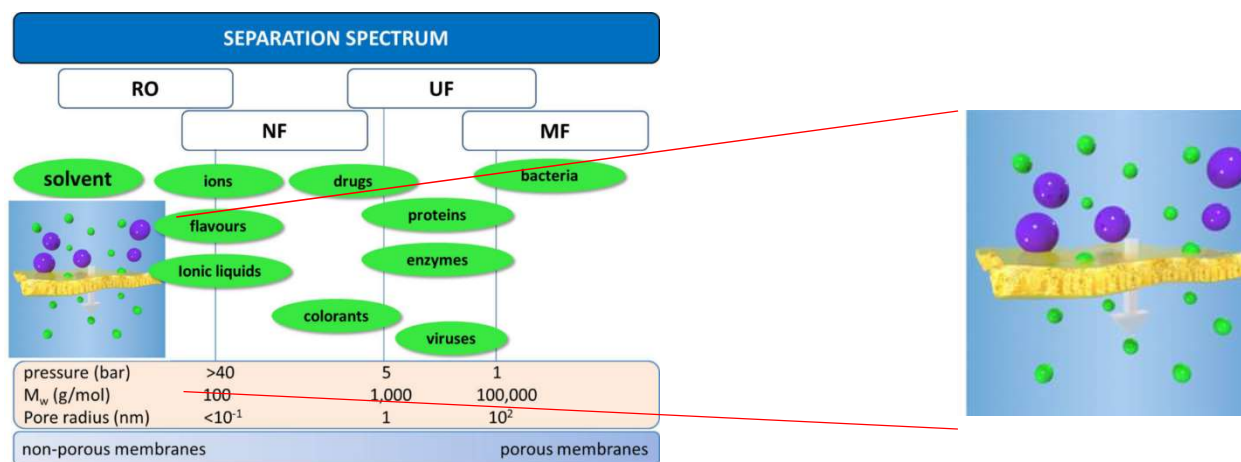


**Figure 1.** Separation spectrum for different types of membrane filtrations. From left to right, reverse osmosis, nanofiltration, ultrafiltration, microfiltration.

This chapter is re-adapted from:

Bye et al., Pure and mixed fluid sorption and transport in celazole<sup>®</sup> polybenzimidazole: Effect of plasticization, JMS, 235-247, volume 580, 2019, with permission of Elsevier

Bye, Galizia, Fundamental origin of flux-nonlinearity in organic solvent nanofiltration: Formulation of a thermodynamic/diffusion framework, JMS, volume 603, 2020, with permission of Elsevier

Loianno et al., Plasticization mechanism in polybenzimidazole membranes for organic solvent nanofiltration: Molecular insights from in situ FTIR spectroscopy, Journal of Polymer Science, 2547-2560, volume 58, issue 18, 2020 with permission of Wiley Online Library

The end goal of both of these separations is solute concentration and solvent recovery which account for 50-70% of the capital and operating costs in the chemical industry [2]. The over 40,000 distillation towers installed in the US to perform these separations consume 50% of the energy required by the American chemical industry [3, 4] and create environmental concerns, due to CO<sub>2</sub> emissions. The American chemical industry is responsible for 32% of the total energy consumption in the United States (see table 1) [4], so reducing energy requirements in the chemical industry is paramount to reducing the overall energy consumption of the United States.

**Table 1.** Energy consumption of different sectors of the United States (1 quad = 10<sup>15</sup> BTU) [4]

	Commercial	Transportation	Residential	<b>Industrial</b>
Percentage of Energy Consumption	19%	28%	21%	<b>32%</b>
Total Energy Consumption (Quads)	18.6	27.4	20.6	<b>31.4</b>

Membrane separations require significantly less energy and are a strong potential candidate for reducing or replacing distillation for solvent recovery and solute concentration. As highlighted in Fig. 2, concentrating one cubic meter of methanol by a factor of ten, requires two orders of magnitude less energy compared to distillation [1]. The potential scale of this energy reduction is highlighted by a recent report from the Environmental Protection Agency (EPA), which found that large scale use of membrane-based technologies would save annually 100 million tons of CO<sub>2</sub> emissions and \$4 billion in the US alone [5].



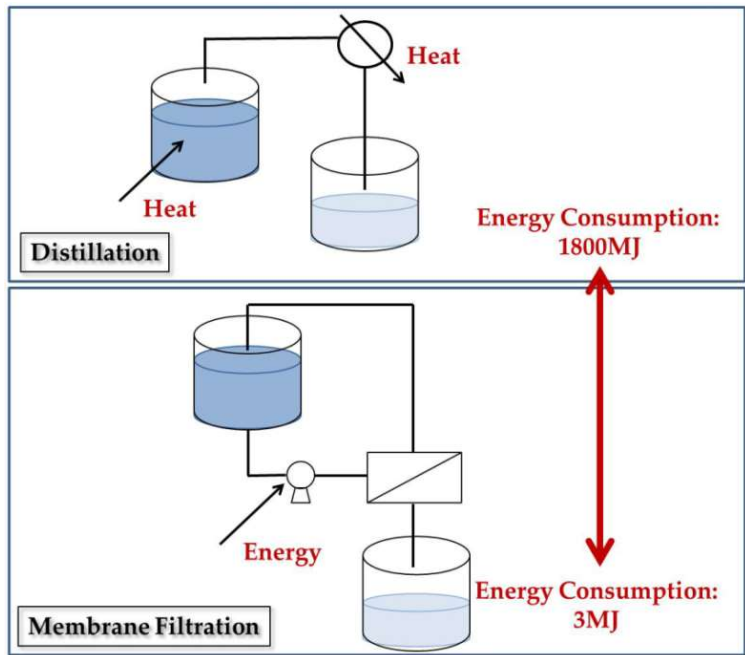


**Figure 2.** Energy consumption required to concentrate  $1 \text{ m}^3$  of methanol by a factor of ten via distillation and membrane filtration [1].

While promising as an alternative to distillation, membrane technology has major issues to overcome, including membrane material plasticization (cf. Fig. 3A), in which highly soluble penetrants cause excessive swelling of the polymer leading to a reduction in its separation efficiency, physical aging, that is, the collapse of non-equilibrium fractional free volume of glassy polymers over time (cf. Fig. 3B), and the limitation of the “upper bound” for permeability and selectivity (cf. Fig. 3C). The “upper bound” refers to a well-documented tradeoff between permeability and selectivity, the most famous example being reported as the Robeson upper bound for gas separation membranes [6]. The same trade-off has been reported, in more recent years, for organic solvent separations [7]. As membranes become more permeable, they tend to become less selective and vice versa. As a result, when selectivity is plotted against permeability, the membrane

performance is limited to below an upper bound. The goal of many researchers is focused on the synthesis and fabrication of materials which are both solvent resistant and capable of surpassing the upper bound. However, fundamental understanding of chemical and physical aspects that govern solvent and solute transport in OSN membranes remains entirely unexplored [5, 8-13]. This dissertation will explain how the solution-diffusion model can be formulated to fundamentally explain organic solvent transport through glassy polymers, and how the membrane productivity is affected by intermolecular interactions between the polymer and the penetrant. This fundamental analysis of membrane properties is essential to developing structure property correlations which, in turn, allow for the intelligent design of new membrane materials.

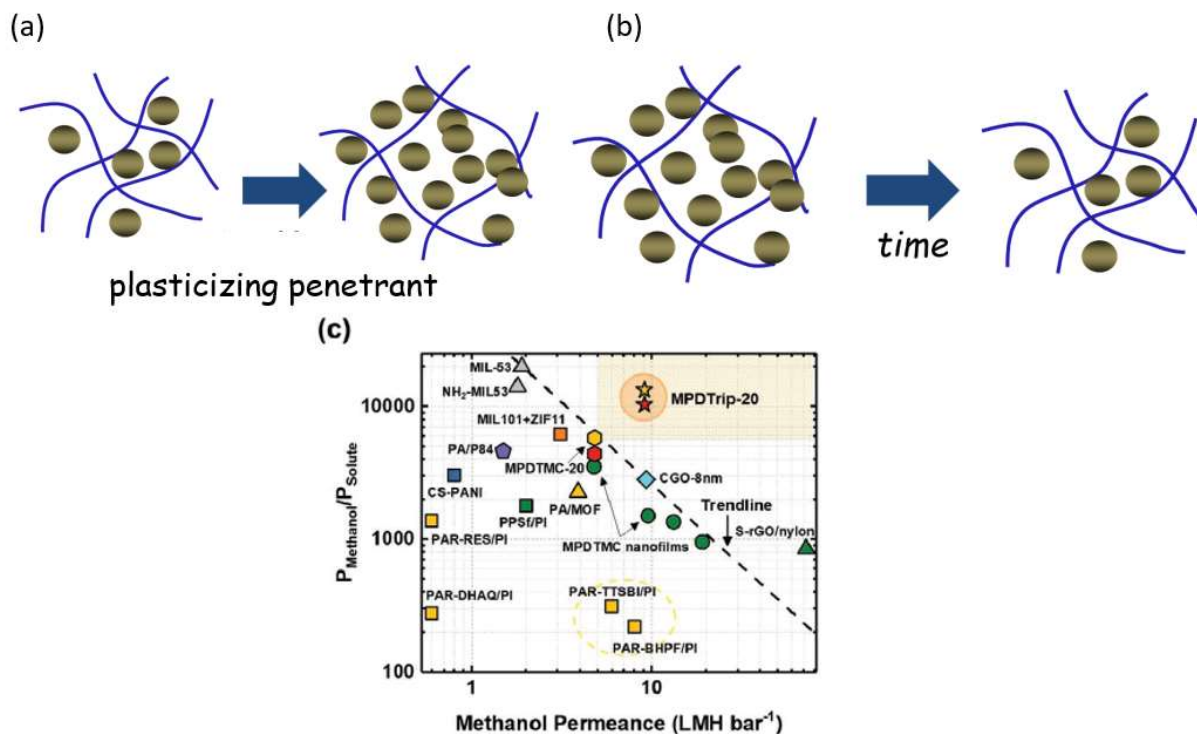


**Figure 3.** A) A penetrant plasticizing a polymer, causing the chains to spread apart resulting in greater permeability and reduced selectivity, B) A polymer experiencing physical aging, causing

*a collapse in the fractional free volume and a reduction in permeability, C) “Upper bound” example for a methanol/solute separation. Adapted from Pinnau et al. [7]*

The transport mechanism itself in OSN and OSRO membranes is poorly understood: some researchers have hypothesized a solution-diffusion mechanism [14-16], others a pore-flow mechanism [17, 18]. Finally, others have considered a combination of the previous two mechanisms [19, 20]. This confusion hinders the identification of the molecular factors that influence solvent flux and solute rejection. The nomenclature itself is somehow misleading. Indeed, while gas separation and water purification membranes are characterized in terms of permeability and selectivity [3], OSN and OSRO membranes are characterized in terms of solvent flux and solute rejection [7, 21]. The difference between the two nomenclatures is substantial, since permeability and selectivity are intrinsic membrane material properties, while flux and rejection are not [1, 3, 21]. This confusion comes from the fact that most of OSN research is performed using composite or asymmetric membranes (cf. Fig. 4), which makes impossible to deconvolute the properties of the active layer from those of the support.

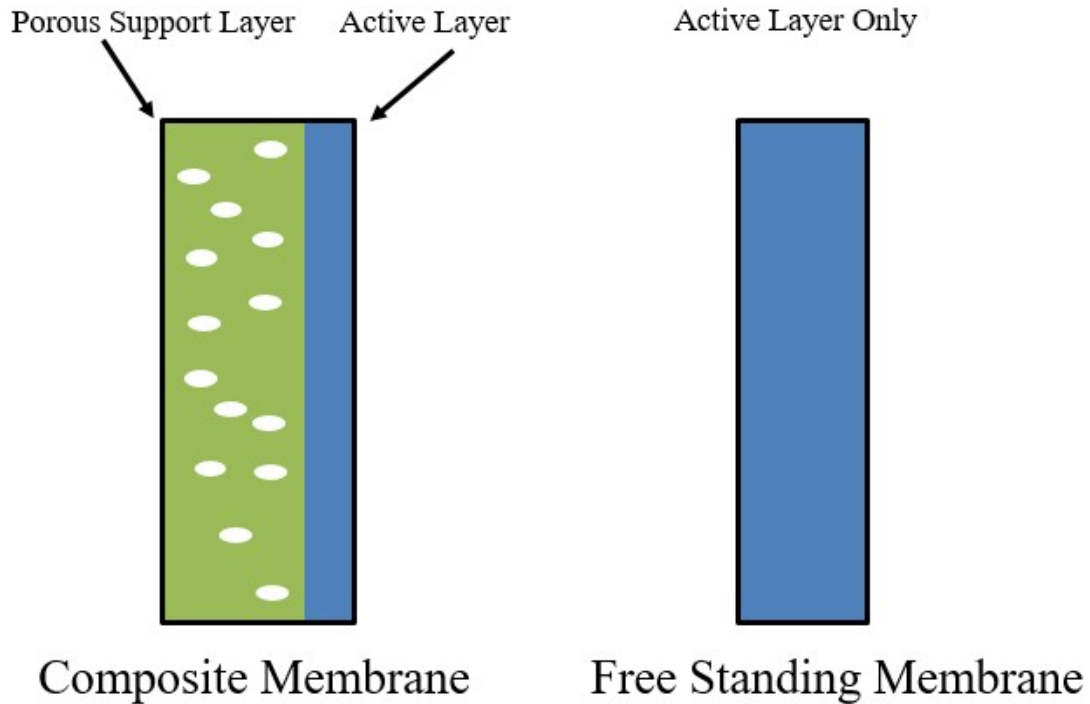


**Figure 4.** Composite Membrane vs. Free Standing Membrane schematic.

A peculiar feature of OSN is the flux non-linearity with  $\Delta p$  [22-27]. That is, a negative departure of flux from linearity is observed starting from  $\Delta p = 10/15$  atm, which makes the flux/pressure curve concave to the pressure axis. The molecular origin of this phenomenon has been the subject of a long-standing debate in the literature. Despite membrane mechanical compaction under pressure has been invoked to explain this phenomenon, this hypothesis has no quantitative support [22-24, 26, 27].

In this study, the hypothesis of membrane compaction is critically discussed, and a thermodynamic/diffusion framework is developed to demonstrate that flux vs.  $\Delta p$  non-linearity in OSN has a purely thermodynamic origin. Attributing flux non-linearity to membrane compaction implicitly assumes that the membrane is porous and that the transport mechanism is pore-flow. Indeed, membrane pores would be squeezed at high pressure, which would cause the observed

flux decline. However, the active layer of OSN membranes is dense, i.e., non-porous. It could be alternatively hypothesized that the porous material supporting the active layer undergoes compaction at high pressure. However, flux decline with  $\Delta p$  has been observed in free standing (i.e., support-free) dense films of PDMS [22-24, 26, 27], PTMSP and PIM-1 [28]. Therefore, the hypothesis of membrane compaction does not look convincing.

To shed fundamental light on flux non-linearity, the thermodynamic/transport framework originally developed by Paul in the early 70's to describe the pressure-driven mass transfer through swollen rubbery polymers has been generalized to glassy polymers, by replacing the Flory-Rehner model with the Non-Equilibrium lattice fluid theory, and used to describe solvent transport through OSN membranes in terms of the concentration gradient produced by the applied  $\Delta p$  [30-32]. The model has been validated using ethanol transport data through free-standing poly(trimethylsilyl propyne) (PTMSP) membranes. Equally important, this study demonstrates that, to be physically meaningful, solvent diffusion coefficients in OSN membranes must be corrected for the effects of the frame of reference (i.e., convective effects) and thermodynamic non-ideality. The latter represents a substantial difference with respect to gas separation membranes, where the frame of reference and non-ideal thermodynamic effects can be neglected without prejudicing the significance of the experimental findings [33, 34].

This study supports the hypothesis that the solution-diffusion model, if properly formulated, can successfully describe small molecule transport in OSN membranes, without the need to resort to the pore-flow model or more complicated transport mechanisms. Advancing fundamental understanding of OSN will lay the foundation for a more mature use of this process, and allow the most effective operative conditions to be set to maximize its productivity and efficiency.

In order to maximize membrane performance, researchers often develop membranes which greater fractional free volume in order to facilitate penetrant diffusion resulting in higher permeability. However, less attention has been paid to selectivity, which is believed to be controlled by the size-sieving effect (that is, by the diffusion contribution). A more careful analysis, however, shows that, in many cases, sorption-selectivity dominates over diffusion selectivity, an example being negative retention observed during the separation of non-polar solutes from polar solvents using PDMS, due to preferential solute sorption in the membrane [23]. The larger solute solubility relative to solvent solubility in the membrane was ascribed to the larger thermodynamic affinity of the former with PDMS. [23]. In many cases, these relevant chemical-physical phenomena are left completely unexplored. For this reason, it is essential to study the role of intermolecular interactions between the polymer and penetrant and how they affect the transport properties of the system.

In order to fundamentally analyze the role of intermolecular interactions on membrane performance in a wide variety of solvents, Celazole<sup>®</sup> PBI is used in this study due to its favorable chemical, physical, and thermal stability. It is commonly reported that tough polymers are more capable of withstanding chemically challenging environments than conventional glassy polymers, which make them promising candidates for OSN and OSRO. However, few studies report the effects of organic solvent sorption on the polymer structure [29, 30]. Sorption and dilation data in polymers for OSN application are rarely reported in the literature and the vast majority of them refer to rubbery PDMS [23, 29, 31-34]. In 2016, a collection of sorption and diffusion coefficients for several pure liquids in Matrimid<sup>®</sup> were reported by Stanford et al., however no fundamental interpretation was provided [35]. More recently, sorption data for several pure liquids in PDMS, polyimide P84, Matrimid<sup>®</sup>, polysulfone, perfluorinated co-polymers, and PIM-1 were reported by

Chau [2] and Ogieglo [36]. Ogieglo studied the sorption and swelling behavior of glassy and rubbery polymers as a function of time but, also in this case, no structure-property correlation was identified and discussed [36].

In this dissertation, we investigate pure and mixed liquid (aliphatic and aromatic hydrocarbons, alcohols, water, acetone) sorption in Celazole<sup>®</sup>, a commercial polybenzimidazole that is receiving attention for membrane separations in harsh environments. N-decane and PEG400 were considered to mimic common solutes used in the chemical industry. Interestingly, while exhibiting outstanding stability in aliphatic and aromatic hydrocarbons, Celazole<sup>®</sup> is plasticized by polar liquids. This behavior was explained based on favorable polymer-penetrant interactions. To shed more fundamental light on this aspect, methanol transport in Celazole<sup>®</sup> was investigated in the activity range 0-1 from 25 to 45 C. Since the experimental time scale is important to assess the transport properties of glassy polymers in the presence of swelling penetrants, Celazole<sup>®</sup> stability upon exposure to solvents was studied over a period up to 3 months. Additionally, FTIR spectroscopy in the transmission mode is used to provide a quantitative analysis of sorption, diffusion, swelling and molecular interactions in Celazole<sup>®</sup>. Specifically, this dissertation addresses the following questions: *i)* To what extent do polar liquids and their vapors plasticize Celazole<sup>®</sup>? *ii)* How does plasticization influence the sorption of solute/solvent mixtures in Celazole<sup>®</sup>? *iii)* Why do inter-chain hydrogen bonds not help prevent plasticization? *iv)* Which parameters affect solute and solvent sorption in Celazole<sup>®</sup>?

## Chapter 2: Theory

### 2.1 Small molecule sorption in glassy polymers.

There are at least two mechanisms to describe small molecules transport through solid materials, the solution diffusion model and the pore flow model (cf. Fig. x). The solution diffusion model describes transport through dense polymers which have no permanent pores. Molecules diffuse through transient gaps in the polymer. According to the solution-diffusion model, small molecule permeability coefficient in dense polymer membranes,  $P$ , is given by the product of the effective diffusion coefficient,  $\bar{D}$ , and the sorption coefficient,  $S$  [37, 38]:

$$P = \bar{D} \times S \quad (\text{Eq. 1})$$

The sorption coefficient,  $S$ , is defined as  $C/p$ , where  $C$  is the equilibrium penetrant concentration in the polymer, and  $p$  is the pressure. The pore flow model assumes the solvent flows through permanent pores in the membrane, and the flux can be calculated by the following equation:

$$n = \frac{d^2 \varepsilon \Delta p}{32 \eta \tau \ell} \quad (\text{Eq. 2})$$

where  $n$  is the flux through the membrane,  $d$  is the diameter of the pores of the membrane,  $\varepsilon$  is the porosity,  $\Delta p$  is the pressure difference across the membrane,  $\eta$  is the solvent viscosity,  $\tau$  is the tortuosity, and  $\ell$  is the membrane thickness. Due to flux decline observed at high pressures, some researchers claim that compaction causes membrane pores to be squeezed, resulting in a decrease in flux. However, this dissertation will call into question the assumption that membrane

This chapter is re-adapted from:

Bye et al., Pure and mixed fluid sorption and transport in celazole<sup>®</sup> polybenzimidazole: Effect of plasticization, JMS, 235-247, volume 580, 2019, with permission of Elsevier

Bye, Galizia, Fundamental origin of flux-nonlinearity in organic solvent nanofiltration: Formulation of a thermodynamic/diffusion framework, JMS, volume 603, 2020, with permission of Elsevier

Loianno et al., Plasticization mechanism in polybenzimidazole membranes for organic solvent nanofiltration: Molecular insights from in situ FTIR spectroscopy, Journal of Polymer Science, 2547-2560, volume 58, issue 18, 2020 with permission of Wiley Online Library



compaction is responsible for flux decline in glassy polymers and show how the solution diffusion model can describe flux decline via a thermodynamic explanation.

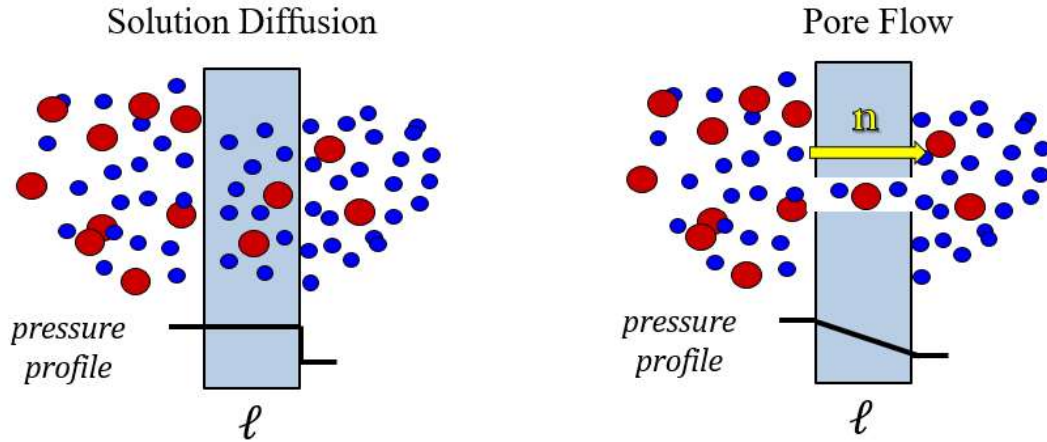


**Figure 5.** Solution diffusion and pore flow schematics. The solution diffusion mechanism explains diffusion through transient gaps in the polymer while pore flow describes flow through permanent pores.

Permeability is experimentally measured as the pressure and thickness normalized flux [39]:

$$P = \frac{n_i}{\frac{\Delta P}{\ell}} \quad (\text{Eq. 3})$$

where  $n_i$  is the steady-state flux with respect to the fixed frame of reference (i.e., with respect to the membrane), that is, the experimentally measured flux. Permeance is the pressure (but not thickness) normalized flux:

$$P = \frac{n_i}{\Delta P} \quad (\text{Eq. 4})$$

Permeance is not a membrane material property since it depends on the thickness of the membrane being tested, while permeability is a characteristic of a membrane material regardless of membrane thickness. For this reason, in order to understand material properties, it is essential

to report permeability instead of permeance. Selectivity is reported as the ratio between the permeability or permeance of the solvent to the solute.

$$\alpha_{ij} = \frac{P_i}{P_j} \quad (\text{Eq. 5})$$

Where  $\alpha_{ij}$  is the selectivity of component i to component j and. By plugging eq. 1 into eq. 5, the selectivity can be deconvoluted into the solubility selectivity and the diffusion selectivity, or the ratio of the sorption coefficients and the ratio of the diffusion coefficients.

$$\alpha_{ij} = \frac{S_i}{S_j} * \frac{D_i}{D_j} \quad (\text{Eq. 6})$$

This deconvolution allows the thermodynamic and entropic contributions to selectivity be determined in order to analyze selectivity at a more fundamental level.

Sorption of gas and vapors in glassy polymer membranes is described via the dual mode model [40, 41], based on which small molecules can sorb in either the excess free volume (Langmuir sorption) or the dense phase (Henry's mode sorption) of the polymer, according to the equation:

$$C = k_D p + \frac{C'_H b p}{1 + b p} \quad (\text{Eq. 7})$$

where  $C$  is the penetrant concentration in the polymer,  $k_D$  is Henry's constant for penetrant dissolution in the dense, equilibrium polymer phase,  $C'_H$  is the Langmuir sorption capacity, and  $b$  is the Langmuir affinity parameter, which measures the affinity of the penetrant to the Langmuir sites.

The solubility coefficient exhibits an van't Hoff-type dependence on temperature [37]:

$$S = S_0 \exp\left(\frac{-\Delta H_S}{RT}\right) \quad (\text{Eq. 8})$$

where  $S_0$  is the pre-exponential constant, and  $\Delta H_S$  is the heat of sorption. The heat of sorption is the sum of the enthalpy of penetrant condensation ( $\Delta H_{cond}$ ) and the enthalpy of mixing of the penetrant and polymer ( $\Delta H_{mix}$ ).  $\Delta H_{mix}$  accounts for the polymer-penetrant interactions and the

energy required to spread apart polymer chains and open molecular scale gaps to accommodate penetrant molecules [35]. The isosteric heat of sorption, which provides the concentration dependence of sorption enthalpy, is defined as follows [40]:

$$\left[ \frac{\partial \ln p}{\partial \left( \frac{1}{T} \right)} \right]_C = \frac{\Delta H_s}{R} \quad (\text{Eq. 9})$$

where  $p$  is the pressure corresponding at each concentration,  $C$ .

*2.2 Clustering.* Zimm and Lundberg developed a very simple approach to address the issue of penetrant clustering in polymer-penetrant systems [42], which is based on the analysis of sorption data. The Zimm-Lundberg approach relies on the following equation:

$$\frac{G_{11}}{\bar{V}_1} = (\phi_1 - 1) \left[ \frac{\partial \left( \frac{a}{\phi_1} \right)}{\partial a} \right]_{T,p} - 1 \quad (\text{Eq. 10})$$

where  $G_{11}$  is the so-called clustering integral,  $\phi_1$  is the penetrant volume fraction,  $\bar{V}_1$  is the penetrant partial molar volume and  $a$  is the penetrant activity in the external vapor phase. The quantity  $\phi_1 \frac{G_{11}}{\bar{V}_1}$  provides the number of vapor molecules in the cluster in excess to a single molecule. Accordingly, penetrant clustering takes place if the quantity  $\phi_1 \frac{G_{11}}{\bar{V}_1}$  is positive [42, 43].

*2.3 Small molecule diffusion in polymers.* Small molecule diffusion coefficients in polymers can be determined from the analysis of experimental sorption kinetics. Specifically, the normalized mass uptake is plotted as a function of time as follows [44]:

$$\frac{M_t - M_0}{M_\infty - M_0} = kt^n \quad (\text{Eq. 11})$$

where  $M_t$  is the sample mass at time  $t$ ,  $M_0$  is the sample mass at time 0, i.e., at the beginning of the experiment, and  $M_\infty$  is the mass of the sample at the end of the experiment. Fickian behavior

is observed when the normalized mass uptake is linear with the square root of time, i.e., when  $n = 0.5$  [44]. However, diffusion of condensable vapors and liquids in glassy polymers is often accompanied by matrix relaxation [44-46]. In some cases, a pseudo-Fickian behavior is observed at short times, followed by a slow relaxation at long times. Berens and Hopfenberg demonstrated that, in the latter situation, the overall sorption kinetics can be described using a linear superimposition of Fickian diffusion and relaxation diffusion [44]:

$$M_t = M_{F,t} + M_{R,t} \quad (\text{Eq. 12})$$

where  $M_{F,t}$  and  $M_{R,t}$  represent the sorption associated to Fickian diffusion and polymer relaxation, respectively. When the barometric (i.e., pressure decay) technique is used to measure vapor sorption, the dimensionless absorbed mass can be expressed as follows [44, 45]:

$$\frac{M_t}{M_\infty} = g_F \left[ 1 - \sum_{n=1}^{\infty} \frac{2\Omega(1+\Omega)}{q_n^2\Omega^2 + \Omega + 1} \exp\left(-\frac{\bar{D}q_n^2 t}{\ell^2}\right) \right] + (1-g_F) \left[ 1 - \exp\left(-\frac{t}{\tau}\right) \right] \quad (\text{Eq. 13})$$

where  $g_F$  is the fraction of penetrant absorbed by pure diffusion and  $1 - g_F$  is the remaining fraction of penetrant absorbed during the relaxation stage. In Eq. 13,  $\Omega$  is the ratio between the volume of the vapor in equilibrium with the membrane and the volume of the membrane itself, corrected for the partition coefficient [45, 47]. Such correction accounts for changes in the interfacial concentration due to vapor sorption in the membrane. Finally,  $\ell$  is the membrane semi-thickness,  $q_n$  are the positive, non-zero solutions of the equation  $\tan(q_n) = -\Omega q_n$  [45], and  $\tau$  is the characteristic relaxation time.

When considering the transport of a pure species  $i$  through a polymer membrane, the steady-state flux with respect to the fixed frame of reference (i.e., the membrane),  $n_i$ , and the diffusive flux with respect to the center of mass of the polymer-penetrant system,  $j_i$ , are related as follows [1, 33, 38, 48]:

$$n_i = j_i + \omega_i n_i \quad (\text{Eq. 14})$$

where  $\omega_i$  is the penetrant mass fraction in the membrane. Therefore, the penetrant flux with respect to the fixed frame is the sum of the diffusive flux with respect to the center of mass (i.e.,  $j_i$ ), and the convective flux due to the bulk penetrant motion (i.e.,  $\omega_i n_i$ ). Eq. 14 satisfies the condition that the membrane flux is zero at steady-state. If diffusion occurs in the thickness direction only (i.e.,  $\bar{x}$ ), the Fick's law provides the following expression for  $j_i$  [39]:

$$j_i = -\rho D_i \frac{d\omega_i}{dx} \quad (\text{Eq. 15})$$

where  $\rho$  is the density of the membrane/solvent mixture,  $\frac{d\omega_i}{dx}$  is the concentration gradient across the membrane, and  $D_i$  is the local effective mutual diffusion coefficient.  $D_i$  represents an effective value because it inherently contains non-ideal thermodynamic effects. At steady-state,  $\frac{d\omega_i}{dx} = \frac{\omega_{i,\ell}^m - \omega_{i,0}^m}{\ell}$ , where  $\omega_{i,\ell}^m$  and  $\omega_{i,0}^m$  are the mass fractions of species  $i$  in the downstream (i.e., at  $x = \ell$ ) and upstream (i.e., at  $x = 0$ ) membrane side, respectively. Superscript  $m$  stands for the membrane phase. Plugging Eq. 15 into Eq. 14 provides the following expression for penetrant flux with respect to the fixed frame [32, 39]:

$$n_i = -\frac{\rho D_i}{1 - \omega_i} \frac{d\omega_i}{dx} \quad (\text{Eq. 16})$$

When considering gas or vapor diffusion in polymers,  $\omega_i$  is numerically negligible ( $\ll 0.1$ ), therefore Eq. 16 is written by assuming  $\omega_i \cong 0$ , which implies that  $n_i \cong j_i$ . However, in the case of organic liquid transport in polymers,  $\omega_i$  can be very high, so the assumption  $n_i \cong j_i$  is no longer valid. Assuming  $n_i \cong j_i$  provides unrealistic values of diffusion coefficients, which has led several researchers to conclude that small molecule transport in OSN membranes occurs by pore flow

[18]. Analytical integration of Eq. 16 provides the following expression for the penetrant flux [29, 32]:

$$n_i \ell = \rho \bar{D}_i \ln \left( \frac{1 - \omega_{i,\ell}}{1 - \omega_{i,0}} \right) \quad (\text{Eq. 17})$$

where  $\bar{D}_i$  is the effective, concentration-averaged diffusion coefficient, which is defined as follows [49]:

$$\bar{D}_i = \frac{1}{\omega_{i,\ell}^m - \omega_{i,0}^m} \int_{\omega_{i,0}^m}^{\omega_{i,\ell}^m} \frac{D_i}{1 - \omega_i} d\omega_i^m \quad (\text{Eq. 18})$$

The penetrant chemical potential difference between the external fluid phase and the membrane phase is the actual driving force for penetrant transport [45, 50]. However, since concentration is easier to measure than chemical potential, the penetrant concentration difference across the membrane is usually assumed as the driving force in the Fick's law. In the latter situation, the diffusion coefficient appearing in Eq. 17,  $\bar{D}$ , is the product of a mobility coefficient,  $L$ , which is a purely kinetic parameter related to the frictional resistance offered by the polymer to penetrant diffusion, and a thermodynamic factor,  $\alpha$ , which is related to polymer-penetrant interactions [45, 50]. When polymer-penetrant mixing is ideal,  $\alpha$  is equal to one, so the measured diffusion coefficient does not need any correction for thermodynamic non-ideality [45, 50]. When polymer-penetrant mixing is non-ideal,  $\alpha$  can be either greater than 1, when polymer-penetrant interactions are thermodynamically favorable (i.e., attractive), or less than 1 when polymer-penetrant interactions are thermodynamically unfavorable (i.e., repulsive). The thermodynamically corrected diffusion coefficient or mobility,  $L$ , can be calculated as follows [45, 50]:

$$L = \frac{\bar{D}}{\alpha} = \bar{D} \frac{\partial \ln(\omega_{pen})}{\partial \ln(a)} \quad (\text{Eq. 19})$$

where  $\omega_{pen}$  is the penetrant mass fraction in the polymer, which is known from sorption measurements, and  $a$  is the penetrant activity. The thermodynamic factor,  $\alpha$ , can be calculated directly from the experimental sorption data (i.e.,  $\alpha = \frac{\partial \ln(a)}{\partial \ln(\omega_{pen})}$ ). Alternatively, the dual mode

model provides the following analytic expression for  $\alpha$  [51]:

$$\alpha = \left( \frac{k_D + \frac{C_H b}{1+bp}}{k_D + \frac{C_H b}{(1+bp)^2}} \right) \left[ 1 + \frac{M_{w1}}{22,414 \rho_p} \left( k_D p + \frac{C_H bp}{1+bp} \right) \right] \quad (\text{Eq. 20})$$

where  $M_{w1}$  is the penetrant molar mass and  $\rho_p$  is the polymer density.

To apply Eq. 13 to *time-resolved* FTIR measurements, the Lambert-Beer law is used to correlate the penetrant uptake with the absorbance as follows [52]:

$$\frac{M(t)}{M_\infty} = \frac{A(t)L_\infty}{A_\infty L(t)} \quad (\text{Eq. 21})$$

If the sample thickness changes little during the sorption experiment ( $\leq 3\%$ ), the mass ratio in Eq. 13 can be considered equivalent to the absorbance ratio.

*2.4 Formulation of a thermodynamic-diffusion model for OSN and OSRO.* The starting point in this study is the generalization of the thermodynamic theory of penetrant transport in swollen rubbery polymers, originally developed by Paul in the early '70s, to glassy polymers typically used in OSN [29-32]. Let us consider an isothermal dead-end filtration experiment, where a polymer membrane, whose thickness is  $\ell$ , separates two solutions (cf. Fig. 4). The upstream membrane face (at  $x = 0$ ) contacts the feed, and the downstream membrane face (at  $x = \ell$ ) contacts the permeate. We assume that the solution-diffusion model governs small molecule transport in the membrane, therefore the pressure profile throughout the membrane is uniform and it is equal to the feed

pressure, while the permeate is at atmospheric pressure [29, 39]. The pressure, chemical potential and concentration profiles of the species  $i$  through the membrane are shown in Fig. 4.

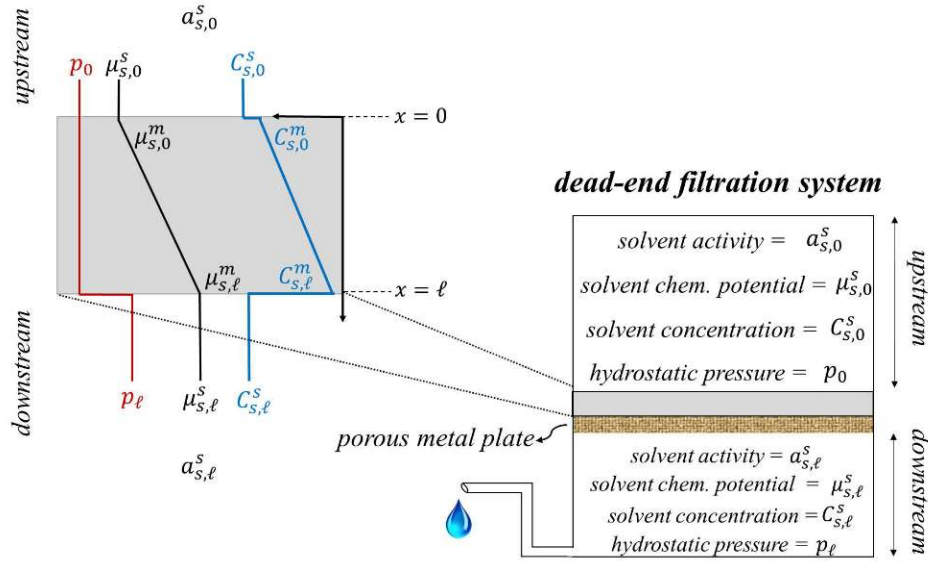


**Figure 6.** Pressure, chemical potential and concentration profile in a dense OSN polymer membrane.

The chemical potential of species  $i$  in the feed solution,  $\mu_{i,0}^s$ , and in the permeate,  $\mu_{i,\ell}^s$ , is expressed in terms of activity as follows [29]:

$$\mu_{i,0}^s = \mu_{i,ref} + RT \ln a_{i,0}^s + \tilde{V}_i (p_0 - p_{ref}) \quad (\text{Eq. 22})$$

$$\mu_{i,\ell}^s = \mu_{i,ref} + RT \ln a_{i,\ell}^s + \tilde{V}_i (p_\ell - p_{ref}) \quad (\text{Eq. 23})$$

where the properties of the upstream and downstream solutions are assumed to be spatially uniform. In Eqs. 22-23,  $\mu_{i,ref}$  represents the chemical potential of pure component  $i$  at the reference pressure,  $p_{ref}$ , subscripts 0 and  $\ell$  represent the upstream and downstream membrane sides, respectively, and superscripts  $s$  and  $m$  indicate the solution and the membrane phase, respectively. Finally,  $a_i$  and  $\tilde{V}_i$  are the activity and molar volume of species  $i$ , respectively. The



advantage for using Eqs. 22-23 is that the pressure dependence of chemical potential is lumped in the terms  $\tilde{V}_i(p_0 - p_{ref})$  and  $\tilde{V}_i(p_\ell - p_{ref})$ , while activity depends on concentration only. The chemical potential of species  $i$  in the upstream membrane face,  $\mu_{i,0}^m$ , and downstream membrane face,  $\mu_{i,\ell}^m$ , are given by [29]:

$$\mu_{i,0}^m = \mu_{i,ref} + RT \ln a_{i,0}^m + \bar{V}_i(p_0 - p_{ref}) \quad (\text{Eq. 24})$$

$$\mu_{i,\ell}^m = \mu_{i,ref} + RT \ln a_{i,\ell}^m + \bar{V}_i(p_\ell - p_{ref}) \quad (\text{Eq. 25})$$

where  $\bar{V}_i$  is the penetrant partial molar volume in the membrane. Despite  $\bar{V}_i$  can be a little different from the pure penetrant molar volume (i.e.,  $\tilde{V}_i$ ), for the sake of simplicity we assume that  $\bar{V}_i = \tilde{V}_i$ .

This assumption relies on the relatively small dilation experienced by PTMSP in liquid ethanol (

$\frac{\Delta \ell}{\ell_0} \approx 12\%$ ), i.e., on the small volume change upon penetrant/polymer mixing. The assumption of

$\bar{V}_i = \tilde{V}_i$  has been used to describe liquid sorption in rubbery polymers, which exhibit much large swelling upon exposure to organic liquids.

Since equilibrium conditions must exist at the interface between the membrane and the adjacent solution at  $x = 0$  and  $x = \ell$ , the following conditions must be satisfied:

$$\mu_{i,0}^m = \mu_{i,0}^s \quad (\text{Eq. 26})$$

$$\mu_{i,\ell}^m = \mu_{i,\ell}^s \quad (\text{Eq. 27})$$

From Eqs. 22, 24 and 26, it follows that:

$$a_{i,0}^m = a_{i,0}^s \quad (\text{Eq. 28})$$

which means that a change in the upstream pressure does not change the activity of component  $i$  in the upstream membrane face. From Eqs. 23, 25 and 27, it follows that [29]:

$$a_{i,\ell}^m = a_{i,\ell}^s \exp\left[-\frac{\tilde{V}_i(p_0 - p_\ell)}{RT}\right] \quad (\text{Eq. 29})$$

which indicates that any increase in the upstream pressure causes a decrease in the activity of component  $i$  in the downstream membrane face. Obviously,  $a_{i,\ell}^s = 1$  when the permeation of a pure liquid is considered. When the pressure difference across the membrane is zero, Eq. 29 degenerates in the well-known equilibrium condition  $a_{i,\ell}^m = a_{i,\ell}^s$ . Eqs. 28 and 29 are of general validity, irrespective of the glassy or rubbery nature of the membrane, and represent the central point in the Paul theory. Paul used the Flory-Rehner theory to relate the activity to the concentration of species  $i$  in the upstream and downstream membrane faces [53]. However, the Flory-Rehner theory is valid for rubbery systems only, and it cannot be used to connect activity to concentration in the case of glassy polymers. In this paper, the core thermodynamic relations developed by Paul (i.e., Eqs. 28-29) will be generalized to virtually any polymer by replacing the Flory-Rehner theory with the lattice fluid theory [54-56]. Besides being grounded on more rigorous molecular basis, the lattice fluid theory works for both rubbery and glassy polymers, via the Sanchez-Lacombe equation of state (SLEoS) [54, 55] and the NELF model [56], respectively. Since at any given activity corresponds one and just one concentration, Eqs. 28-29 imply that any increase in the upstream pressure does not influence the concentration of the species  $i$  in the upstream membrane face, while it causes a decrease in the concentration of species  $i$  in the downstream membrane face [29]. Therefore, a  $\Delta p$  must exist at which the solvent concentration in the downstream membrane side becomes zero. According to the Fick's law, in this condition the maximum driving force for penetrant transport is attained, therefore a ceiling flux must exist. This conclusion implies that flux, which is initially a linear function of  $\Delta p$ , must gradually decline with increasing  $\Delta p$  to reach its final ceiling value. On this basis, membrane compaction does not seem

a convincing motivation to explain the flux vs  $\Delta p$  non-linearity. The underlying hypothesis of this approach is that flux decline with  $\Delta p$  is only caused by the concentration gradient across the membrane. However, based on the Fick's law, flux decline might also be caused by a decrease of diffusion coefficient with pressure. To shed fundamental light on this aspect, the solvent diffusion coefficient in the membrane will be determined as a function of  $\Delta p$ .

*2.5 Equilibrium and non-equilibrium Lattice Fluid models.* The Sanchez-Lacombe lattice fluid theory [54, 55] generalizes the Flory's model by introducing the lattice compressibility [53]. Specifically, mixtures of rubbery polymers with small molecules are envisaged as a three-dimensional lattice, where each lattice's site is occupied by a small molecule. Polymer chains are assumed as a sequence of rigid beads, each of which occupies a lattice's site. Finally, the model admits the existence of empty sites, which guarantees the lattice's compressibility. The model requires only three input parameters to predict the thermodynamic properties of polymer-containing mixtures, namely the characteristic temperature ( $T_i^*$ ), pressure ( $p_i^*$ ), and density ( $\rho_i^*$ ) of each species [54, 55].  $T_i^*$ ,  $p_i^*$  and  $\rho_i^*$  are estimated by fitting experimental pVT data for the pure component to the Sanchez-Lacombe equation of state (SLEoS). The mixture characteristic parameters are determined using appropriate mixing rules. In doing so, the validity of the Hildebrand rule is assumed, i.e., penetrant-penetrant mean field self-interactions are assumed energetically equivalent to polymer-polymer self-interactions and penetrant-polymer mutual interactions. When mutual mean field interactions deviate from the Hildebrand rule, an adjustable parameter, namely the binary interaction parameter ( $k_{ij}$ ), is introduced [45, 57, 58]. For mixtures that follow the Hildebrand rule,  $k_{ij} = 0$ . When  $k_{ij} > 0$ , mutual (i.e., polymer-penetrant) interactions are less favorable than self-interactions (i.e., penetrant-penetrant and polymer-polymer interactions). In contrast, when  $k_{ij} < 0$ , mutual interactions are more energetically favorable than

self-interactions. The advantage for using the lattice fluid theory is that the binary parameter,  $k_{ij}$ , does not depend on composition, temperature and pressure [57, 60]. In contrast, the Flory-Hugging interaction parameter,  $\chi$ , exhibits a complex dependence on temperature and composition, which introduces additional adjustable parameters [49, 60].

Finally, the density of a rubbery polymer-penetrant mixture is calculated, at any temperature and composition, via the Sanchez-Lacombe equation of state (SLEoS), without the need for additional experimental information [58, 59].

The framework developed by Sanchez and co-workers cannot be used to predict thermodynamic properties of mixtures containing glassy polymers. Since the latter are non-equilibrium materials, the non-equilibrium lattice fluid (NELF) model must be used to connect activity to concentration [56]. The sole difference relative to the case of rubbery polymers is that the glassy polymer density cannot be calculated via the SLEoS, but it has to be known experimentally. The density of a swollen glassy polymer can be estimated from its dry density,  $\rho_{pol,0}$ , and experimental dilation data,  $\frac{\Delta V}{V_0}$ , as follows:

$$\rho_{pol} = \rho_{pol,0} \left( \frac{1}{1 + \frac{\Delta V}{V_0}} \right) \quad (\text{Eq. 30})$$

To reduce the amount of experimental input, in the NELF model the dilation is assumed to be a linear function of pressure or activity [45]:

$$\rho_{pol} = \rho_{pol,0} (1 - k_{sw} p) \quad (\text{Eq. 31})$$

where  $k_{sw}$  is the swelling coefficient. When considering organic species sorption in glassy polymers, however, Eq. 31 may underestimate the polymer swelling at activity 1, due to non-linearity of density as a function of pressure, which leads to underestimate liquid sorption.

Moreover, when considering the sorption of associating penetrants, such as alcohols, the NELF model is not able to account for penetrant clustering, which, like swelling, produces a well detectable upturn in the experimental sorption isotherm at activity close to 1 [45]. In the latter situation,  $k_{sw}$  lumps together the effects of swelling and clustering, therefore it represents an apparent swelling coefficient (cf. section 4.1) [45].

To summarize,  $\omega_{i,0}^m$  (i.e., the concentration,  $C_{i,0}^m$ ) and  $\omega_{i,\ell}^m$  (i.e.,  $C_{i,\ell}^m$ ) can be predicted as follows:

- At any  $(p_0 - p_\ell)$  values, and at fixed temperature,  $\omega_{i,0}^m$  is obtained directly from the SLEoS if the polymer is rubbery or it turns rubbery upon exposure to the liquid penetrant. The sole adjustable parameter is the binary polymer-penetrant interaction parameter,  $k_{ij}$ , which can be fit directly to the experimental liquid solubility. If liquid sorption is not experimentally available,  $k_{ij}$  can be fit to vapor sorption data at activity less than 1. If the membrane is glassy and it remains glassy upon exposure to the solvent, the SLEoS must be replaced with the NELF model. At any  $(p_0 - p_\ell)$  values, and at fixed temperature,  $\omega_{i,0}^m$  is calculated by entering the actual polymer density, which has to be known experimentally (from dilation measurements), and by adjusting the  $k_{ij}$  parameter to vapor sorption data, as described in the case of rubbery polymers.
- At any  $(p_0 - p_\ell)$  values, the corresponding activity at the downstream membrane face,  $a_{i,\ell}^m$ , is calculated through Eq. 29, regardless the membrane is rubbery or glassy. Since in this study we consider pure fluid transport only, in Eq. 29  $a_{i,\ell}^s$  is equal to 1. Once  $a_{i,\ell}^m$  is known, the corresponding  $\omega_{i,\ell}^m$  value is calculated from the SLEoS or the NELF model, following the same approach as for  $\omega_{i,0}^m$ .

## Chapter 3: Experimental

*3.1 Membrane Fabrication.* For Celazole<sup>®</sup> PBI (polybenzimidazole) membrane fabrication, dope solution containing 26 wt% PBI, 1.5 wt% LiCl, and 72.5 wt% dimethylacetamide (DMAc) was purchased from PBI Performance Products Inc. (Charlotte, NC). The as received dope solution was diluted with DMAc (Alfa Aesar, Haverhill, MA) to produce a 5 wt% solution of PBI and cast onto a clean Petri dish. The nascent membrane was placed into a vacuum oven and dried at room temperature under full vacuum. After 24 hours, the temperature in the oven was raised to 80°C for 4 hours, and finally to 100°C for 1 hour. The membrane was then soaked in deionized water for 24 hours to remove lithium chloride. Finally, the membrane was blotted with a clean paper, sandwiched between two quartz plates separated by spacers and dried at 140°C for 24 hours under vacuum, to remove water and any other remaining solvent. The quartz plates help prevent the membrane from curling. Complete solvent removal was verified by TGA with mass spectrometry analysis. Membranes for sorption and dilation experiments with organic liquids and water were about 120-150  $\mu\text{m}$  thick. Membranes for vapor sorption experiments were about 20  $\mu\text{m}$  thick. For PTMSP membrane fabrication, PTMSP powders (*Gelest Inc, Morrisville, PA*) were dissolved in toluene (*Alfa Aesar, Haverhill MA*) to prepare a 1 wt% solution. After stirring for overnight at ambient temperature, the PTMSP solution was cast into a glass ring caulked to a flat glass plate,

This chapter is re-adapted from:

Bye et al., Pure and mixed fluid sorption and transport in celazole<sup>®</sup> polybenzimidazole: Effect of plasticization, *JMS*, 235-247, volume 580, 2019, with permission of Elsevier

Bye, Galizia, Fundamental origin of flux-nonlinearity in organic solvent nanofiltration: Formulation of a thermodynamic/diffusion framework, *JMS*, volume 603, 2020, with permission of Elsevier

Loianno et al., Plasticization mechanism in polybenzimidazole membranes for organic solvent nanofiltration: Molecular insights from in situ FTIR spectroscopy, *Journal of Polymer Science*, 2547-2560, volume 58, issue 18, 2020 with permission of Wiley Online Library

to fabricate a dense, flat membrane. The amount of solution poured into the ring varied depending on desired membrane thickness (typically 50 mL, resulting in a film about 125  $\mu\text{m}$  thick). The nascent membrane was covered with an aluminum foil with small holes poked through, to allow slow toluene evaporation, and placed under a fume hood for 24 hours. After toluene was completely evaporated, the membrane was peeled off the dish by soaking it in de-ionized water for a few minutes. Following this procedure, the membrane was blotted, sandwiched between two quartz plates to prevent curling, and placed under vacuum at room temperature for 3 hours to remove any residual toluene and water. To prevent physical aging effects, sorption/permeation experiments were run immediately. Organic liquids for sorption experiments were purchased from Alfa Aesar with different degrees of purity (always higher than 98%).

### *3.2 Pure Fluid Sorption.*

Pure liquid sorption experiments were performed at 25°C. Each membrane was cut into 5x2 cm strips. Small glass jars were filled with different pure liquids (in the case of PTMSP, only ethanol was used) and 2-3 membrane strips were placed inside. During the experiments, the jars were stored in a thermostatic bath, whose temperature was kept constant to within  $\pm 0.1^\circ\text{C}$ . At regular time intervals, the membranes were removed from the solvents and rapidly blotted using laboratory wipes, to remove the excess liquid. The blotting and weighing process was very fast ( $\cong 20$  s), to minimize any evaporative solvent loss. Each membrane was weighed using an analytical balance (Mettler Toledo, model ME54TE, full scale 52 g, resolution 0.1 mg). To evaluate the extent of evaporation rate and its impact on sorption data accuracy, especially during experiments with volatile solvents, some samples were quenched in liquid nitrogen before recording their weight. No detectable difference was observed relative to the previous protocol. A third protocol was also used. After reaching equilibrium in the appropriate solvent, selected membranes were wiped and

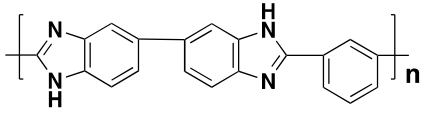
sealed in a weighing glass bottle before measuring the weight. The actual membrane weight was obtained by subtracting the weight of the bottle from the balance reading. Also in this case, no significant differences were observed relative to the first protocol.

After recording the weight, each membrane was returned in the appropriate solution. This process was repeated in a timeframe of days to weeks, depending on the solvent. Sorption experiments with water and lower alcohols reached equilibrium in 24 h. Sorption experiments with hydrocarbons (pentane, hexane, decane, toluene), 1-propanol, 2-propanol and PEG400 reached equilibrium in 10-12 weeks. These experiments were considered complete when the sample weight did not change for 7 days. Finally, the membrane was dried in a vacuum oven at 140°C for 24 hours until reaching a constant weight. Sorption was determined as follows:

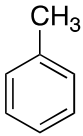
$$C = \frac{M_{\infty} - M_{dry}}{M_{dry}} \quad (\text{Eq. 32})$$

where  $M_{\infty}$  is the final equilibrium mass, and  $M_{dry}$  is the dry polymer mass. To measure the sorption of solvents exhibiting extremely low vapor pressure (e.g., PEG400), the dry weight was measured before soaking in the solvent. Indeed, the drying treatment would be insufficient to remove the penetrant sorbed into the polymer. For other liquids, the dry weight measured after treatment under vacuum was compared with the value measured before the sorption test. The good agreement between the two values indicates complete penetrant desorption after treatment under vacuum.

**Table 2.** Structure and chemical-physical properties of polymer [61, 52] and penetrants [53-57] considered with Celazole® (PTMSP was only tested with ethanol).

Celazole®		density (g/cm <sup>3</sup> )	solubility parameter (MPa <sup>0.5</sup> )	FFV
		1.27	32.4	0.120
		molar volume (cm <sup>3</sup> /mol)	molecular weight (g/mol)	solubility parameter (MPa <sup>0.5</sup> )



water	$\text{H}_2\text{O}$	18.0	18.0	47.8
methanol	$\text{H}_3\text{C}-\text{OH}$	40.7	32.0	29.7
ethanol	$\text{H}_3\text{C}-\text{CH}_2-\text{OH}$	58.5	46.1	26.0
1-propanol	$\text{H}_3\text{C}-\text{CH}_2-\text{CH}_2-\text{OH}$	75.2	60.1	24.9
2-propanol	$\text{H}_3\text{C}-\text{CH}(\text{OH})-\text{CH}_3$	76.8	60.1	23.8
1-butanol	$\text{H}_3\text{C}-\text{CH}_2-\text{CH}_2-\text{CH}_2-\text{OH}$	91.5	74.1	23.3
acetone	$\text{H}_3\text{C}-\text{C}(=\text{O})-\text{CH}_3$	74.1	58.1	20.3
toluene		106.9	92.1	18.3
n-pentane	$\text{H}_3\text{C}-\text{CH}_2-\text{CH}_2-\text{CH}_2-\text{CH}_3$	116.2	72.2	14.3
n-hexane	$\text{H}_3\text{C}-\text{CH}_2-\text{CH}_2-\text{CH}_2-\text{CH}_2-\text{CH}_3$	131.6	86.2	14.9
n-decane	$\text{H}_3\text{C}-\text{CH}_2-\text{CH}_2-\text{CH}_2-\text{CH}_2-\text{CH}_2-\text{CH}_2-\text{CH}_2-\text{CH}_2-\text{CH}_2-\text{CH}_3$	196.0	142.3	13.5
PEG400	$\text{H}-(\text{O}-\text{CH}_2-\text{CH}_2)_n-\text{OH}$	356.4	400.0	23.1

PTMSP in ethanol sorption tests under pressure were also conducted in the pressure range 0 to 10 atm. The custom built sorption cell, consisting of a double 1 in. VCR male and two female plugs, was filled with ethanol, and 3-4 PTMSP samples, pre-equilibrated in ethanol at atmospheric pressure, were soaked. The cell was tightly sealed and pressurized with nitrogen (cf. Fig. 11). After 24 hours, the system was quickly de-pressurized and the mass of the samples was recorded. Following this step, the sample was placed back into the cell and the experiment was repeated at a different pressure. Finally, the samples were dried for several hours, the dry weight was recorded and the sorption was calculated as described above.

*3.3 Mixed liquid sorption measurement.* Solubility of methanol/PEG400 mixtures (30, 50 and 70% wt. PEG400) in Celazole<sup>®</sup> was measured gravimetrically. One large membrane sample was soaked in each solution until reaching equilibrium conditions ( $V_{\text{solution}}/V_{\text{membrane}} \approx 200$ ). To prevent polarization phenomena, solutions were stirred during the experiments. The equilibrium weight was measured using an analytical balance. During the experiment, the temperature in the lab was about 23.5°C. After reaching equilibrium, each sample was placed in a vacuum oven and exposed to 70°C and moderate vacuum (-15 mmHg). Operation under controlled atmosphere helps to prevent absorption of atmospheric humidity by Celazole<sup>®</sup>, which is known to be a hydrophilic polymer. Due to the low vapor pressure of PEG400, only methanol evaporates during this process. This assumption was verified experimentally by exposing two small jars containing a known amount of pure PEG400 or methanol to 70°C and -15 mmHg. After several hours of exposure, the mass of PEG400 didn't change, while methanol completely evaporated. Moreover, a membrane previously equilibrated in pure methanol was exposed to 70°C and -15 mmHg. After 24h, the membrane was methanol-free. Methanol evaporation was considered complete when the sample reached a constant weight. The methanol and PEG400 uptake in mixed conditions was calculated as follows:

$$M_{CH_3OH}^{eq} = M_{\infty} - M' \quad (\text{Eq. 33})$$

$$M_{PEG}^{eq} = M' - M_{dry} \quad (\text{Eq. 34})$$

where  $M_{dry}$  is the dry polymer mass,  $M_{\infty}$  is the mass of the polymer after reaching equilibrium in the methanol/PEG400 mixture, and  $M'$  is the mass after the vacuum oven treatment (i.e., after methanol evaporation).

*3.4 Polymer dilation.* To investigate the polymer dimensional stability, sorption-induced dilation was measured. Membrane strips, whose dimensions were 3×7 cm, were soaked in organic liquids

and water and allowed to reach sorption equilibrium. Following this step, the membrane dimensions were measured using a Canon CanoScan Lide 220 scanner. The images were analyzed using the software ImageJ. The dimensions were measured again after drying the membranes in a vacuum oven. The percentage dilation was determined as follows:

$$\frac{\Delta\ell}{\ell_0} = \frac{\ell_\infty - \ell_0}{\ell_0} \quad (\text{Eq. 35})$$

where  $\ell_\infty$  is the polymer dimension after reaching equilibrium in any organic solvent and  $\ell_0$  is the dimension of dry polymer. To verify that dilation is isotropic,  $\frac{\Delta\ell}{\ell_0}$  was calculated in both length and width directions (cf. Fig. S2, Supporting Information).

### 3.5 Liquid solvent Permeability measurement

A large PTMSP sample was soaked in ethanol until reaching sorption equilibrium. Next, a circular sample (area = 14.6 cm<sup>2</sup>) was cut from the original membrane and returned in ethanol for other 24 hours. A dead-end filtration cell (Sterlitech Corporation, Kent WA) was used to measure liquid ethanol permeability as a function of pressure (up to 35 atm) at ambient temperature. Compressed nitrogen was used to generate a pressure gradient across the membrane. The permeate was collected in a graduated cylinder sealed with a dense stopper, to prevent ethanol evaporation. Ethanol flow rate was determined by tracking the level in the graduated cylinder at regular time intervals over the course of 3-4 hours.

*3.5 Vapor sorption and diffusion measurements.* Methanol vapor sorption in Celazole<sup>®</sup> was measured at 25, 35, and 45 degrees C using a constant volume, variable pressure (pressure decay) system. Details are provided in the Supporting Information section.

*3.6 Mechanical properties measurement.* Details about mechanical properties measurements are provided in the Supporting Information section.

### 3.7 *In situ* FTIR Spectroscopy measurements

FTIR spectroscopy experiments were carried out by colleagues at the department of chemical, materials, and manufacturing engineering at the University of Naples as well as the institute for polymers, composites, and biomaterials in Naples. The apparatus combines a FTIR Spectrum 100 interferometer from *Perkin Elmer (Norwalk, CT)* with a vacuum tight cell. The cell is connected to a flask whose volume is about 10 L, which ensures a stable vapor activity during the sorption experiment [52, 68]. A schematic diagram of the system is shown in Fig. S9, Supporting Information. The instrument is equipped with a Germanium/KBr beam splitter and a wide band DTGS detector. Sorption measurements are performed in transmission mode by increasing stepwise the vapor activity in the test cell. Two ZnSe windows (thickness = 4 mm) enable the passage of the IR beam. The collection parameters were set as follows: frequency resolution  $4\text{ cm}^{-1}$ ; optical path difference velocity =  $0.2\text{ cm s}^{-1}$ ; spectral range  $4000 - 600\text{ cm}^{-1}$ . Vacuum is monitored with a Pirani vacuumeter. A *Haake F6* bath circulates temperature-controlled water through the cell jacket. A dedicated LabVIEW program records the pressure data measured by a *MKS Baratron 121A* transducer (100 Torr F.S. range, 0.1% F.S. resolution, accuracy 0.5% of the reading) and acquired by a *MKS PR4000S* single channel controller. Stepwise sorption tests were performed at  $25^{\circ}\text{C}$  and in the vapor activity range 0-0.7 (testing protocol represented in Fig. S10, Supporting Information).

Two integral sorption tests were run in the activity range 0-0.05 and 0-0.1. During an integral sorption test the initial activity is zero, while during a differential test the initial activity is equal to the final equilibrium value in the previous step.

FTIR experiments were run in the same conditions as the barometric sorption measurement at  $25^{\circ}\text{C}$ . However, while a high-temperature drying was not possible in the barometric sorption

system, prior to running FTIR experiments the sample was fully dried at 150°C under high vacuum ( $10^{-3}$  Torr) for 30 min. As suggested in the literature, there exists a fraction of residual water tenaciously bound to the polymer substrate that can be eliminated only upon a thermal treatment at high temperatures [68].

## Chapter 4: Results and Discussion

### 4.1 Formulation of the solution diffusion theory: analysis of flux decline

*4.1.1 Liquid Ethanol Sorption in PTMSP.* PTMSP was the material chosen for permeability studies, due to the long experimental timeframe of permeability studies with Celazole<sup>®</sup> PBI membranes (sometimes weeks for permeation to even start) and to allow for direct comparison to the conclusions reported by Volkov et al., who reported that liquid ethanol diffusion coefficient in free-standing PTMSP membranes, determined from experimental flux data, exceeds ethanol self-diffusion coefficient [18]. They correctly noted that this result is physically unrealistic, and inferred that solvent transport in PTMSP membrane occurs by pore flow [18]. However, a more cautious analysis of experimental data dramatically alters this conclusion and shows that invoking the pore flow mechanism is unnecessary. For this reason, ethanol sorption and transport data in PTMSP are used to validate the framework developed in this study.

Ethanol flux through a free standing, 150  $\mu\text{m}$  thick PTMSP film is shown in Fig. 7A as a function of the pressure difference across the membrane,  $\Delta p$ . The experimental flux is a linear function of  $\Delta p$  up to 15 atm, and a negative departure from linearity is observed at higher  $\Delta p$ . This result provides evidence that flux decline takes place not only in supported membranes, but also in self-standing (i.e., backing-free) membranes, which implies that non-linear effects cannot be attributed to the compaction of the porous support.

Prior to interpret ethanol transport data in PTMSP using the thermodynamic-diffusion framework presented in section 2, the NELF model ability to describe ethanol sorption in PTMSP must be verified. Ethanol sorption isotherm in PTMSP in the activity range 0-1 and ambient temperature is shown in Fig. 7B. Vapor sorption data (activity  $< 1$ ) were from a previous study [50], while

This chapter is re-adapted from:  
Bye, Galizia, Fundamental origin of flux-nonlinearity in organic solvent nanofiltration: Formulation of a thermodynamic/diffusion framework, JMS, volume 603, 2020, with permission of Elsevier

liquid sorption (activity = 1) was measured in our laboratory as detailed in the Supporting Information.

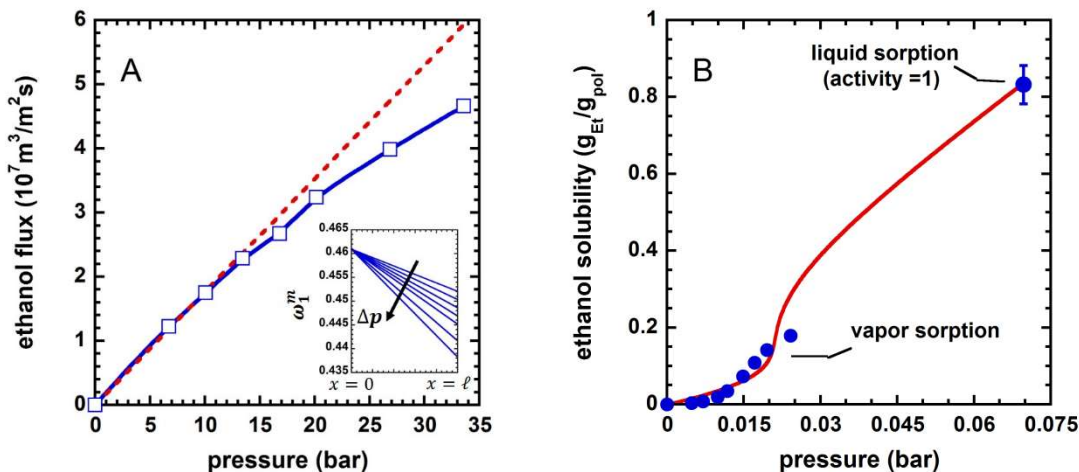


**Figure 7.** A) Ethanol flux at 25°C through a free standing, 150  $\mu\text{m}$  thick PTMSP film. Open squares are experimental data, and continuous blue line is a guide for the eye. Dashed red line is a linearization of the first portion of the flux vs.  $\Delta p$  curve. B) Ethanol sorption at ambient temperature in PTMSP in the activity range 0-1. Filled circles are experimental data, and continuous red line is the NELF best fit. Vapor sorption data are from ref. [50].

The lattice fluid parameters (i.e.,  $T^*$ ,  $p^*$  and  $\rho^*$ ) for PTMSP and ethanol were taken from the literature, and they are listed in Table 3.

**Table 3.** Lattice fluid parameters of PTMSP and ethanol.

	$T^*$ (K)	$p^*$ (MPa)	$\rho^*$ ( $\text{g}/\text{cm}^3$ )	source
PTMSP	515	550	1.250	[45]
ethanol	470	880	0.915	[69]

To calculate the sorption isotherm in the activity range 0-1 with the NELF model, the binary parameter  $k_{ij}$  (i.e., 0.07) was optimized by fitting the sorption data at low activity. This procedure relies on  $k_{ij}$  to be independent of temperature, pressure and composition [57, 59, 70]. The swelling coefficient,  $k_{sw}$ , was estimated combining Eqs. 30 and 31 with experimental dilation data,  $\frac{\Delta V}{V_0}$  :

$$k_{sw} = \frac{1}{p_0} \left( 1 - \frac{1}{1 + \frac{\Delta V}{V_0}} \right) \quad (\text{Eq. 36})$$

where  $p_0$  is the ethanol vapor pressure at the experimental temperature, and the resulting  $k_{sw}$  is 43.2 bar<sup>-1</sup>. However, doing so provides a pronounced underestimation of liquid solubility at activity 1 (cf. Fig. S8, Supporting Information). The reason of this departure relies in the NELF model inability to describe ethanol clustering at high activity [71, 72]. To get a good quantitative estimate of liquid solubility, it is necessary to use a swelling coefficient much larger than 43.2 bar<sup>-1</sup>. The actual value of the swelling coefficient, 8.69 bar<sup>-1</sup>, was retrieved by fitting the experimental liquid sorption datum to the NELF model using the  $k_{ij}$  value estimated as described above, i.e., 0.07. This procedure has been successfully used by Sarti to calculate ethanol solubility in glassy polycarbonate in the activity range 0-1 [73]. The  $k_{sw}$  retrieved in this way is an effective swelling coefficient, as it lumps the effects of polymer swelling and penetrant clustering. Doing so, provides a very good representation of ethanol sorption isotherms in PTMSP in the activity range 0-1 (cf., Fig. 7B). Interestingly, the model provides the proof of concept that PTMSP remains glassy upon exposure to ethanol in the activity range 0-1. Indeed, the Sanchez-Lacombe equation of state underestimates ethanol sorption in PTMSP from both vapor and liquid phase by almost two orders



of magnitude, suggesting that ethanol sorption occurs essentially in the excess free volume, which is not accounted for by the Sanchez-Lacombe equation of state.

Once the NELF model ability to describe ethanol sorption in PTMSP has been verified, ethanol concentration at the upstream and downstream membrane faces during a filtration experiment can be calculated. Based on Eq. 28, liquid ethanol solubility in the upstream membrane side (i.e.,  $\omega_{i,0}^m$ ) is expected to not change with increasing upstream pressure (i.e.,  $p_0 - p_\ell$ ). To support this conclusion, membrane samples were sealed into a stainless steel cell filled with liquid ethanol, and an isotropic pressure was imposed on the whole system using nitrogen, as detailed in section 3.2. In this experiment, both the sample and the surrounding liquid are under pressure, which mimics the upstream side of an OSN membrane during a filtration experiment. Liquid ethanol sorption in PTMSP (i.e.,  $\omega_{i,0}^m$ ) was measured up to 11 atm using the blot-and-weight method. To provide a very accurate estimate of  $\omega_{i,0}^m$ , nitrogen sorption in the polymer [74] was subtracted from the overall sorption data.  $\omega_{i,0}^m$  values are reported in Fig. 8 as a function of the applied pressure. As predicted by Eq. 28,  $\omega_{i,0}^m$  does not change with increasing ( $p_0 - p_\ell$ ).

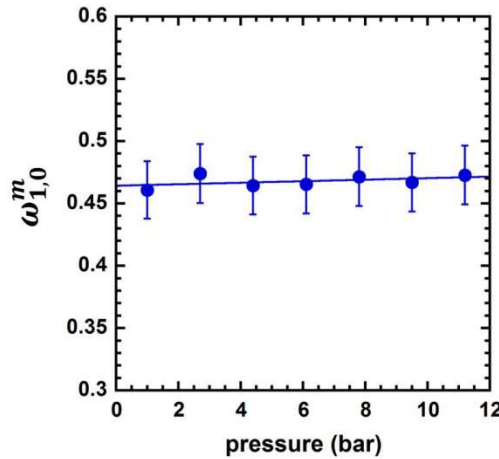


**Figure 8.** Liquid ethanol mass fraction in PTMSP (i.e.,  $\omega_{i,0}^m$ ) at different pressures. As predicted by the thermodynamic framework,  $\omega_{i,0}^m$  does not change with  $\Delta p$ . The uncertainty was estimated

from the standard deviation of three separate experiments [75]. The continuous line is a guide for the eye.

In contrast, based on Eq. 29, ethanol mass fraction in the downstream membrane face,  $\omega_{i,\ell}^m$ , is expected to decrease with increasing the pressure difference across the membrane (i.e.,  $p_0 - p_\ell$ ) (cf. Fig. 9A). To calculate  $\omega_{i,\ell}^m$ , we start from the experimental flux vs.  $(p_0 - p_\ell)$  data, where  $p_\ell$  is constant and equal to 1 atm. Eq. 29 was used to calculate the ethanol activity in the downstream membrane face,  $a_{i,\ell}^m$ , corresponding to any  $p_0$  value. Since in this study we consider pure ethanol transport data, in Eq. 29  $a_{i,\ell}^s$  was assumed equal to 1. The ethanol mass fraction in the downstream membrane side corresponding to any  $a_{i,\ell}^m$  was predicted with the NELF model, using the  $k_{ij}$  value estimated from vapor sorption data, and the  $k_{sw}$  value optimized to the experimental liquid sorption datum, as detailed above. In doing so, we implicitly assume that the swelling is uniform throughout the membrane thickness (i.e., that the upstream and downstream membrane faces experience the same swelling). In this specific case this assumption is reasonable, since  $a_{i,\ell}^m$  does not depart significantly from  $a_{i,0}^m$  (i.e., 1) in the entire  $\Delta p$  range (0-35 bar) investigated. For example,  $a_{i,\ell}^m$  is 0.984 when  $\Delta p$  is 7 bar, and 0.930 when  $\Delta p$  is 35 bar, with a maximum deviation of 7% from the upstream value. Therefore, it is reasonable to calculate  $\omega_{i,\ell}^m$  using the  $k_{sw}$  value estimated by fitting the liquid sorption datum,  $\omega_{i,0}^m$ , at activity 1.

As shown in Fig. 9A-B, ethanol content in the membrane at  $x = \ell$  decreases with increasing  $\Delta p$ .

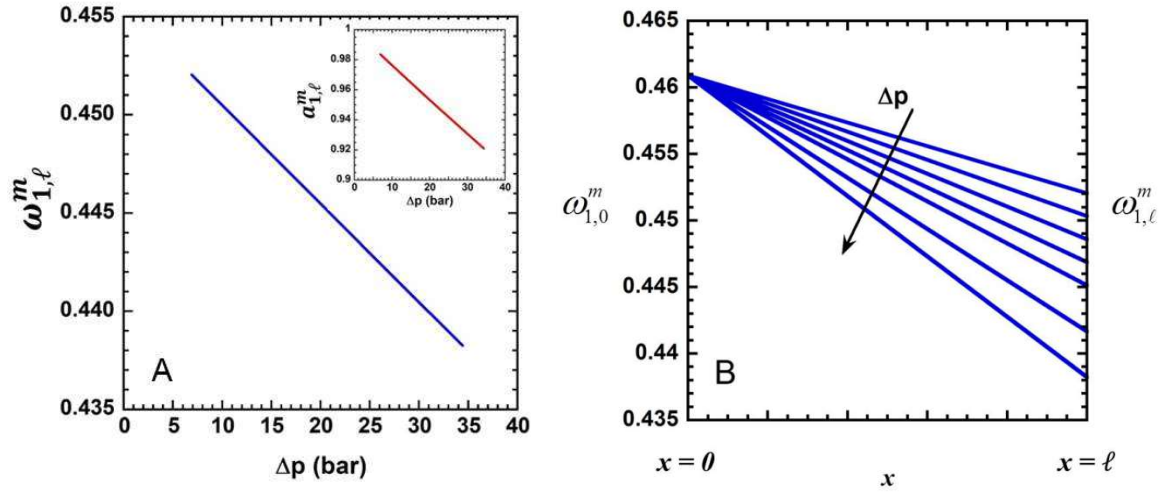


**Figure 9.** A) Ethanol mass fraction in the downstream face of a PTMSP membrane during a dead-end filtration test, calculated combining the Paul's model and the NELF model. B) Effect of  $\Delta p$  on the membrane ethanol content, calculated combining the Paul's model and the NELF model. Obviously, the model can calculate  $\omega_1^m$  at  $x = 0$  and  $x = \ell$ , therefore the line at  $0 < x < \ell$  is drawn to guide the eye.

Fig. 9A indicates that  $\omega_{i,\ell}^m$  becomes zero at high pressures. In the limit case where  $\omega_{i,\ell}^m$  is nul, the driving force for solvent transport, i.e.  $\omega_{i,0}^m - \omega_{i,\ell}^m$ , is maximum, therefore, based on the Fick's law, a ceiling flux must exist, which explains why flux versus  $\Delta p$  must exhibit a downward curvature. The pressure at which  $\omega_{i,\ell}^m$  becomes zero,  $p^{ceiling}$ , can be approximately predicted by extrapolating the curve shown in Fig. 8 at  $\omega_{i,\ell}^m = 0$ . In the specific case of the system ethanol/PTMSP,  $p^{ceiling}$  is about 908 bar. However, in doing so, the assumption of uniform swelling throughout the membrane thickness is quite crude, since the activity gradient across the membrane is no longer negligible, therefore the ceiling pressure estimated above is affected by a high degree of uncertainty.

An important implication of Eq. 29 is that, for any given  $(p_0 - p_\ell)$  value, the extent of  $\omega_{i,\ell}^m$  depends on the solvent molar volume (i.e., on the solvent molecular size) [1, 22]. Specifically, solvents with larger molar volume are squeezed out to a greater extent from the downstream membrane face when the upstream pressure is increased [1, 22, 39].

*4.1.2 Liquid ethanol diffusion coefficient in PTMSP.* As discussed above, flux decline occurs as long as the driving force for mass transfer across the membrane approaches its maximum value. However, based on the Fick's law, flux decline might also be caused by a decrease of the diffusion coefficient with pressure. To shed fundamental light on this aspect, liquid ethanol diffusion coefficients in PTMSP were determined as a function of the concentration gradient across the membrane,  $\omega_{1,0}^m - \omega_{1,\ell}^m$ . Three methods were used to calculate diffusion coefficients, which, as detailed below, provided substantially different results.

*Method 1.* The Fick's law is written under the hypothesis that the flux with respect to the fixed frame is equal to that with respect to the moving frame (i.e.,  $j_i = n_i$ ), as in the case of gas separation membranes. Diffusion coefficients were calculated by integrating Eq. 15, and neglecting the effects of the frame of reference and thermodynamic non-ideality:

$$\bar{D}_i = \frac{j_i \ell}{\rho (\omega_{i,0}^m - \omega_{i,\ell}^m)} \quad (\text{Eq. 37})$$

The density of the polymer-penetrant mixture,  $\rho$ , can be calculated from swelling and sorption

data (i.e.,  $\rho = \frac{\rho_{pol,0} \left( 1 + \frac{M_{1w} C}{22414 \rho_{pol,0}} \right)}{\left( 1 + \frac{\Delta V}{V_0} \right)}$ , where  $\rho_{pol,0}$  is the density of unpenetrated polymer, 0.75 g/cm<sup>3</sup>,

$C = 304 \text{ cm}^3(\text{STP})/\text{cm}^3 \text{ polymer}$  is the ethanol concentrations in PTMSP at activity 1,  $M_{1w}$  is ethanol molecular weight, and  $\frac{\Delta V}{V_0}$  is the polymer volume dilation, which was calculated from linear

dilation as  $\left[ \left( \frac{\ell}{\ell_0} \right)^3 - 1 \right]$  [61]. Although this method is frequently used to calculate small molecule diffusion coefficients in gas separation polymer membranes, it does not work for OSN membranes. Indeed, as shown in Fig. 10, the diffusion coefficient calculated according to Eq. 37 exceeds the ethanol self-diffusion coefficient, which is physically unrealistic. Penetrant diffusion coefficient in polymers cannot exceed self-diffusion coefficient for two reasons: *i)* the presence of polymer chains, which make the diffusion pathway more tortuous relative to self-diffusion [48], and *ii)* molecular interactions, which contribute to reduce penetrant mobility in the polymer [38]. Volkov and co-workers used Eq. 37 to calculate liquid ethanol diffusivity in PTMSP from experimental flux data, and correctly noted that the results were physically unrealistic. Therefore, they concluded that solvent transport in OSN membranes cannot be simply described by the solution-diffusion mechanism [18]. Unfortunately, this conclusion results from the incorrect use of the Fick's law, since Eq. 37 cannot properly describe organic solvents transport in polymer membranes.

Method 2. The Fick's law is written by accounting for the effect of the frame of reference (i.e.,  $j_i \neq n_i$ ), while the effects of thermodynamic non-idealities are neglected. Therefore, diffusion coefficients were calculated using Eq. 17. As shown in Fig. 10, diffusion coefficients are lower than ethanol self-diffusion coefficient, and they asymptotically approach it at high pressure.

Method 3. Diffusion coefficients calculated using the method 2 were corrected for the effects of thermodynamic non-idealities to get  $\bar{D}_i^*$ . The value of the thermodynamic factor,  $\beta$  was reported by Doghieri [50] and is 1.5 at activity close to one. As shown in Fig. 10,  $\bar{D}_i^*$  is always lower than ethanol self-diffusion coefficient. Obviously, the latter method is the only one able to provide a realistic estimate of diffusion coefficients.

Noteworthy, liquid ethanol diffusion coefficients in PTMSP increase with increasing  $\omega_{1,0}^m - \omega_{1,\ell}^m$  (i.e.,  $\Delta p$ ) before reaching a constant value, which indicates that flux non-linearity is only caused by the concentration profile in the membrane, as discussed above. This result further indicates that invoking membrane compaction to explain flux decline with pressure is not appropriate. Indeed, membrane compaction should cause a pronounced decrease of diffusion coefficient with increasing  $\Delta p$ , which is not consistent with the results shown in Fig. 10. The increase of  $\bar{D}_i^*$  with  $\Delta p$  before reaching a constant value could be explained by considering that the net amount of ethanol sorbed in the membrane decreases with increasing  $\Delta p$  (cf. Fig. 9B). Since ethanol is a polar liquid, the extent of clustering is expected to decrease with decreasing the amount of ethanol sorbed in the polymer [45], i.e., with increasing  $\Delta p$ , which would be consistent with the results shown in Fig. 10. As it is well known, indeed, clustering produces a decrease of diffusion coefficient, due to the larger size of clusters relative to single molecules. An increase of diffusivity with pressure was previously observed by Paul when considering the transport of several organic liquids in swollen natural rubber [29].

The experimental/theoretical analysis presented above provides the proof of concept that the solution-diffusion model is sufficient to describe solvent transport in OSN membranes, therefore the need to resort to the pore-flow or more complicated mechanism is the result of the inappropriate mathematical formulation of the problem.

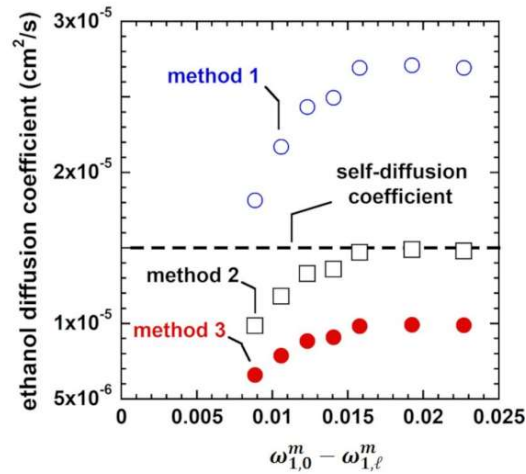


**Figure 10.** Liquid ethanol diffusion coefficient at ambient temperature in PTMSP as a function of the ethanol concentration gradient across the membrane.

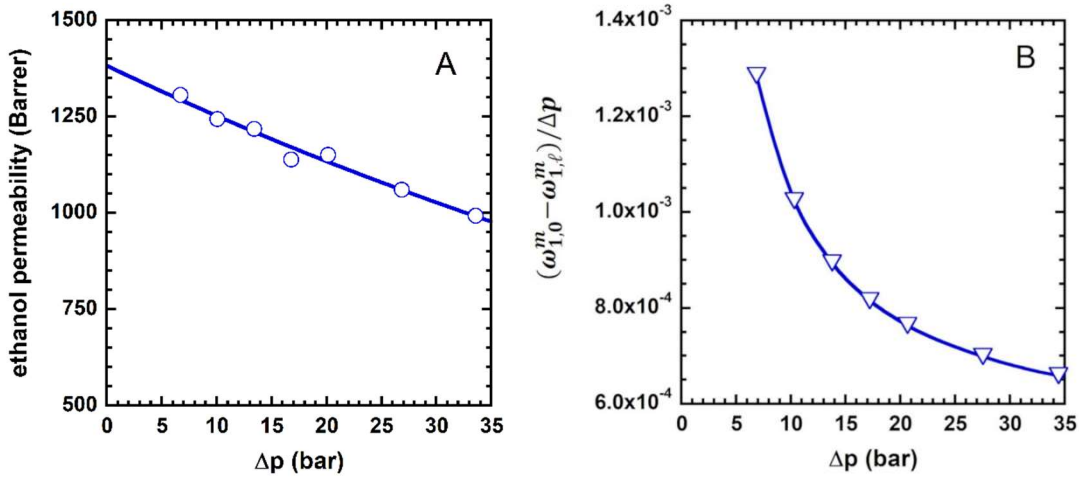
4.1.3 Liquid ethanol permeability in PTMSP. While gas separation and water purification membranes are characterized in terms of permeability and selectivity, OSN membranes are almost always characterized in terms of solvent flux and solute rejection [1]. The difference between the two nomenclatures is substantial: indeed, while permeability and selectivity are intrinsic properties of the membrane material, flux and rejection are not, since they depend on the membrane thickness. An unanswered fundamental question is: *how does solvent permeability through OSN membranes change with  $\Delta p$ ?* While this aspect has been deeply investigated for gas separation membranes and rationalized using the dual mode sorption-transport model [41, 76, 77], it is completely unexplored for OSN membranes.

Liquid ethanol permeability through a free standing PTMSP membrane, expressed in the standard units of Barrer ( $1 \text{ mol m}^{-1} \text{ s}^{-1} \text{ kPa}^{-1} = 2.99 \times 10^{12} \text{ Barrer}$  [78]), was calculated using Eq. 3 and is shown in Fig. 11 as a function of the pressure difference across the membrane. Interestingly, permeability decreases by about 30% in the pressure range 0-35 bar. This behavior can be

explained by analyzing the trend of permeability, sorption and diffusion coefficients as a function of  $\Delta p$ . Within the framework of the solution-diffusion model, the permeability coefficient can be expressed as follows:

$$\phi_i = \bar{D}_i \left( \frac{C_{1,0}^m - C_{1,\ell}^m}{\Delta p} \right) \quad (\text{Eq. 38})$$

where  $C_{i,0}^m$  and  $C_{i,\ell}^m$  are the penetrant concentration in the upstream and downstream membrane face, respectively, expressed in units of  $\text{cm}^3(\text{STP})/\text{cm}^3$  polymer.  $C_{i,0}^m$  and  $C_{i,\ell}^m$  can be calculated directly from the  $\omega_{i,0}^m$  and  $\omega_{i,\ell}^m$  values estimated as detailed above. Interestingly,  $\frac{\omega_{i,0}^m - \omega_{i,\ell}^m}{\Delta p}$  (i.e.,  $\frac{C_{i,0}^m - C_{i,\ell}^m}{\Delta p}$ ) decreases with increasing  $\Delta p$ , and  $\bar{D}_i$  increases with increasing  $\Delta p$ , which indicates that the decrease in ethanol permeability with  $\Delta p$  mirrors the decrease in sorption coefficient with  $\Delta p$ . This result implies that, at least for the system ethanol-PTMSP, the permeability coefficient is controlled by the concentration gradient across the membrane.





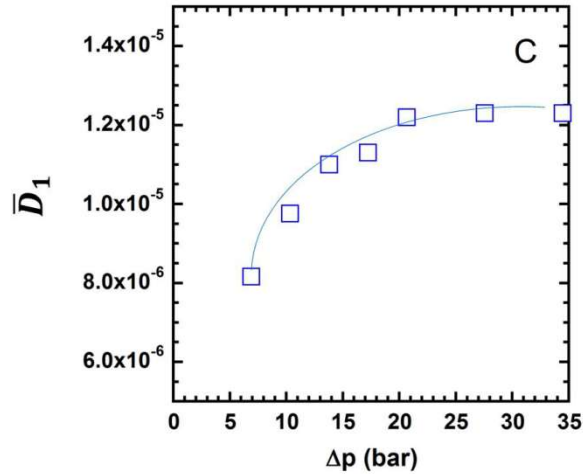


**Figure 11.** A) Liquid ethanol permeability in PTMSP as a function of the pressure difference across the membrane. B)  $\frac{\omega_{1,0}^m - \omega_{1,\ell}^m}{\Delta p}$  as a function of  $\Delta p$ ; C) concentration-averaged, liquid ethanol diffusion coefficient in PTMSP (i.e.,  $\bar{D}_1$ ) corrected for the frame of reference and non-ideal effects as a function of  $\Delta p$ .

Absent fundamental correlations between solvent permeation, sorption and diffusion, the permeability decrease with  $\Delta p$  shown in Fig. 12 could be explained by invoking membrane compaction. However, the *vis-à-vis* comparison of Figs. 11A-B-C indicates that the permeability decay with  $\Delta p$  is ascribable to the solvent concentration profile across the membrane, instead of membrane compaction.

To summarize, the flux non-linearity vs.  $\Delta p$  and permeability decay with  $\Delta p$  have a purely thermodynamic origin, that is, they are ascribable to the behavior of sorption coefficient, therefore invoking membrane compaction or complicated transport mechanisms to explain these phenomena is unnecessary.

## 4.2 Role of molecular interactions on Celazole<sup>®</sup> performance

4.2.1 *Pure liquid sorption.* Small molecule sorption in polymers is ruled by the interplay between energetic (i.e., enthalpic) and entropic factors, which are related to polymer-penetrant interactions (i.e., polymer-penetrant affinity) and penetrant molecular size, respectively [79].

Celazole<sup>®</sup> PBI was the material of choice for sorption focused studies instead of PTMSP due to its high chemical stability in a wide variety of solvents. It is only dissolvable in DMAc, which allows it to be tested in a wide range of organic solvents. Additionally, PBI has amine groups on its backbone which allow for analysis of specific polymer-penetrant interactions which are essential to understanding the enthalpic interactions between polymer and penetrant while PTMPS has no specific interaction sites on its backbone. In this study, we assume the penetrant molar volume as a measure of the penetrant size, and the difference between the polymer and penetrant Hildebrand solubility parameter as a measure of the polymer-penetrant affinity. Small molecule solubility is expected to decrease with increasing penetrant size (indeed, for entropic reasons, the probability of accommodating penetrant molecules in the polymer matrix decreases with increasing penetrant size), and to increase with decreasing difference between the polymer and penetrant Hildebrand solubility parameter [34, 79]. Care must be taken in selecting the appropriate unit to express solubility. Penetrant sorption in polymers can be expressed in mass, molar, or volume units. While mass-based solubility only accounts for the total amount of penetrant sorbed by the polymer, molar and volume-based solubility also account for penetrant size. As shown in Fig. 12A, the mass-based solubility of several liquids in Celazole<sup>®</sup> at 25°C

This chapter is re-adapted from:

Bye et al., Pure and mixed fluid sorption and transport in celazole<sup>®</sup> polybenzimidazole: Effect of plasticization, *JMS*, 235-247, volume 580, 2019, with permission of Elsevier

Loianno et al., Plasticization mechanism in polybenzimidazole membranes for organic solvent nanofiltration: Molecular insights from in situ FTIR spectroscopy, *Journal of Polymer Science*, 2547-2560, volume 58, issue 18, 2020 with permission of Wiley Online Library

exhibits a non-monotonous trend with penetrant molar volume. Specifically, it first increases in the order water < methanol < ethanol < 1-propanol, and then markedly decreases with increasing penetrant size.

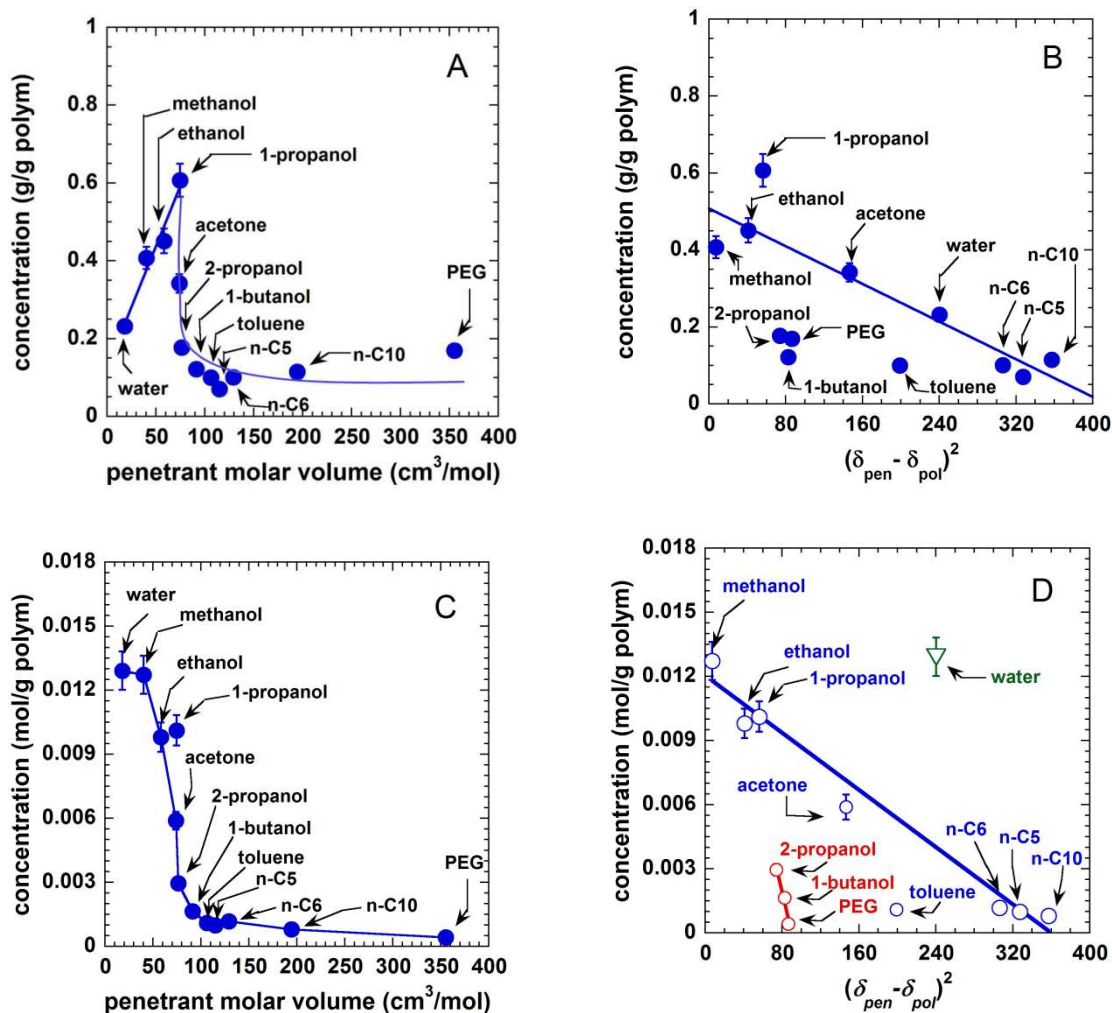


**Figure 12.** A) Liquid sorption in Celazole® (mass-based) at 25°C as a function of liquid molar volume. B) Liquid sorption in Celazole® (mass-based) at 25°C as a function of  $(\delta_{pen} - \delta_{pol})^2$ . C) Liquid sorption in Celazole® (molar-based) at 25°C as a function of liquid molar volume. D) Liquid sorption in Celazole® (molar-based) at 25°C as a function of  $(\delta_{pen} - \delta_{pol})^2$ . Continuous lines are a guide for the eye.

Polar –OH groups of water and alcohols, which act as proton donors, are expected to interact favorably with the –NH groups on the polymer backbone, which are proton acceptors, likely via hydrogen bonding. Interestingly, 1-propanol exhibits the largest mass uptake. The solubility of primary lower alcohols (methanol, ethanol, 1-propanol) increases linearly with increasing length of the alkyl chain, which may reflect the polymer swelling (i.e., dilation) induced by the sorption of bulky polar liquids. As discussed in section 4.2.2, alcohols induce severe polymer swelling, which: *i*) increases with increasing alcohol molecular size (i.e., 1-propanol > ethanol > methanol), and *ii*) exhibits the same trend of mass-based solubility as a function of penetrant molar volume (cf. Fig. 13B). Therefore, polymer swelling causes the non-monotonous trend observed in Fig. 12A. The large polymer swelling caused by lower alcohols is due, in turn, to their favorable interaction with the polymer backbone. Such a picture indicates that the unexpected increasing trend exhibited by the solubility of polar penetrants with molar volume has an enthalpic origin. Interestingly, 2-propanol is sorbed to a much lower extent relative to 1-propanol, despite the two liquids exhibit similar properties and a fairly similar molar volume (cf. Table 2). This behavior is likely ascribable to the fact that the -OH group in 2-propanol is much more sterically shielded than in 1-propanol, which limits the ability of 2-propanol to form hydrogen bonds with the –NH groups on the polymer backbone. Therefore, enthalpic effects rule the sorption of these two isomers. Interestingly, the opposite behavior was observed in PDMS. As reported by Cocchi et al. [31], the solubility of butanol isomers in PDMS increases in the order: tert-butanol > iso-butanol > 1-butanol. Since in tertiary alcohols the –OH polar group is more efficiently shielded by the alkyl tail, their interaction with the hydrophobic PDMS backbone is much more favorable than that of secondary or primary alcohols. Due to its polar structure, Celazole<sup>®</sup> exhibits a completely reversed

behavior relative to PDMS. Therefore, the solubility of more polar compounds, such as primary alcohols, in Celazole<sup>®</sup> is energetically favored over that of less polar compounds, such as secondary alcohols. The decrease of solubility observed for bulkier penetrants (1-butanol, hydrocarbons, PEG400) as a function of molar volume is ascribable to entropic effects. In fact, for entropic reasons, the probability of accommodating penetrant molecules in the polymer matrix decreases with increasing their molecular size. This conclusion is further supported by the fact that, as discussed in section 4.2.2, sorption of bulky non-polar penetrants does not induce significant matrix swelling, due to their unfavorable interaction with the polymer. In Fig. 12B, the mass-based solubility is reported as a function of  $(\delta_{pen} - \delta_{pol})^2$ , where  $\delta_{pen}$  and  $\delta_{pol}$  are the penetrant and polymer Hildebrand solubility parameters, respectively. This representation of sorption data accounts for enthalpic effects, as polymer-penetrant interactions are expected to be less thermodynamically favorable with increasing difference between solubility parameters. When the polymer-penetrant interaction pattern is described in terms of dispersion forces, penetrant solubility in polymers decreases fairly linearly with increasing  $(\delta_{pen} - \delta_{pol})^2$  [34]. Some deviations from this rule can be observed in Fig. 12B, which indicate that, to properly quantify the role of the enthalpic effects, sorption data need to be corrected for the effects of penetrant size. Therefore, comparison of sorption data as a function of  $(\delta_{pen} - \delta_{pol})^2$  should be done by using volume or molar units. Since using volume or molar units leads to the same conclusions, for the sake of brevity, molar units will be used in the following discussion. The molar-based solubility decreases monotonically with increasing penetrant size and all data lie on a master curve (cf. Fig. 12C). In Fig. 12D, the molar solubility is reported as a function of  $(\delta_{pen} - \delta_{pol})^2$ . Most of the sorption data follow a linear decreasing trend with  $(\delta_{pen} - \delta_{pol})^2$  ( $R^2 = 0.98$ ), and, in general,

molar solubility exhibits a more regular linear trend with  $(\delta_{pen} - \delta_{pol})^2$  relative to the mass solubility. The molecular origin of the negative deviation of 2-propanol, 1-butanol, toluene and PEG400 sorption data from the trend in Fig. 12D is currently unknown and could be tentatively ascribed to unfavorable polymer-penetrant interactions. Interestingly, water sorption follows a linear trend with  $(\delta_{pen} - \delta_{pol})^2$  when it is expressed in mass basis, but a large positive deviation is observed when molar units are used. Therefore, sorption data corrected for penetrant size, which provide a more realistic representation of enthalpic effects, indicate that water-polymer interaction is much stronger than expected. This picture is in agreement with recent studies from Moon [52] and Musto [68].

The relative importance of enthalpic and entropic effects can be quantified using the lattice fluid theory [79], which permits de-convolution of the overall solubility into its elementary enthalpic and entropic contributions [79]. However, since the three polymer lattice fluid parameters are unknown, this theoretical analysis is out of reach at this time.

*4.2.2 Polymer Dilation.* To verify that Celazole<sup>®</sup> dilation in organic solvents and water is isotropic, elongation in the  $x$  (length) and  $y$  (width) directions was measured. As expected, these values match within the experimental uncertainty (cf. Fig. S2, Supporting Information). Dilation data reported in Figs. 13 are the average of the values measured in the  $x$  (width) and  $y$  (length) directions. Polymer dilation in organic liquids at 25°C increases linearly with increasing penetrant mass uptake ( $R^2 = 0.94$ , cf. Fig. 13A). Dilation, also referred to as swelling, is defined as the change in the polymer specific volume induced by penetrant sorption. More specifically, when dilation takes place, the volume of the polymer-penetrant mixture exhibits a positive departure from the additive rule [78-80]. Especially during the sorption of condensable vapors and liquids, sorption in the Henry's mode causes a separation of polymer chains, which acquire a less packed

structure to accommodate additional penetrant molecules [80-82]. To quantify the extent of sorption in the Henry's and Langmuir's modes, sorption experiments were run for a model solvent, methanol, over the entire activity range 0-1 (cf. section 4.2.4).

The less efficient chain packing caused by dilation produces two effects: *i*) it renders the polymer chains much more flexible, and *ii*) it increases the size of free volume elements [61, 82-85]. Based on this picture, data reported in Fig. 13A indicate that penetrant uptake increases with increasing amount of free volume. Therefore, the long-time liquid sorption in Celazole<sup>®</sup> is dominated by polymer swelling.

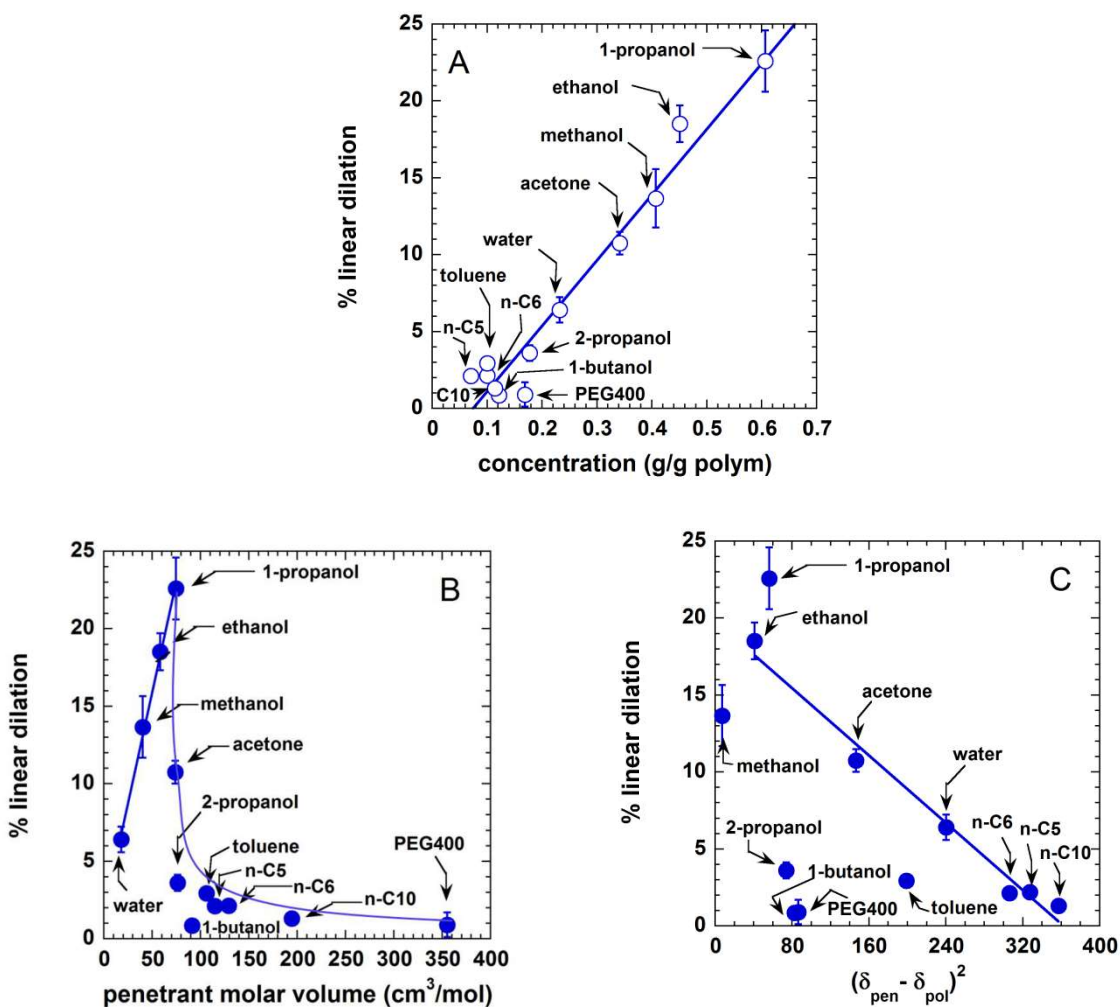


**Figure 13.** Celazole<sup>®</sup> linear dilation in organic liquids and water at 25°C as a function of: A) penetrant mass-based concentration, (B) penetrant molar volume and (C)  $(\delta_{pen} - \delta_{pol})^2$ .

Interestingly, dilation data (Figs. 13B-C) exhibit the same trend of mass-based solubility (Figs. 12A-B) as a function of liquid molar volume and  $(\delta_{pen} - \delta_{pol})^2$ , which confirms that liquid sorption in Celazole<sup>®</sup> is dominated by polymer swelling.

Dilation data indicate that polar liquids significantly swell Celazole<sup>®</sup>. Specifically, Celazole<sup>®</sup> linear dilation is 6.5% in water, 13.5% in methanol, 18.5% in ethanol and 22.5% in 1-propanol. A non-negligible dilation, about 10.8%, is also observed in acetone. In contrast, linear dilation upon exposure to low-polar (1-butanol, 2-propanol) or non-polar (hydrocarbons) liquids does not exceed 3.6%. To put these data in perspective, they were compared with the dilation induced by organic liquid sorption in other glassy polymers. PIM-1 linear dilation is over 20% in methanol, and exceeds 25% in toluene and xylenes [29]. Polyimide P84 exhibits a linear swelling of about 10% in alcohols, water, hydrocarbons and toluene [36]. Finally, Matrimid<sup>®</sup> swells by about 25% in alcohols [36]. This comparison indicates that Celazole<sup>®</sup> stability is very high in non-polar solvents, and it is comparable to that of conventional glassy polymers upon exposure to polar solvents. This physical picture is supported by the conclusions drawn by Liu et al. in their simulation study [86].

**4.2.3 Mixed liquid sorption.** Solubility of binary methanol-PEG400 mixtures in Celazole<sup>®</sup> is reported in units of g/g<sub>polymer</sub> in Fig. 14A, as a function of methanol mass fraction in the external solution. Mixtures containing 30, 50 and 70% wt. methanol were considered. Interestingly, the total mixture solubility exhibits a maximum when the methanol mass fraction in the liquid mixture is about 30%. In this condition, the partial solubility of PEG400 reaches a maximum. In contrast, methanol solubility is essentially constant with methanol concentration in the external solution.



These results suggest that PEG400 sorption is significantly enhanced by the presence of methanol, but methanol sorption is not affected by the presence of PEG400. A similar behavior was observed by Cocchi et al. during solute/solvent mixtures sorption in rubbery PDMS [87]. This behavior is likely ascribable to the polymer swelling induced by methanol sorption. Specifically, when the methanol mass fraction in the external solution is 30% wt., PEG400 sorption is enhanced 4 times (in terms of mass) relative to pure PEG400 sorption. The presence of a maximum in PEG400 sorption could be explained by invoking the polymer swelling induced by methanol, and by considering that, when the external methanol concentration is 30% wt., the most abundant component in the mixture is PEG400.

The data discussed above were used to calculate the real methanol/PEG400 solubility-selectivity,  $\alpha_S$ , which is defined as follows:

$$\alpha_S = \frac{S_{CH_3OH}}{S_{PEG}} \quad (\text{Eq. 39})$$

where  $S_{meth}$  and  $S_{PEG}$  are the sorption (i.e., partition) coefficients of methanol and PEG400 calculated from mixed liquid sorption experiments. For each component,  $S_i$  was calculated as follows:

$$S_i = \frac{C_i}{\omega_i} \quad (\text{Eq. 40})$$

where  $C_i$  is the concentration of species  $i$  in the polymer expressed in units of  $\text{cm}^3_{\text{pen}}(\text{STP})/\text{cm}^3_{\text{polym}}$ , and  $\omega_i$  is the mass fraction of species  $i$  in the liquid mixture. Obviously, the activity of species  $i$  in the external solution should appear in the denominator of Eq. 40 in place of mass fraction. However, since reliable liquid-liquid equilibrium data for the mixture methanol-PEG400 are not available in the literature, compositions were used in place of activities. As a matter of fact, the main purpose of this analysis is to highlight the effect of the second component on sorption

selectivity, rather than providing the absolute value of sorption-selectivity. Mixed sorption coefficients for methanol and PEG400, and methanol/PEG400 solubility selectivity are reported in Fig. 14B-C, respectively, as a function of methanol mass fraction in the external solution. Interestingly, the real solubility-selectivity is up to 3 times lower relative to that calculated in ideal conditions (i.e., as the ratio of pure components sorption coefficient). Loss of solubility-selectivity in real conditions reflects the solvent (i.e., methanol) ability to swell Celazole<sup>®</sup>. To figure out if polymer swelling is also accompanied by plasticization, a more fundamental investigation of methanol sorption from the liquid and vapor phases is needed. Such an investigation is presented in the following section.

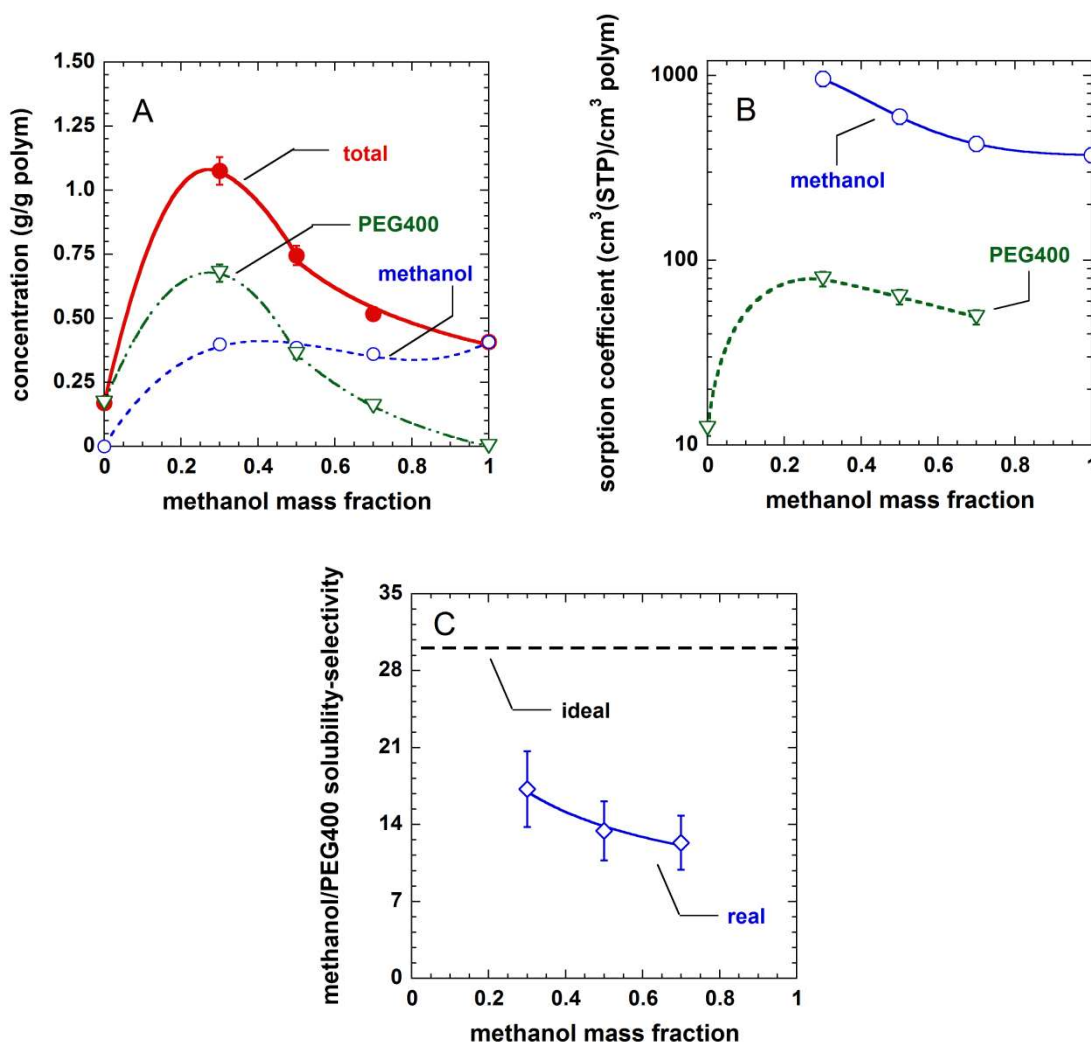


**Figure 14.** A) Total mixed methanol/PEG400 solubility and partial methanol and PEG400 solubility at room temperature, expressed in units of g/g dry polymer, as a function of methanol mass fraction in the external solution. B) Methanol and PEG400 sorption coefficient in mixture conditions, calculated from Eq. 40. C) Ideal and real methanol/PEG400 solubility-selectivity as a function of methanol mass fraction in the external solution.

4.2.4 Methanol vapor sorption and diffusion. Methanol was selected as a model penetrant for sorption and diffusion experiments in the activity range 0-1. In Fig. 15A, methanol sorption in Celazole<sup>®</sup> at 25°C is reported as a function of activity (i.e., relative pressure,  $\frac{p}{p^0}$ , where  $p^0$  is the methanol vapor pressure at 25°C). Liquid methanol solubility (i.e., at activity 1) is also reported for the sake of comparison. The experimental uncertainty was calculated using the error propagation method [75] and is lower than 5%. The uncertainty associated to liquid sorption was calculated from the standard deviation of three independent measurements and is about 3%. Due to intrinsic instrument limitations, the maximum activity reached during vapor sorption experiments is 0.7.

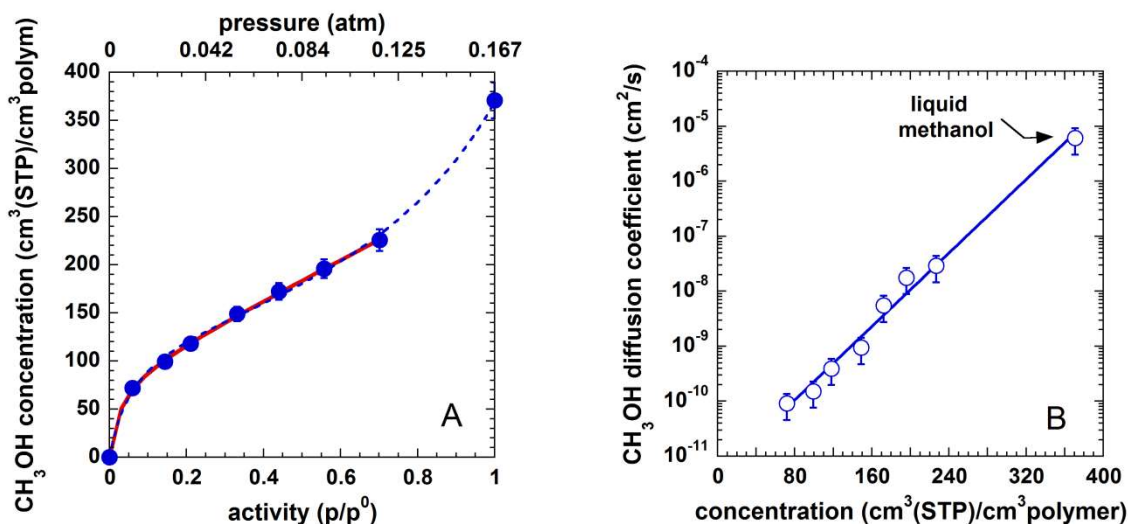


**Figure 15.** A) Methanol sorption in Celazole<sup>®</sup> at 25°C as a function of activity. The continuous red line represents the dual mode fitting, and the dashed blue line is a guide for the eye. B) Methanol diffusion coefficient in Celazole<sup>®</sup> at 25°C as a function of concentration. The blue line is an exponential interpolation.

The methanol sorption isotherm is concave to the activity axis in the activity range 0-0.7, according to the typical dual-mode behavior of glassy polymers. Methanol sorption isotherms in other glassy polymers, such as polyacetylenes [45] and amorphous Teflon AF<sup>®</sup> [88, 89], exhibit a strong upturn at activities of 0.2-0.3, which may indicate polymer plasticization or penetrant clustering [43, 45, 89]. The methanol sorption isotherm in Celazole<sup>®</sup> exhibits a well detectable upturn only at activities higher than 0.7. This behavior could be ascribed to the rigid structure of polybenzimidazoles, whose chain motion is limited by the presence of aromatic fused rings on the polymer backbone, as well as by inter-chain hydrogen bonds [90, 91].

The dual mode model provides an excellent fit of the experimental sorption isotherm in the activity range 0-0.7. The three model parameters are listed in Table 3. For the sake of comparison, the dual mode parameters for the system PIM-1/methanol at 25°C are also shown [29]. Interestingly, PIM-1 and Celazole<sup>®</sup> exhibit similar Henry's constants and Langmuir sorption capacities [29]. However, Celazole<sup>®</sup> has a much higher affinity parameter than PIM-1 (+185%), which reflects the polarity of the polybenzimidazole backbone and its ability to establish thermodynamically favorable interactions with polar methanol molecules. Interestingly, methanol sorption in Celazole<sup>®</sup> and PIM-1 at 25°C are comparable (cf. Fig. S3-A, Supporting Information). However,

while methanol sorption in PIM-1 is entropy-driven, due to the large amount of free volume ( $\approx 29\%$ ) exhibited by this polymer, methanol sorption in Celazole<sup>®</sup> is, at least at low activity, enthalpy-driven. Indeed, despite exhibiting a much smaller free volume ( $\approx 12\%$ ) and a densely packed structure, Celazole<sup>®</sup> offers a more thermodynamically favorable environment to methanol molecules. As discussed later in this study, methanol severely plasticizes Celazole<sup>®</sup>, therefore the apparent Celazole<sup>®</sup> free volume increases with increasing methanol activity.

The dual mode analysis indicates that full saturation of Celazole<sup>®</sup> Langmuir sites occurs when methanol activity is 0.2 (cf. Fig. S4, Supporting Information), therefore, when  $\frac{p}{p^0} > 0.2$ , sorption into the Henry's mode becomes predominant. However, the sorption isotherm does not exhibit any concavity change at activity lower than 0.7. This result might lead to the conclusion that methanol swells but does not plasticize Celazole<sup>®</sup>. If this picture was right, the upturn exhibited by the methanol sorption isotherm in Celazole<sup>®</sup> at activities larger than 0.7 should be ascribed to penetrant clustering. The analysis of diffusion coefficients sheds more fundamental light about the role played by swelling, plasticization and clustering. Although swelling and plasticization are often considered synonymous, there are substantial differences between the two terms. Indeed, while swelling is an increase in the polymer specific volume caused by the Henry's mode penetrant sorption, plasticization indicates a decrease in polymer chain packing accompanied by: *i*) an increase in polymer chain mobility, *ii*) a drop in separation efficiency, and *iii*) a drop in glass transition temperature and mechanical stability [29, 80-83, 92]. Therefore, while polymer swelling does not necessarily imply plasticization, plasticization is always a consequence of polymer swelling. The analysis of penetrant diffusion coefficients as a function of concentration or activity provides useful information about the plasticization onset. Indeed, when polymer plasticization

occurs, penetrant diffusion coefficient increases exponentially with increasing concentration [45, 83, 93].

**Table 4.** Dual mode parameters obtained by fitting methanol concentration in Celazole<sup>®</sup> vs. pressure (expressed in atm). Dual mode parameters for methanol sorption in PIM-1 at 25°C [29] are reported for the sake of comparison.

	$k_D$ (cm <sup>3</sup> (STP)/cm <sup>3</sup> atm)	$C'_H$ (cm <sup>3</sup> (STP)/cm <sup>3</sup> )	$b$ (atm <sup>-1</sup> )	source
Celazole <sup>®</sup> /methanol	1231.8 ± 74.85	85.25 ± 10.68	216.6 ± 62	this study
PIM-1/methanol	1395	88.6	76.1	[29]

Methanol diffusion coefficients in Celazole<sup>®</sup> are reported in Fig. 15B as a function of concentration. They were estimated from the analysis of vapor and liquid sorption kinetics using the Berens-Hopfenberg [44] model (cf. Fig. S5, Supporting Information). These diffusion coefficients must be interpreted as average values over the concentration range corresponding to each sorption step. A collection of experimental methanol sorption kinetics in Celazole<sup>®</sup> at different activities, and the corresponding Berens-Hopfenberg modeling, is reported in Fig. S5, Supporting Information.

Noteworthy, a variable film thickness was considered for the analysis of sorption kinetics. Specifically, the film thickness was assumed to change linearly as a function of activity between the dry value (at activity 0) and the swollen value (at activity 1). The same method was used by Lively et al. to describe dimethylformamide and methanol vapor diffusion in PIM-1 [29]. Direct

measurement of polymer thickness as a function of activity is not possible, as it would require experimental techniques, such as ellipsometry, that are not accessible at this stage. The thickness of several Celazole<sup>®</sup> films was measured with a digital micrometer after swelling in liquid methanol at 25°C. Then, films were dried under vacuum for 24h at 140°C and the dry thickness was measured. The membrane thickness changed by about +10% upon swelling in methanol. Gratifyingly, dilation in the thickness direction agrees reasonably with that measured in the width and length directions during methanol sorption (i.e.,  $\cong 13\%$ ). PIM-1 exhibits a +20% change in thickness upon swelling in liquid methanol [29].

Methanol diffusion coefficient in Celazole<sup>®</sup> increases by almost 5 orders of magnitude in the activity range 0-1, which is indicative of severe polymer plasticization [94-96]. The combined analysis of sorption and diffusion isotherms sheds fundamental light on the role played by matrix plasticization and penetrant clustering. Both phenomena are compatible with the upturn exhibited by the methanol sorption isotherm at high activities. However, plasticization and clustering produce opposite effects on the diffusion coefficient. Specifically, polymer plasticization causes an exponential increase in diffusivity with concentration, while penetrant clustering causes a decrease in diffusivity [43, 45, 97, 49]. The analysis of Fig. 15B indicates that matrix plasticization overwhelms penetrant clustering. The Zimm-Lundberg model was used to assess the extent of penetrant clustering (cf. Fig. S6, Supporting Information). Since the Zimm-Lundberg clustering integral is negative over the entire activity range 0-1, occurrence of methanol clustering should be ruled out. However, these results must be interpreted cautiously, since the conclusions of the Zimm-Lundberg model are often in conflict with experimental spectroscopic data [98]. In fact, as reported by Elabd and co-workers [98], while the Zimm-Lundberg model does not predict water clustering in poly(vinylpyrrolidone) in the activity range 0-1, FTIR spectroscopy indicates that

moderate clustering takes place at high activities. FTIR experiments combined with the analysis of activation energies of diffusion in Celazole<sup>®</sup> are analyzed in more detail in sections 4.2.7 – 4.2.10.

For a more fundamental understanding of the role of plasticization and clustering, diffusion coefficients must be corrected for thermodynamic non-idealities [1, 29, 33]. In fact, since the mobility coefficient  $L$  measures the frictional resistance offered by the polymer to penetrant diffusion, it is more directly related to the free volume of the polymer-penetrant mixture, as well as to penetrant clustering, than the diffusion coefficient. In this study, correction of diffusion coefficients for thermodynamic non idealities has been done in two ways. First, experimental sorption data were used to evaluate numerically the derivative appearing in Eq. 19 (i.e.,  $\frac{\partial \ln a}{\partial \ln \omega_{pen}}$ ).

As a double check,  $\alpha$  was also calculated using the dual mode model (cf. Eq. 20). As shown in Fig. 16B, the two methods provided similar results.

In Fig. 16A-B, the methanol mobility coefficient (i.e., the thermodynamically corrected methanol diffusion coefficient in Celazole<sup>®</sup>) and the thermodynamic factor are reported as a function of methanol concentration. Thermodynamic factors larger than one indicate favorable (i.e., attractive) polymer-penetrant interactions. At low activity, the thermodynamic factor for the system Celazole<sup>®</sup>-methanol is very close to 3 and it decreases with increasing activity. This result is consistent with the picture that polar alcohol -OH groups can interact favorably with polar -NH groups on the polymer backbone, likely by forming hydrogen bonds. The decrease of thermodynamic factor with increasing penetrant concentration has been reported for several polymer-penetrant systems and indicates that penetrant chemical potential is less sensitive to concentration at high activities [49]. From the physical point of view, the decrease of  $\alpha$  with



activity (i.e., concentration) might indicate that polymer-penetrant interactions become less likely at high concentrations, owing to the progressive reduction of interaction sites.

The thermodynamically corrected diffusion coefficient, i.e., the mobility coefficient  $L$ , is significantly lower than  $\bar{D}$  at low concentrations, and it becomes closer to  $\bar{D}$  at high concentrations, where  $\alpha \rightarrow 1$  (cf. Fig. 16A). The overall trend of diffusion coefficients with concentration and its physical interpretation is not altered after correction for thermodynamic non-idealities. Since the mobility coefficient increases by 5 orders of magnitude in the activity range 0-1, we can conclude that methanol sorption severely plasticizes Celazole<sup>®</sup>. This conclusion supports the interpretation of mixed methanol-PEG400 sorption data presented in section 4.2.3.

The mobility coefficient depends exponentially on concentration [45, 51, 52, 99]:

$$L = L_0 \exp(\beta C) \quad (\text{Eq. 41})$$

where  $L_0$  is the mobility coefficient at infinite dilution (i.e., at vanishing concentration),  $C$  is the penetrant concentration expressed in units of  $\text{cm}^3(\text{STP})/\text{cm}^3\text{polymer}$ , and  $\beta$  is the plasticization factor. The exponential fitting of mobility data in Fig. 16A gives a value of  $\beta$  equal to 0.044 ( $\text{cm}^3\text{polymer}/(\text{cm}^3(\text{STP}))$ ) for the mixture Celazole<sup>®</sup>/methanol at 25°C. For the mixture Celazole<sup>®</sup>/water at 35°C, Moon et al. reported a value of  $\beta$  equal to 0.017( $\text{cm}^3\text{polymer}/(\text{cm}^3(\text{STP}))$ ) [52]. Even though the two datasets are available at different temperatures, the comparison indicates that methanol is a stronger plasticizing agent than water for Celazole<sup>®</sup>.

Interestingly, Celazole<sup>®</sup> and PIM-1, two rigid polymers of great interest for OSN applications, exhibit opposite behaviors in the presence of methanol vapor. Indeed, if methanol acts as a plasticizer for Celazole<sup>®</sup>, it swells, but does not plasticize PIM-1 [29]. Such different behavior is

likely related to differences in polymer-penetrant interactions, as well as in fractional free volume (FFV = 29% for PIM-1 and 12% for Celazole<sup>®</sup>).

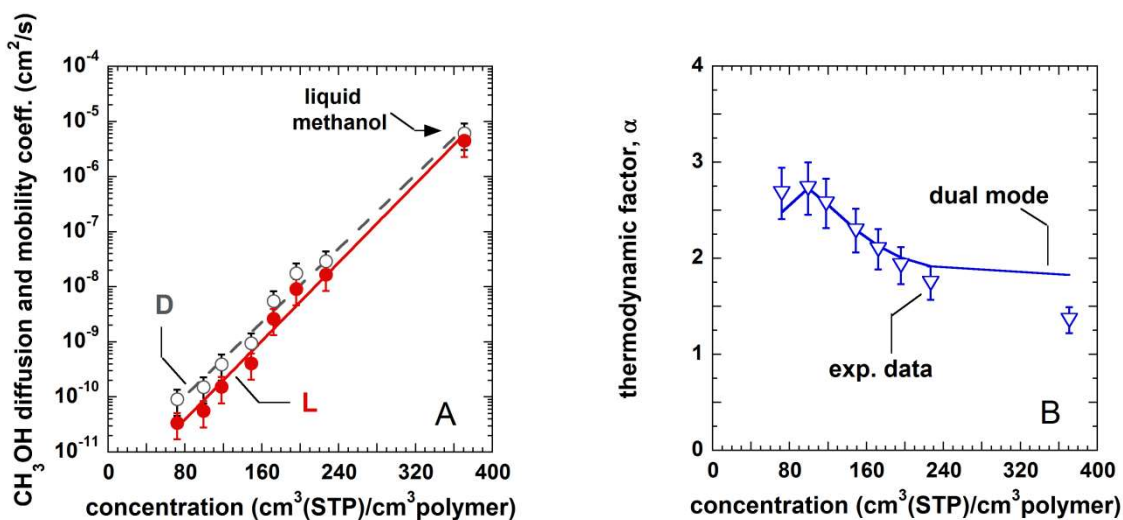


**Figure 16.** A) Methanol mobility coefficient (i.e., thermodynamically corrected diffusion coefficient, filled red circles) in Celazole<sup>®</sup> at 25°C as a function of concentration. Concentration-averaged diffusion coefficient (open grey circles) is reported for the sake of comparison. B) Thermodynamic factor,  $\alpha$ , at 25°C as a function of concentration. Open triangles represent the thermodynamic factor calculated directly from experimental data. Continuous blue line represents the thermodynamic factor calculated from the dual mode model (cf. Eq. 20).

In Fig. S3-B, Supporting Information, the thermodynamically corrected methanol diffusion coefficients (i.e., mobility) at 25°C in Celazole<sup>®</sup> and PIM-1 are reported as a function of concentration. At low-moderate concentrations, methanol mobility in PIM-1 exceeds that in Celazole<sup>®</sup> by three orders of magnitude. This result is consistent with the much larger fractional

free volume exhibited by PIM-1 (i.e., 29%) relative to Celazole<sup>®</sup> (i.e., 12%). However, methanol mobility in PIM-1 decreases with increasing concentration, which is indicative of penetrant clustering or blocking [112, 100, 101]. Blocking refers to the progressive filling of the free volume available for penetrant transport [112, 100, 101]. Therefore, as concluded by Lively and co-workers, methanol does not plasticize PIM-1 [29]. In contrast, methanol mobility in Celazole<sup>®</sup> increases with increasing concentration and, at activities larger than 0.6, it surpasses that in PIM-1. As discussed in section 4.2.5, this result can be rationalized based on the free volume theory. Methanol permeability in Celazole<sup>®</sup> at 25°C, calculated from the solution-diffusion model (i.e.,  $\bar{D} \times S$ ), increases by two orders of magnitude with activity (cf., Fig. S7, Supporting Information), which confirms the occurrence of severe polymer plasticization.

We have hypothesized the possible mechanism of Celazole<sup>®</sup> plasticization (cf., Fig. 17). Specifically, methanol (as well as other polar penetrants) likely break the inter-chain hydrogen bonds in favor of polymer-penetrant hydrogen bonds, according to a mechanism that we could define as competitive hydrogen bonding. The breaking of the original polymeric network would increase, in turn, the distance between polymer chains, thus enhancing their mobility. This phenomenon, obviously, does not occur when Celazole<sup>®</sup> is exposed to non-polar penetrants. Hodge et al. drew a similar conclusion to explain polyvinyl alcohol plasticization during water sorption [102].

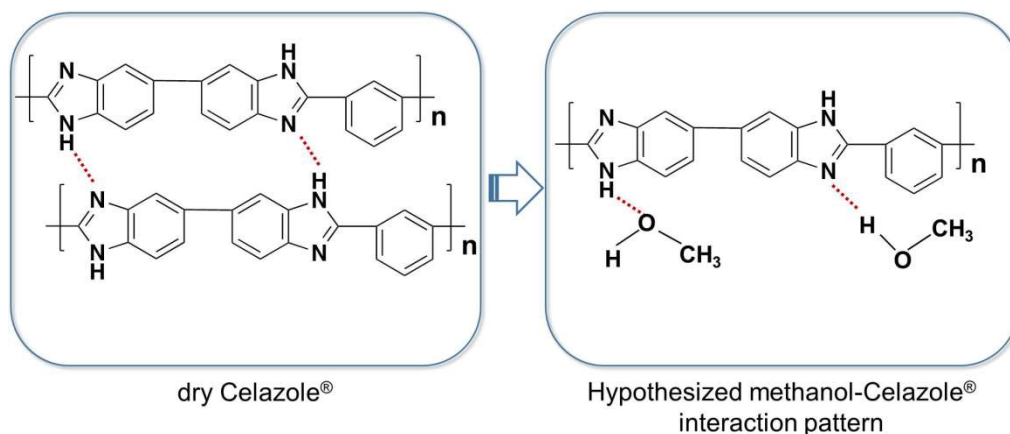


**Figure 17.** Hypothesized methanol-Celazole<sup>®</sup> interaction pattern [52, 68, 103, 104]. Red tracks indicate hydrogen bonds. Due to steric hindrance, the actual interaction could be different. FTIR experiments and molecular simulations are underway to: i) confirm this hypothesis, and ii) prove the occurrence of competitive hydrogen bonding.

Disruption of inter-chain hydrogen bonding upon methanol sorption is compatible with the conclusions drawn by Musto et al. [68] in their study of water transport in Celazole<sup>®</sup>, and is further confirmed by mechanical properties measurements (cf. section 4.2.6).

**4.2.5 Fractional free volume analysis.** In glassy polymers, penetrant molecules execute diffusion jumps through free volume elements. The amount of free volume available for penetrant transport can be calculated using the Bondi's rule [93]:

$$FFV = \frac{\hat{V}_{pol} - 1.3\hat{V}^{vDw}}{\hat{V}_{pol}} \quad (\text{Eq. 42})$$

where  $\hat{V}_{pol}$  is the polymer bulk specific volume and  $1.3\hat{V}^{vDw}$  is the volume occupied by polymer chains ( $0.693 \text{ cm}^3/\text{g}$  for Celazole<sup>®</sup> [52]).  $\hat{V}^{vDw}$ , in turn, represents the so-called Van der Waals volume, which can be calculated using the group contribution method [105]. Based on the free volume theory, penetrant mobility and permeability increase exponentially with FFV [106]. A

relevant question is: how does the Celazole<sup>®</sup> FFV change upon solvent sorption? There are two ways to calculate changes in free volume induced by penetrant sorption in glassy polymers. If we assume that the sorption process is simply a void-filling mechanism, the amount of free volume available for penetrant transport should decrease with increasing penetrant activity, due to the progressive occupation of Langmuir's sites. The implicit assumption underlying this mechanism is that the volume occupied by the penetrant is excluded from the total free volume, i.e., it is inaccessible to other penetrant molecules. If this assumption was correct, the mobility coefficient should decrease with increasing penetrant concentration in the polymer, which is inconsistent with the experimental data shown in Fig. 16A. As discussed by Moon et al. [52], diffusion or mobility coefficients can be more conveniently correlated with penetrant-accessible fractional free volume, which is defined as follows:

$$FFV_{acc} = \frac{\hat{V} - 1.3\hat{V}^{vDv} (1 - \omega_{pen})}{\hat{V}} \quad (\text{Eq. 43})$$

where  $\omega_{pen}$  is the penetrant mass fraction in the polymer and  $\hat{V}$  is the actual specific volume of the penetrant/polymer mixture. This definition of fractional free volume assumes that the volume occupied by the penetrant is included in the overall free volume, i.e., that occupied and non-occupied free volume are equally accessible to penetrant molecules [52]. Here, Eq. 43 was used to calculate the methanol-accessible free volume at activities 0 and 1. The actual specific volume of the methanol/polymer mixture,  $\hat{V}$ , at activity 1 was calculated by coupling liquid methanol sorption and dilation data:

$$\hat{V} = \frac{1 + \frac{\Delta V}{V_0}}{\rho_p \left( 1 + \frac{M_{wl} C}{22,414 \rho_p} \right)} \quad (\text{Eq. 44})$$

where  $\frac{\Delta V}{V_0}$  is the polymer volume dilation (i.e.,  $\left(\frac{\ell}{\ell_0}\right)^3 - 1$ ),  $\rho_p$  is the density of dry, unpenetrated Celazole<sup>®</sup> (i.e., 1.27 g/cm<sup>3</sup>),  $M_{wl}$  is the penetrant molar mass, and  $C$  is the penetrant concentration expressed in units of cm<sup>3</sup>(STP)/cm<sup>3</sup>polymer. Since dilation data are not currently available over the entire activity range, we can only calculate the methanol-accessible fractional free volume at activity 0 (where no dilation takes place and  $C = 0$ ) and activity 1 (where  $\frac{\Delta V}{V_0} = 0.44$  and  $C = 363$  cm<sup>3</sup>(STP)/cm<sup>3</sup>polymer). Interestingly, the methanol-accessible free volume increases from 0.12 at activity 0 to 0.38 at activity 1. This result is consistent with the large increase in mobility coefficient with activity (cf. Fig. 16A). Chung and co-workers used PALS (Positron Annihilation Lifetime Spectroscopy) to demonstrate that the free volume of Celazole<sup>®</sup> films increases by a factor of 2.8 after exposure to liquid methanol. This result is in good agreement with the 3-fold increase estimated in this study.

The Celazole<sup>®</sup> accessible free volume upon exposure to several liquids is reported in Fig. 18 as a function of the mass-based solubility. Interestingly,  $FFV_{acc}$  exhibits a fairly linear trend with concentration. Polar penetrants cause a much larger increase in accessible free volume relative to non-polar penetrants, which is consistent with the competitive hydrogen bonding mechanism described in section 4.2.4.

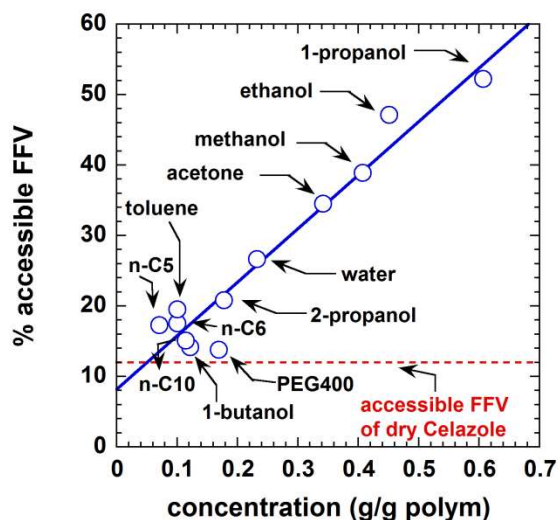


**Figure 18.** Polymer accessible fractional free volume upon exposure to several organic liquids and water at 25°C. Symbols are calculations from Eqs. 30-31, using experimental sorption and dilation data. The continuous, blue line is a linear interpolation. The dry polymer accessible FFV is also reported (red dashed line) for comparison.

4.2.6 Mechanical properties. The Young's modulus and the elongation at break of Celazole<sup>®</sup> samples previously equilibrated in water and methanol at 25°C are shown in Figs. 19. A collection of mechanical properties is also reported in Table 5. Dry samples, to be used as baseline, were tested as well. As shown in Fig. S1, Supporting Information, if thick membrane samples are used, solvent evaporation is negligible. The evaporative methanol loss from a 200 μm thick sample upon exposure to air at room temperature for 5 minutes is about 5%. Since the samples used for the mechanical test were about 200 μm thick and the time needed to mount the specimen and run the test is about 6 minutes, we can conclude that the data reported in Fig.19 and Table 5 reflect the actual mechanical properties of Celazole<sup>®</sup> samples equilibrated in liquid methanol and water.

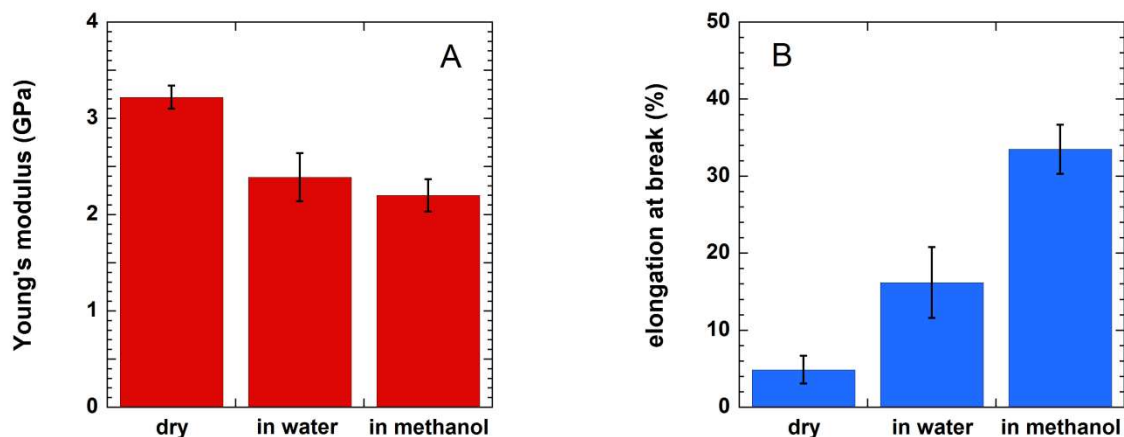


**Figure 19.** Young's modulus (A) and elongation at break (B) of Celazole<sup>®</sup> before and after exposure to liquid water and methanol at 25°C.

Since methanol uptake is higher than water uptake (28.9% vs. 18.8% wt), methanol is expected to be a stronger plasticizing agent than water for Celazole<sup>®</sup>. The Young's modulus decreases by about 31.5% and 25.5% upon exposure to methanol and water, respectively. Such loss in rigidity is compatible with polymer plasticization [107]. In contrast, the elongation at break increases by 586% and 232% upon exposure to methanol and water, respectively. This result indicates that Celazole<sup>®</sup> becomes more deformable upon exposure to polar liquids, which, again, is compatible with polymer plasticization [85]. As noted by other researchers, sorption-induced polymer plasticization influences the elongation at break much more than the Young's modulus [85, 107].

**Table 5.** Mechanical properties of Celazole<sup>®</sup> before and after exposure to liquid water and methanol at 25°C. Uncertainties were estimated from the standard deviation of several measurements.



	Young's modulus (GPa)	elongation at break (%)	ultimate stress (MPa)
Celazole <sup>®</sup> (dry)	3.22 ± 0.12	4.88 ± 1.8	109 ± 2.30
Celazole <sup>®</sup> + water	2.40 ± 0.25	16.2 ± 4.6	66.5 ± 13.4
Celazole <sup>®</sup> + methanol	2.20 ± 0.17	33.5 ± 3.2	51.9 ± 8.91

#### 4.2.7 Methanol sorption in PBI at multiple temperatures

Methanol sorption isotherms in PBI at 25, 35 and 45°C are shown in Fig. 20A as a function of methanol activity,  $a$  (i.e.,  $a = \frac{p}{p_0}$ , where  $p$  is the final equilibrium pressure, and  $p_0$  is the vapor pressure at the experimental temperature).

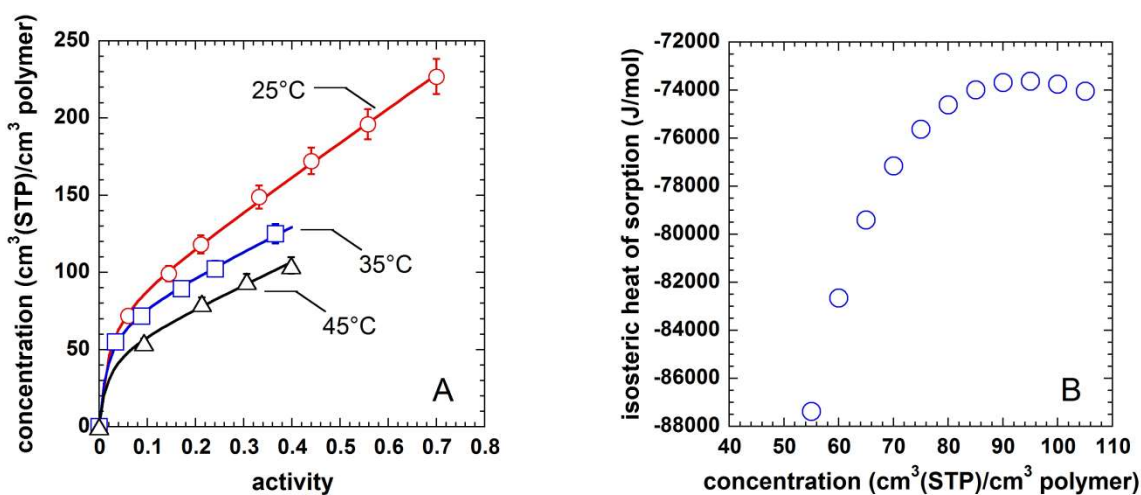


**Figure 20.** A) Methanol vapor sorption in PBI as a function of activity and temperature. B) Isosteric heat of sorption as a function of methanol concentration in PBI.

The uncertainty of sorption data was calculated using the error propagation method, and is about 5% [75]. Sorption isotherms exhibit, in the activity range investigated and at all temperatures, the dual mode behavior typical of glassy polymers. The dual mode parameters at 25, 35 and 45C,

obtained by fitting Eq. 7 to the experimental sorption isotherms, are shown in Table 6. To reduce the degrees of freedom, the dual mode fitting of sorption data at 25°C was unconstrained, that is, the three dual mode parameters were left unconstrained. Sorption data at 35 and 45°C were fit by assuming  $C'_H$  equal to its value at 25°C, while  $k_D$  and  $b$  were left unconstrained. This assumption relies on the fact that the PBI glass transition temperature is extremely high [62, 113, 68] ( $\cong 417^\circ\text{C}$ ), therefore, in view of the highly rigid structure of this polymer, characterized by fused ring with limited chain rotation freedom, no change in excess free volume (i.e., in  $C'_H$ ) is expected to take place between 25 and 45°C.  $k_D$  and  $b$  decrease with increasing temperature, which is consistent with previous literature reports [70, 108].

**Table 6.** Dual mode parameters of the system methanol/PBI at 25, 35 and 45°C. Uncertainty were calculated as using the error propagation method [109].

T (°C)	$k_D$ cm <sup>3</sup> (STP)/cm <sup>3</sup>	$C'_H$ cm <sup>3</sup> (STP)/cm <sup>3</sup>	$b$
25	209.72 ± 12.7	83.45 ± 6.7	38.72 ± 4.0
35	120.17 ± 7.0	83.45 ± 6.7	37.86 ± 4.0
45	86.43 ± 5.2	83.45 ± 6.7	13.45 ± 2.0

As expected, methanol sorption in PBI decreases with increasing temperature, which indicates that the sorption process is exothermic [40]. The isosteric heat of sorption was calculated as discussed in section 2.1, and it is shown in Fig. 20B as a function of methanol concentration in the polymer. Noteworthy, the sorption enthalpy is strongly negative ( $< -75$  kJ/mol). Lively et al. reported that the enthalpy of methanol sorption in PIM-1 is about -40 kJ/mol [29]. The larger exothermic effect observed in PBI is ascribed to the highly favorable energetic interaction of

methanol with the PBI backbone. Specifically, methanol molecules can form hydrogen bonds with N-H groups on the imidazole ring, which breaks the original hydrogen bonded structure of PBI and favors polymer swelling and plasticization. This aspect has been analyzed via FTIR spectroscopy and is discussed in section 4.10.

Interestingly, the heat of sorption in PIM-1 is very close to the heat of methanol condensation (i.e., -39 kJ/mol), which means that methanol sorption in PIM-1 can be envisaged as the penetrant condensation in the excess free volume, with essentially no interaction with the polymer (i.e.,  $\Delta H_{mix} \approx 0$ ) [116]. In contrast, the heat of sorption in PBI is much more negative than the heat of condensation, which implies that  $\Delta H_{mix}$  is largely negative, and confirms the favorable polymer-penetrant mutual interaction [37, 40].

Equally important, the isosteric heat of methanol sorption in PBI increases with increasing methanol concentration, indicating that the sorption process becomes less exothermic at higher activity. This behavior is ascribed to the polymer swelling, during which polymer chains are pulled apart to create additional room to accommodate penetrant molecules. The latter process is strictly endothermic, as energy is required to deform the polymer structure, which justifies the increase of isosteric heat of sorption with concentration [37, 40]. In this study, polymer swelling and plasticization during methanol sorption have been assessed quantitatively via FTIR spectroscopy.

As discussed in section 4.2.4, methanol diffusion coefficients in PBI at 25°C increase by almost three orders of magnitude with increasing activity in the range 0-0.7, which provides strong evidence for polymer plasticization. Barometric sorption kinetics at 35 and 45°C were noisy, therefore we could not estimate diffusion coefficients at these temperatures.

#### 4.2.8 Use of FTIR spectroscopy to shed fundamental details on the mechanism of plasticization of OSN membranes

PBI spectra in its dry state, as well as upon equilibration in methanol vapor at different activities are shown in Fig. 21. Characteristic signals of sorbed methanol are apparent in the range 3700 – 2300  $\text{cm}^{-1}$  and at 1028  $\text{cm}^{-1}$ . The high-frequency band displays a complex shape and exhibits several components.

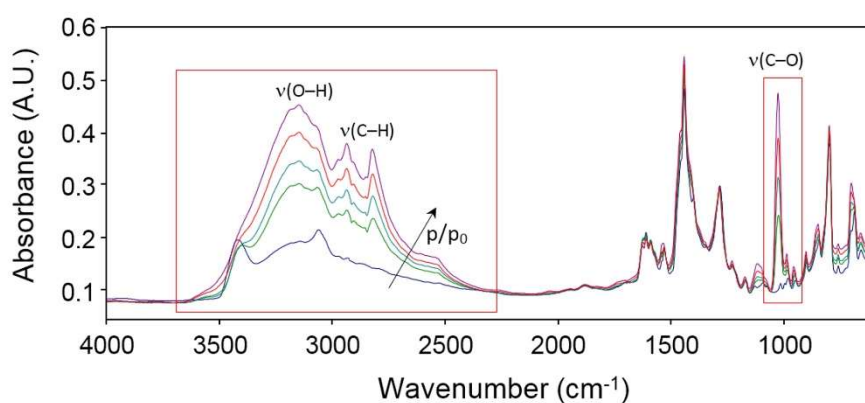


**Figure 21.** FTIR transmission spectra in the frequency range 4000 – 450  $\text{cm}^{-1}$  of dry PBI (blue trace) and PBI equilibrated at increasing activities of methanol vapor.  $p/p_0$  values, from the bottom trace up, are: =0, 0.1, 0.3, 0.5, 0.7.

The curve fitting analysis (cf. Figs. S3A-B, Supporting Information) shows that the dry spectrum can be suitably simulated by a minimum of 4 components, which reflects the presence, in the amorphous phase, of regions differing by density and average d-spacing [68]. The occurrence of a mesophase has also been suggested as a result of a detailed vibrational analysis of the PBI peak at 3424  $\text{cm}^{-1}$ . In the sample equilibrated with methanol vapor (cf. Fig. S11B, Supporting Information) the three components at lower frequencies (3195, 2930, 2545  $\text{cm}^{-1}$ ) increase concurrently with methanol uptake, while the sharper peak originally at 3424  $\text{cm}^{-1}$  is barely

affected. The lack of resolution prevents a more detailed analysis. It can be inferred, from the multiplicity of  $\nu(\text{OH})$  components, that several methanol species are present, which are involved in different kinds of H-bonding interactions, both with the polymer matrix and with themselves, giving rise to dimer/multimer species (that is, clustering) [52, 114]. However, as discussed in section 4.2.4, since methanol diffusion coefficient in PBI increases with increasing activity (i.e., methanol concentration), it can be inferred that plasticization overwhelms clustering (cf. Fig. 24E). The latter, indeed, would cause a marked decrease of diffusion coefficient with concentration.

The  $\nu(\text{OH})/\nu(\text{NH})$  region does not provide direct evidence of the breaking of PBI self-association linkages ( $\text{N-H}\cdots\text{N}$ ) by methanol through the formation of competitive interactions of the type  $\text{N-H}\cdots\text{O}$  and/or  $\text{O-H}\cdots\text{N}$ . This is a relevant issue, since the PBI mechanical, thermal and transport properties are strictly related to the cross-link density of the H-bonding network. The analysis presented in section 4.10 will shed fundamental light on this aspect.

Sorbed methanol also shows the typical  $\nu(\text{CH}_3)$  pattern below  $3000\text{ cm}^{-1}$  which, according to its vibrational origin, is insensitive to molecular interactions [52]. The third significant signal of the probe molecule is observed as a single, intense band at  $1028\text{ cm}^{-1}$ . It is often referred to as a  $\nu(\text{C-O})$  vibration, but it is, in fact, a coupled mode with minor contributions from  $\text{H-C-O}$  and  $\text{C-O-H}$  bending. Being next to the interaction site, the CO linkage displays a limited sensitivity to H-bonding in comparison to the OH bond itself, which is reflected in a relatively sharp, quasi-symmetrical band shape of its stretching mode (cf. inset in Fig. 23). This inertness makes it a good candidate for quantitative analysis, since an average value of molar absorptivity can be assumed for the different molecular species. In fact, Fig. 22 demonstrates that the  $1028\text{ cm}^{-1}$  peak correlates linearly with both methanol concentration and optical path-length (sample thickness)

according to the Beer-Lambert relationship. This correlation warrants the conversion of the photometric observable (absorbance) into absolute concentration values. The absorbance/concentration calibration curve was built by considering the experimental sorption data collected barometrically at 25°C and the FTIR data collected at the same temperature. Prior to building the normalized absorbance/concentration calibration curve (cf. Fig. 22), a correction was applied to the experimental barometric sorption data, to account for the residual water left in the sample after drying at 25°C for 24 h under vacuum. Indeed, as mentioned earlier, the PBI sample could not be completely dried at 150°C prior to the barometric sorption measurements. The amount of residual water was estimated spectroscopically and it is 2.5 wt. % [62]. The slope of the absorbance-concentration plot shown in Fig. 22 affords an accurate evaluation of the molar absorptivity of the analytical peak, which is equal to 16.9 km/mol.

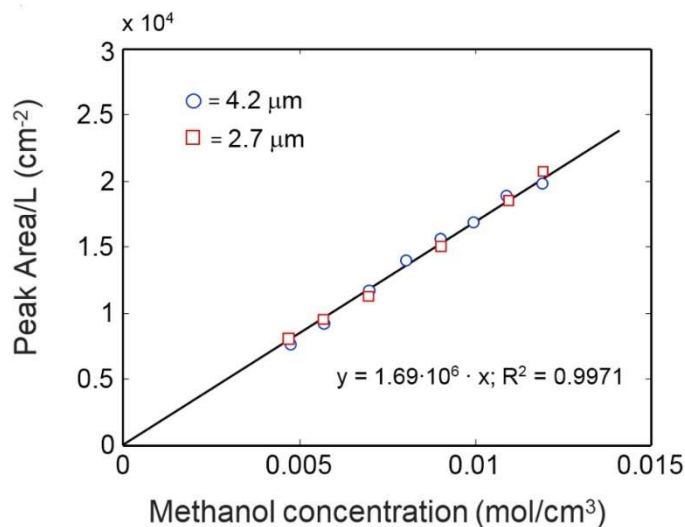


**Figure 22.** Normalized absorbance vs. concentration diagram. The two data sets refer to PBI films of different thickness.

#### 4.2.9 Sorption equilibrium and kinetics obtained via FTIR spectroscopy

Fig. 23 shows the methanol sorption isotherm in PBI, evaluated from the intensity of the peak at  $1028\text{ cm}^{-1}$ , normalized by the sample thickness. The shape of the FTIR sorption isotherm is comparable with that from barometry. To provide a quantitative comparison between the two techniques, it is important to note that, if the dual-mode model is expressed in terms of absorbance in place of concentration, the relative parameters  $\bar{k}_D$  and  $\bar{C}'_H$  correspond, respectively, to  $k_D \varepsilon L$  and  $C'_H \varepsilon L$ , while the parameter  $b$  remains invariant. To compare the  $b$  values from barometry and spectroscopy, barometric sorption data were corrected to remove the contribution of residual water. Indeed, as mentioned earlier, the sample used for sorption experiments could not be dried at  $150^\circ\text{C}$ , so it contains 2.5%wt. of residual water. After this correction, the  $b$  values from barometry and spectroscopy are in good agreement (i.e.,  $65 \pm 20$  and  $57 \pm 20$ , respectively). Analogously, the molar absorptivity values calculated from  $\bar{k}_D$  and  $\bar{C}'_H$  are  $17 \pm 3\text{ km/mol}$  and  $16 \pm 3\text{ km/mol}$ , respectively, which are in excellent agreement with the direct estimate from the absorbance – concentration diagram (i.e.,  $16.9\text{ km/mol}$ ). The dual mode parameters are summarized in Table 7. For the sake of comparison, the dual mode parameters for the system PBI/H<sub>2</sub>O are reported as well.

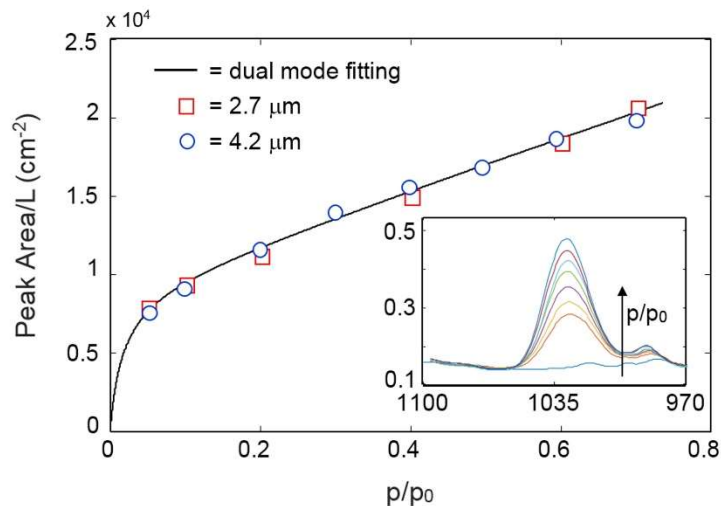


**Figure 23.** Methanol sorption isotherm in PBI at 25°C. The continuous line is the least-squares regression of the experimental data with the dual-mode model. The inset represents the analytical peak at 1028  $\text{cm}^{-1}$  at the different vapor activities for the 4.2  $\mu\text{m}$  thick film.

**Table 7.** Dual mode parameters for methanol and water vapor sorption and dilation in PBI

	PBI/methanol spectroscopy <sup>a</sup>	PBI/methanol barometry (corrected) <sup>b</sup>	PBI/H <sub>2</sub> O barometry <sup>b</sup> [62]
T (°C)	25	25	35
$k_D$	$(1.6 \pm 0.2) \times 10^4$	$(9.3 \pm 0.7) \times 10^{-3}$	$(9.6 \pm 0.3) \times 10^{-3}$
$C'_H$	$(9.1 \pm 0.1) \times 10^3$	$(5.5 \pm 0.5) \times 10^{-3}$	$(4.6 \pm 0.2) \times 10^{-3}$
$b$	$57 \pm 20$	$65 \pm 20$	$37 \pm 10$
$V_D$ ( $\text{cm}^3/\text{mol}$ )	$10 \pm 1$	-	$10.8 \pm 0.3$
$f$	$0.62 \pm 0.06$	-	$0.33 \pm 0.03$

<sup>a</sup>  $k_D$  and  $C'_H$  in  $\text{cm}^{-2}$ ;

<sup>b</sup>  $k_D$  and  $C'_H$  in  $\text{mol}/\text{cm}^3$ .  $b$  and  $f$  are dimensionless. Barometric methanol sorption data were corrected to remove the contribution of residual water.

Time-resolved FTIR measurements allowed to investigate methanol sorption kinetics in PBI. Experimental sorption kinetics from differential and integral sorption tests over several activity ranges are shown in Fig. 24A-B-C-D, where the continuous lines represent the best fit of the Berens–Hopfenberg model to the experimental kinetics.

The kinetic behavior of the system is always non-Fickian and is strongly dependent on methanol concentration (i.e., activity). For the two integral tests at  $p/p_0 = 0.05$  and 0.1, the mechanism is



pseudo-Fickian, i.e., the Fickian contribution strongly prevails over relaxation. At higher activities, the sorption process shows a typical dual-stage behavior. The initial plateau is attained almost instantaneously, while the final pseudo-equilibrium is attained over much longer times [110, 111, 115, 116]. Polymer relaxation is promoted by the penetrant, which likely dissociates the H-bonding self-interactions in PBI, thus increasing the polymer chain mobility. The shapes of the kinetic curves are very close to those reported by Petropoulos et al. for the system acetone/cellulose [110]. Also in the latter case the polymer matrix is self-associated and the penetrant is supposed to break the H-bonding self-interactions. The Berens-Hopfenberg model parameters in the activity range 0 – 0.4 are summarized in Table 8. At activities higher than 0.4 the diffusion and relaxation stages cannot be easily de-convoluted, therefore we did not attempt to model sorption kinetics in this activity range. The  $\alpha$  value (i.e. the relative amount of penetrant sorbed during the relaxation stage) exhibits a step change above  $p/p_0 = 0.1$ , which marks the start of the dual-stage behavior. At higher activities  $\alpha$  increases slightly to reach 0.8 at  $p/p_0 = 0.3$ , confirming that, above  $p/p_0 = 0.1$  the matrix relaxation is the controlling feature. The relaxation time,  $\tau$ , increases exponentially with penetrant concentration.

**Table 8.** Berens–Hopfenberg parameters and concentration-averaged diffusivity at 25°C and different activities.

$p/p_0$ (from-to)	concentration (mol/cm <sup>3</sup> )	$\bar{D}$ (cm <sup>2</sup> /s)	$\tau$ (s)	$\alpha$
0.00-0.05	0.0023	3.3E-12	3.8 x 10 <sup>4</sup>	0.3
0.00-0.10	0.0050	8.0E-12	2.6 x 10 <sup>4</sup>	0.2
0.10-0.20	0.0062	7.0E-11	5.2 x 10 <sup>4</sup>	0.7

0.20-0.30	0.0076	1.2E-10	9.5 x 10 <sup>4</sup>	0.8
0.30-0.40	0.0088	2.3E-10	14.3 x 10 <sup>4</sup>	0.8

The trend of the Fickian diffusivity at 25°C as a function of concentration (cf. Fig. 24E) is consistent with the results of barometric sorption experiments. However, diffusion coefficients retrieved via FTIR experiments are about one order of magnitude lower compared to those obtained during barometric sorption experiments (cf. Fig. 24E). This discrepancy may originate from the different drying protocol. Indeed, the sample used for FTIR measurements was pre-treated at 150°C, which could produce a rearrangement (i.e., a densification) of the polymer structure. In contrast, the sample used for barometric sorption experiments was dried at 25°C, and it contains some residual water bonded to the polymer backbone. We have observed that the presence of residual water significantly accelerates methanol sorption in PBI (cf. Fig. S13, Supporting Information). The physical picture sketched above is consistent with the larger diffusion coefficients measured during barometric sorption experiments.

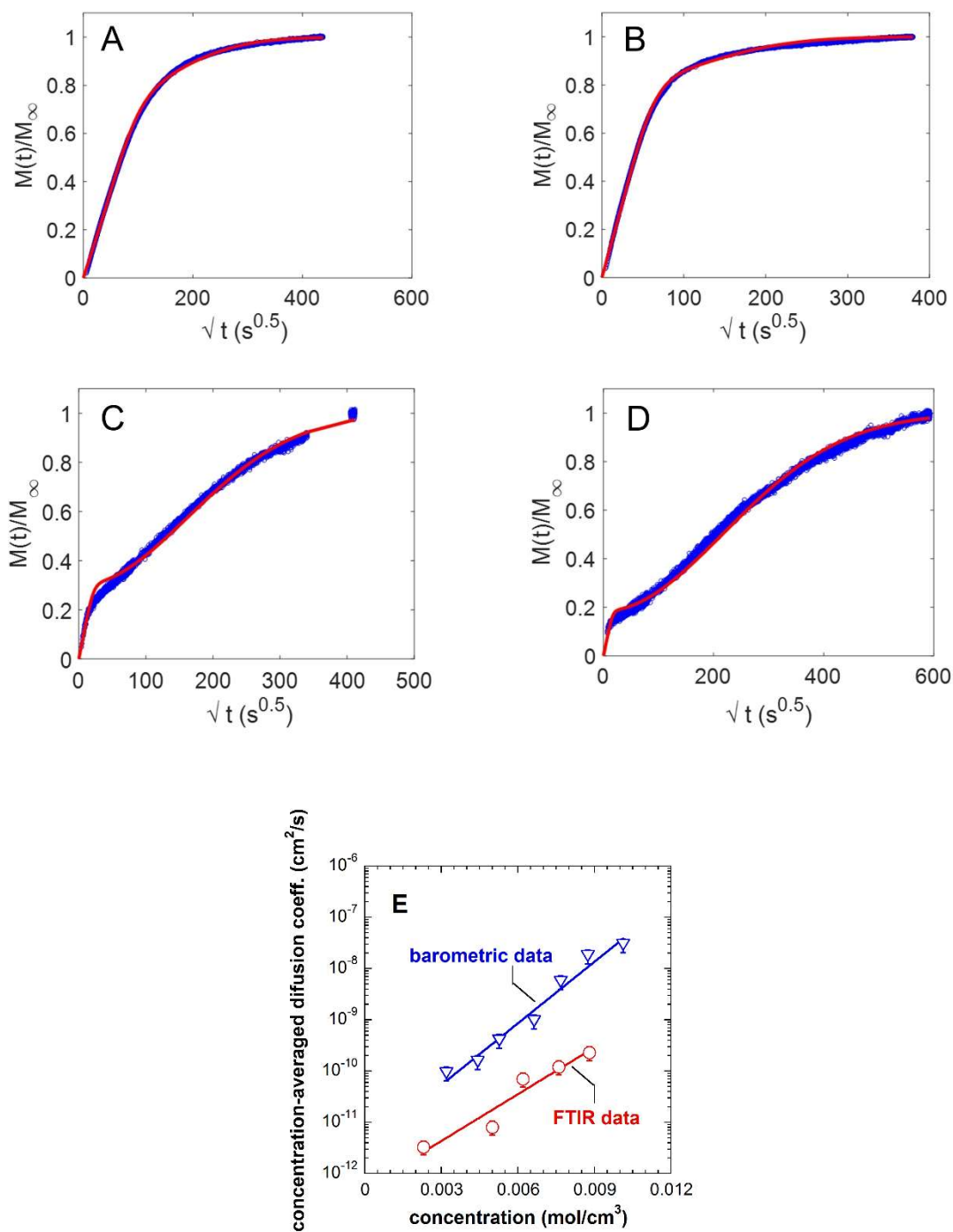


**Figure 24.** Methanol sorption kinetics in PBI at 25°C. A) Integral test at  $p/p_0 = 0.05$ . B) Integral test at  $p/p_0 = 0.10$ . C) Differential test  $p/p_0 = 0.10 - 0.20$ . D) Differential test  $p/p_0 = 0.20 - 0.30$ . Blue symbols are the experimental data, and continuous lines represent the least-squares fit of

*the experimental data with the Berens–Hopfenberg model. E) Barometric and FTIR diffusion coefficient as a function of methanol concentration in PBI at 25°C. Uncertainty was calculated using the error propagation method [75].*

Noteworthy, methanol sorption kinetics in other rigid glassy polymers, such as 6FDA-ODA polyimide and Ultem<sup>®</sup> polyetherimide are essentially Fickian with a diffusion coefficient variable with concentration [52]. The strong relaxation stage observed during methanol sorption in PBI suggests that a severe polymer structural evolution takes place during sorption, which is compatible with the competitive hydrogen bonding mechanism discussed in section 4.2.10.

#### *4.2.10 Evolution of the PBI spectrum during methanol sorption: competitive hydrogen bonding mechanism*

A closer look at the PBI spectrum as a function of methanol concentration highlights a number of features that deserve a deeper analysis. In particular, a doublet at 704 – 690 cm<sup>-1</sup> is found to change markedly and in a regular fashion with methanol content (cf. Fig. 25A). The high frequency component increases at the expenses of the peak at lower frequency, and the doublet displays an *isosbestic* point at 694 cm<sup>-1</sup>. This feature is characteristic of two molecular species absorbing at close frequencies that are transformed into each other by the incoming penetrant. More specifically, the species absorbing at 690 cm<sup>-1</sup> is transformed into the species absorbing at 704 cm<sup>-1</sup>.

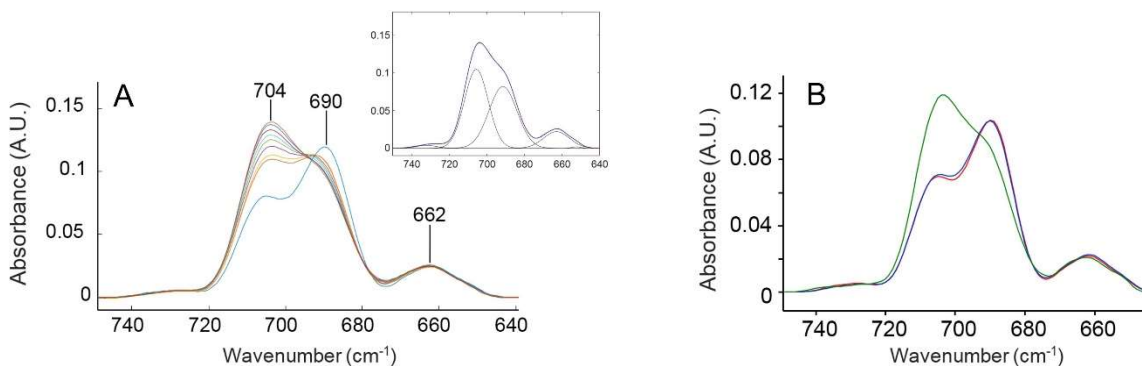
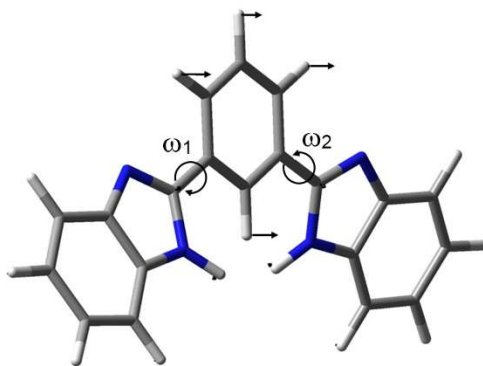


**Figure 25.** A) The PBI doublet at  $704 - 690 \text{ cm}^{-1}$  for the dry sample (blue trace) and the sample equilibrated at increasing methanol activity.  $p/p_0$  values, from the bottom trace up, are:  $= 0, 0.05, 0.1, 0.2, 0.3, 0.4, 0.5, 0.6$  and  $0.7$ . The inset represents the LSCF analysis of the spectral profile (blue trace = experimental, red trace = least-squares regression; black traces = resolved components). B) Reversibility experiment: Red trace = fully dried sample before the sorption/desorption run. Green trace = sample equilibrated at  $p/p_0 = 0-7$ . Blue trace = sample after complete desorption of penetrant.

The profile in the  $740 - 640 \text{ cm}^{-1}$  range has been subjected to a least-squares curve fitting (LSCF) analysis, whose results are shown in the inset of Fig. 25A. Simulation with Gaussian band shapes provided an excellent and consistent fit ( $R^2 > 0.999$  for the whole set of spectra), with the two main components exhibiting very close values of Full Width at Half-Height (FWHH) ( $15.1$  and  $15.7 \text{ cm}^{-1}$  for the  $704 \text{ cm}^{-1}$  and the  $690 \text{ cm}^{-1}$  peaks, respectively). The latter feature suggests that the two components originate from a single vibrational mode, whose position shifts because of a changing molecular environment. On the same premises, it can be supposed that the two peaks share similar values of molar absorptivity, which implies that the species absorbing at  $690 \text{ cm}^{-1}$  is strongly prevailing in the dry sample, but at  $p/p_0 = 0.05$  the two

concentrations are already comparable. At higher vapor pressures the  $704\text{ cm}^{-1}$  species starts to prevail, becoming clearly predominant from  $p/p_0 = 0.5$  onward. A further relevant observation is that the effect is fully reversible: on complete desorption of methanol from the sample equilibrated at the maximum  $p/p_0$  value (0.7), the doublet reverts to its original band shape (cf. Fig. 25B).

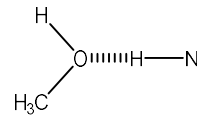
A previous *ab-initio* vibrational analysis of the PBI spectrum [68] indicated that, in the range  $775 - 630\text{ cm}^{-1}$ , are active the out-of-plane vibrations of the aromatic hydrogens [ $\omega(\text{CH})$ ], with those belonging to the benzimidazole (BI) moiety calculated at higher frequency than those of the m-substituted benzene (mB) (respectively, at  $730$  and  $685\text{ cm}^{-1}$ ). Considering a model that takes into account the molecular environment of the imidazole group (cf. Fig. S12, Supporting Information) it is found that, for two BI groups connected through a phenyl C–C bond (the connectivity realized in the PBI repeating unit), the intensity of the  $\omega(\text{CH})$  modes of the BI moiety is almost completely suppressed. It is therefore concluded that the observed doublet arises from the wagging modes of the mB unit (mode 11, according to Wilson notation [111], cf. Fig. 26). This vibration is found to be very sensitive to the dihedral angles between the mB ring and the condensed hetero-aromatic systems to which the benzene is linked ( $\omega_1$ ,  $\omega_2$  in Fig. 26) owing to the variable degree of conjugation between the involved aromatic systems. The establishment of a PBI self-interaction in a rigid H-bonding network, as schematically represented in Fig. 26, alters the  $\omega_1$  and  $\omega_2$  dihedrals, which are displaced from their equilibrium values in order to accommodate interactional and/or steric requirements. This distortion causes the  $\omega(\text{CH})$  mode to shift to lower frequency.



**Figure 26.** The mode at  $704 - 690 \text{ cm}^{-1}$  represented in terms of displacement vectors. The two dihedrals that induce the observed frequency shift are indicated.

When an N–H···N interaction is broken by a methanol molecule, the enhanced local mobility may allow a rearrangement of the  $\omega$  angle towards its equilibrium value. Therefore, we assign the  $690 \text{ cm}^{-1}$  component to self-associated PBI units located within an H-bonding chain (i.e. with both nitrogen atoms involved in the interaction as proton-donor and proton acceptor, respectively), and the component at  $704 \text{ cm}^{-1}$  to PBI units whereby one of the two H-bonds has been dissociated by a methanol molecule. A terminal BI unit with any of the two nitrogen atoms being dissociated, is expected to absorb at about the same frequency, which accounts for the presence of the  $704 \text{ cm}^{-1}$  component in the spectrum of the dry sample. In this frame, it is also possible to account for the complete reversibility of the effect (cf. Fig. 25B): due to the rigidity of the polymer matrix ( $T_g \approx 417^\circ\text{C}$ ), the head and the tail of the broken H-bonding chain remains in close proximity and, upon removal of the methanol molecule, the polymer self-interaction is readily re-established. Thus, the two-component profile discussed above is a distinct signature of H-bonding self-association in PBI and, contrary to the  $\nu(\text{NH/OH})$  range, provides a direct evidence of PBI dissociation by molecularly interacting probes. At the present

level of analysis, it is not clear if the probe acts as proton donor or acceptor or both, although

preliminary simulations suggest a preferential interaction of the  type.

A schematic representation of the proposed interaction mechanism, with the indication of the relevant peak frequencies, is reported in Fig. 27.

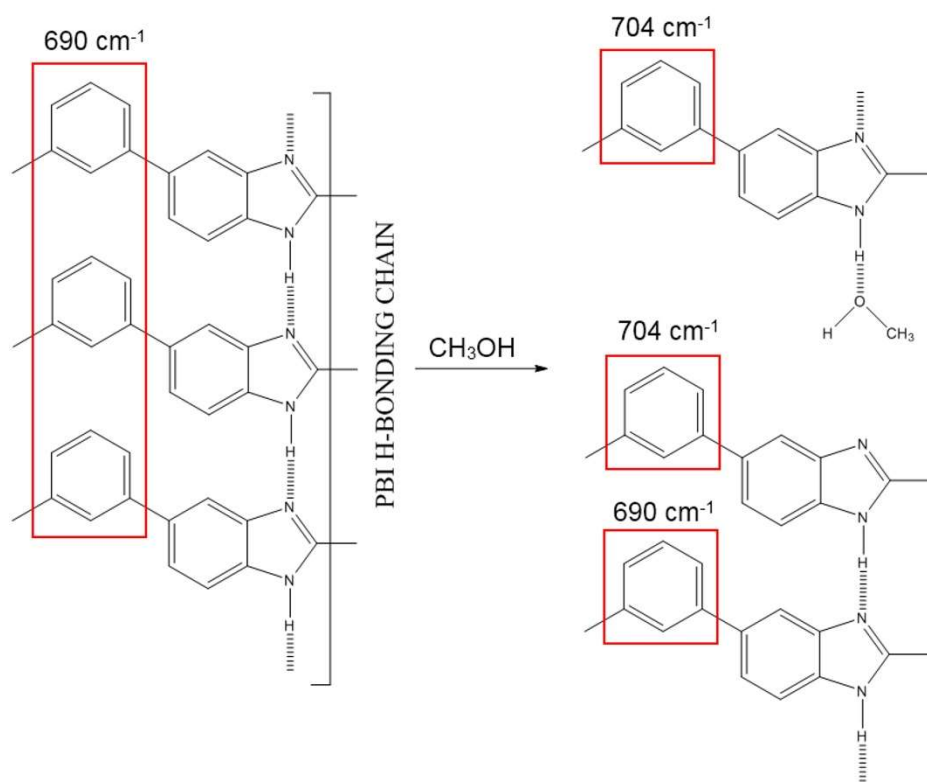


**Figure 27.** The proposed PBI/methanol interaction mechanism (that is, competitive hydrogen bonding).

Caution must be used in interpreting the conclusion drawn above. Indeed, the rapid re-establishment of the polymer hydrogen-bond network upon methanol desorption does not mean that the polymer instantaneously returns to its original structure. To shed light on this aspect, after reaching equilibrium at an activity of about 0.7, barometric sorption was measured by



decreasing the activity in the sorption cell. The sorption-desorption curve (cf. Fig S6, Supporting Information) exhibits some hysteresis, which indicates that, at least within the short experimental time frame, the polymer maintains a swollen structure upon methanol removal. The long term recovery of the initial transport properties is under investigation.

## Chapter 5: Conclusions and Recommendations

To design functional membrane materials for organic solvent separation it is imperative to understand fundamental aspects of small molecule transport. To fill this gap in the literature, which for three decades represented the main roadblock to progress in this area, in this dissertation, fundamental chemical-physical, kinetic and thermodynamic aspects governing solute and solvent transport in OSN-OSRO membranes have been elucidated. For the first time ever, a thermodynamic/diffusion framework has been developed to explain solvent flux nonlinearity in glassy polymers and dispelled the idea that compaction can be responsible for this phenomena.. Equally important, it has been shown that if the solution-diffusion model is properly formulated, it is sufficient to describe solute and solvent transport in OSN-OSRO dense (i.e., non-porous) polymer membranes, without the need to resort to complicate or semi-empirical transport models. This result helps settle a long standing debate in the literature about whether the solution diffusion model, the pore flow model, or some combination of the two should be used to describe small molecule transport through OSN-OSRO polymers.

A fundamental study of the role of intermolecular interactions and plasticization on transport properties of a wide variety of solvents has been examined for Celazole<sup>®</sup> PBI. For the first time ever, the molecular mechanism of polymers plasticization upon exposure to organic solvents has been provided, using transport measurements and FTIR spectroscopy. According to this approach, plasticization is explained by the “competitive hydrogen bonding” mechanism. According to this

This chapter is re-adapted from:

Bye et al., Pure and mixed fluid sorption and transport in celazole<sup>®</sup> polybenzimidazole: Effect of plasticization, JMS, 235-247, volume 580, 2019, with permission of Elsevier

Bye, Galizia, Fundamental origin of flux-nonlinearity in organic solvent nanofiltration: Formulation of a thermodynamic/diffusion framework, JMS, volume 603, 2020, with permission of Elsevier

Loianno et al., Plasticization mechanism in polybenzimidazole membranes for organic solvent nanofiltration: Molecular insights from in situ FTIR spectroscopy, Journal of Polymer Science, 2547-2560, volume 58, issue 18, 2020 with permission of Wiley Online Library

mechanism, sorbed methanol molecules reversibly disrupt the hydrogen bonded network characteristic of dry PBI, by forming mutual polymer/penetrant hydrogen bonds, which enhances polymer chain mobility and favors polymer swelling and plasticization. This physical picture is confirmed by methanol sorption experiments at multiple temperatures, and by the analysis of isosteric heat of methanol sorption in PBI..

Recommendations for future work include examining and predicting flux decline for different polymers/solvents than PTMSP to verify that the results of this study can be safely extended to other systems. Additionally, conducting sorption experiments of PTMSP and ethanol which simulate the downstream face of the membrane could verify the hypothesis of the thermodynamic-diffusion framework formulated in this dissertation. Finally, developing and testing polymer OSN-OSRO membranes exhibiting high selectivity would be a real breakthrough, as the problem of selectivity in organic separations is one of the top priorities in the field.

## Literature Cited

- [1] M. Galizia, K.P. Bye, Advances in organic solvent nanofiltration rely on physical chemistry and polymer chemistry, *Frontiers in chemistry*, 6 (2018) 511.
- [2] J. Chau, P. Basak, J. Kaur, Y. Hu, K.K. Sirkar, Performance of a composite membrane of a perfluorodioxole copolymer in organic solvent nanofiltration, *Sep. Pur. Tech.*, 199 (2018) 233-241.
- [3] M. Galizia, W.S. Chi, Z.P. Smith, T.C. Merkel, R.W. Baker, B.D. Freeman, 50th anniversary perspective: Polymers and mixed matrix membranes for gas and vapor separation: A review and prospective opportunities, *Macromolecules*, 50 (2017) 7809-7843.
- [4] D.S. Sholl, R.P. Lively, Seven chemical separations to change the world, *Nature News*, 532 (2016) 435.
- [5] U.S. Environmental Protection Agency (EPA), <https://www.epa.gov/>, 2017 (accessed May 30 2019).
- [6] Robeson, J. *Membr. Sci.* **2008**, 320, 390-400
- [7] Pinnau et al., *Adv. Mater.* **2020**, 32 2001132
- [8] M.F. Jimenez-Solomon, Q. Song, K.E. Jelfs, M. Munoz-Ibanez, A.G. Livingston, Polymer nanofilms with enhanced microporosity by interfacial polymerization, *Nature Materials*, 15 (2016) 760.
- [9] I.B. Valtcheva, S.C. Kumbharkar, J.F. Kim, Y. Bhole, A.G. Livingston, Beyond polyimide: crosslinked polybenzimidazole membranes for organic solvent nanofiltration (OSN) in harsh environments, *J. Membr. Sci.*, 457 (2014) 62-72.
- [10] J. da Silva Burgal, L.G. Peeva, S. Kumbharkar, A. Livingston, Organic solvent resistant poly(ether-ether-ketone) nanofiltration membranes, *J. Membr. Sci.*, 479 (2015) 105-116.

- [11] M.F.J. Solomon, Y. Bhole, A.G. Livingston, High flux membranes for organic solvent nanofiltration (OSN)—Interfacial polymerization with solvent activation, *J. Membr. Sci.*, 423 (2012) 371-382.
- [12] M. Cook, P.R. Gaffney, L.G. Peeva, A.G. Livingston, Roll-to-roll dip coating of three different PIMs for Organic Solvent Nanofiltration, *J. Membr. Sci.*, 558 (2018) 52-63.
- [13] P.H. Duong, K. Daumann, P.-Y. Hong, M. Ulbricht, S.P. Nunes, Interfacial polymerization of zwitterionic building blocks for high-flux nanofiltration membranes, *Langmuir*, 35 (2018) 1284-1293.
- [14] E. Florian, M. Modesti, M. Ulbricht, Preparation and characterization of novel solvent-resistant nanofiltration composite membranes based on crosslinked polyurethanes, *Ind. Eng. Chem. Res.*, 46 (2007) 4891-4899.
- [15] P. Silva, S. Han, A.G. Livingston, Solvent transport in organic solvent nanofiltration membranes, *J. Membr. Sci.*, 262 (2005) 49-59.
- [16] L. Hesse, J. Mićović, P. Schmidt, A. Górak, G. Sadowski, Modelling of organic-solvent flux through a polyimide membrane, *J. Membr. Sci.*, 428 (2013) 554-561.
- [17] B. Van der Bruggen, J. Schaep, D. Wilms, C. Vandecasteele, A comparison of models to describe the maximal retention of organic molecules in nanofiltration, *Sep. Sci. Tech.*, 35 (2000) 169-182.
- [18] A. Volkov, D. Stamatialis, V. Khotimsky, V. Volkov, M. Wessling, N. Plate, Poly [1-(trimethylsilyl)-1-propyne] as a solvent resistance nanofiltration membrane material, *J. Membr. Sci.*, 281 (2006) 351-357.

- [19] S. Darvishmanesh, A. Buekenhoudt, J. Degève, B. Van der Bruggen, Coupled series–parallel resistance model for transport of solvent through inorganic nanofiltration membranes, *Sep. Pur. Tech.*, 70 (2009) 46-52.
- [20] A.E. Yaroshchuk, Solution-diffusion-imperfection model revised, *J. Membr. Sci.*, 101 (1995) 83-87.
- [21] P. Marchetti, M.F. Jimenez Solomon, G. Szekely, A.G. Livingston, Molecular separation with organic solvent nanofiltration: a critical review, *Chem. Rev.*, 114 (2014) 10735-10806.
- [22] D.R. Machado, D. Hasson, R. Semiat, Effect of solvent properties on permeate flow through nanofiltration membranes. Part I: investigation of parameters affecting solvent flux, *J. Membr. Sci.*, 163 (1999) 93-102.
- [23] S. Postel, G. Spalding, M. Chirnside, M. Wessling, On negative retentions in organic solvent nanofiltration, *J. Membr. Sci.*, 447 (2013) 57-65.
- [24] S. Postel, S. Wessel, T. Keil, P. Eiselt, M. Wessling, Multicomponent mass transport in organic solvent nanofiltration with solvent mixtures, *J. Membr. Sci.*, 466 (2014) 361-369.
- [25] E. Gibbins, M. D'Antonio, D. Nair, L.S. White, L.M.F. dos Santos, I.F. Vankelecom, A.G. Livingston, Observations on solvent flux and solute rejection across solvent resistant nanofiltration membranes, *Desalination*, 147 (2002) 307-313.
- [26] M. Abdellah, L. Liu, C. Scholes, B. Freeman, S. Kentish, Organic solvent nanofiltration of binary vegetable oil/terpene mixtures: Experiments and modelling, *J. Membr. Sci.*, 573 (2019) 694-703.
- [27] M. Abdellah, C. Scholes, B. Freeman, L. Liu, S. Kentish, Transport of terpenes through composite PDMS/PAN solvent resistant nanofiltration membranes, *Sep. Pur. Tech.*, 207 (2018) 470-476.

- [28] S. Tsarkov, V. Khotimskiy, P.M. Budd, V. Volkov, J. Kukushkina, A. Volkov, Solvent nanofiltration through high permeability glassy polymers: effect of polymer and solute nature, *J. Membr. Sci.*, 423 (2012) 65-72.
- [29] M.L. Jue, C.S. McKay, B.A. McCool, M. Finn, R.P. Lively, Effect of Nonsolvent Treatments on the Microstructure of PIM-1, *Macromolecules*, 48 (2015) 5780-5790.
- [30] W. Ogieglo, K. Rahimi, S.B. Rauer, B. Ghanem, X. Ma, I. Pinnau, M. Wessling, How Do Organic Vapors Swell Ultrathin Films of Polymer of Intrinsic Microporosity PIM-1?, *The Journal of Physical Chemistry B*, 121 (2017) 7210-7220.
- [31] G. Cocchi, M.G. De Angelis, F. Doghieri, Solubility and diffusivity of liquids for food and pharmaceutical applications in crosslinked polydimethylsiloxane (PDMS) films: I. Experimental data on pure organic components and vegetable oil, *Journal of Membrane Science*, 492 (2015) 600-611.
- [32] S. Postel, C. Schneider, M. Wessling, Solvent dependent solute solubility governs retention in silicone based organic solvent nanofiltration, *Journal of Membrane Science*, 497 (2016) 47-54.
- [33] S. Postel, S. Wessel, T. Keil, P. Eiselt, M. Wessling, Multicomponent mass transport in organic solvent nanofiltration with solvent mixtures, *Journal of Membrane Science*, 466 (2014) 361-369.
- [34] I.F. Vankelecom, S. De Beukelaer, J.B. Uytterhoeven, Sorption and pervaporation of aroma compounds using zeolite-filled PDMS membranes, *The Journal of Physical Chemistry*, 101 (1997) 5186-5190.
- [35] J.P. Stanford, A.L. Maier, L.A. McDonald, P.H. Pfromm, M.E. Rezac, Kinetic and equilibrium sorption of organic liquids and vapors in Matrimid, *Journal of Membrane Science*, 512 (2016) 29-37.

- [36] E.J. Kappert, M.J. Raaijmakers, K. Tempelman, F.P. Cuperus, W. Ogieglo, N.E. Benes, Swelling of 9 polymers commonly employed for solvent-resistant nanofiltration membranes: A comprehensive dataset, *Journal of membrane science*, 569 (2019) 177-199.
- [37] T. Merkel, V. Bondar, K. Nagai, B.D. Freeman, Y.P. Yampolskii, *Macromolecules* **1999**, 32, 8427.
- [38] M. Galizia, D.R. Paul, B.D. Freeman, *Polymer* **2016**, 102, 281.
- [39] D.R. Paul, Reformulation of the solution-diffusion theory of reverse osmosis, *J. Membr. Sci.*, 241 (2004) 371-386.
- [40] W. Koros, D.R. Paul, G. Huvar, *Polymer* **1979**, 20, 956.
- [41] D.R. Paul, W. Koros, *J. Polym. Sci.: Polym. Phys. Ed.* **1976**, 14, 675.
- [42] B.H. Zimm, J.L. Lundberg, Sorption of vapors by high polymers, *The Journal of Physical Chemistry*, 60 (1956) 425-428.
- [43] S.K. Burgess, D.S. Mikkilineni, B.Y. Daniel, D.J. Kim, C.R. Mubarak, R.M. Kriegel, W.J. Koros, Water sorption in poly (ethylene furanoate) compared to poly (ethylene terephthalate). Part 1: Equilibrium sorption, *Polymer*, 55 (2014) 6861-6869.
- [44] A. Berens, H. Hopfenberg, Diffusion and relaxation in glassy polymer powders: 2. Separation of diffusion and relaxation parameters, *Polymer*, 19 (1978) 489-496.
- [45] M. Galizia, M.G. De Angelis, E. Finkelshtein, Y.P. Yampolskii, G.C. Sarti, Sorption and transport of hydrocarbons and alcohols in addition-type poly (trimethyl silyl norbornene). I: Experimental data, *Journal of membrane science*, 385 (2011) 141-153.
- [46] J.S. Lee, R.T. Adams, W. Madden, W.J. Koros, Toluene and n-heptane sorption in Matrimid<sup>®</sup> asymmetric hollow fiber membranes, *Polymer*, 50 (2009) 6049-6056.
- [47] J. Crank, *The mathematics of diffusion*, Oxford university press, 1979.



- [48] R.B. Bird, W.E. Stewart, E.N. Lightfoot, Transport phenomena, John Wiley & Sons, 2007.
- [49] A. Singh, B.D. Freeman, I. Pinnau, Pure and mixed gas acetone/nitrogen permeation properties of polydimethylsiloxane [PDMS], *J. Polym. Sci. B: Polym. Phys.*, 36 (1998) 289-301.
- [50] F. Doghieri, G. Sarti, Solubility, diffusivity, and mobility of n-pentane and ethanol in poly (1-trimethylsilyl-1-propyne), *Journal of Polymer Science Part B: Polymer Physics*, 35 (1997) 2245-2258.
- [51] T. Merkel, V. Bondar, K. Nagai, B. Freeman, Sorption and transport of hydrocarbon and perfluorocarbon gases in poly (1-trimethylsilyl-1-propyne), *Journal of Polymer Science Part B: Polymer Physics*, 38 (2000) 273-296.
- [52] M. Galizia, P. La Manna, M. Pannico, G. Mensitieri, P. Musto, *Polymer* **2014**, 55, 1028.
- [53] P.J. Flory, Principles of polymer chemistry, Cornell University Press, 1953.
- [54] I.C. Sanchez, R.H. Lacombe, An elementary molecular theory of classical fluids. Pure fluids, *J. Phys. Chem.*, 80 (1976) 2352-2362.
- [55] R.H. Lacombe, I.C. Sanchez, Statistical thermodynamics of fluid mixtures, *J. Phys. Chem.*, 80 (1976) 2568-2580.
- [56] F. Doghieri, G.C. Sarti, Nonequilibrium lattice fluids: a predictive model for the solubility in glassy polymers, *Macromolecules*, 29 (1996) 7885-7896.
- [57] M. Galizia, K.A. Stevens, Z.P. Smith, D.R. Paul, B.D. Freeman, Nonequilibrium lattice fluid modeling of gas solubility in HAB-6FDA polyimide and its thermally rearranged analogues, *Macromolecules*, 49 (2016) 8768-8779.
- [58] R. Hariharan, B.D. Freeman, R. Carbonell, G. Sarti, Equation of state predictions of sorption isotherms in polymeric materials, *J. Appl. Polym. Sci.*, 50 (1993) 1781-1795.

- [59] M. Galizia, Z.P. Smith, G.C. Sarti, B.D. Freeman, D.R. Paul, Predictive calculation of hydrogen and helium solubility in glassy and rubbery polymers, *J. Membr. Sci.*, 475 (2015) 110-121.
- [60] H. Lin, B.D. Freeman, Gas and vapor solubility in cross-linked poly (ethylene glycol diacrylate), *Macromolecules*, 38 (2005) 8394-8407.
- [61] G.M. Shi, H. Chen, Y. Jean, T.S. Chung, Sorption, swelling, and free volume of polybenzimidazole (PBI) and PBI/zeolitic imidazolate framework (ZIF-8) nano-composite membranes for pervaporation, *Polymer*, 54 (2013) 774-783.
- [62] J.D. Moon, M. Galizia, H. Borjigin, R. Liu, J.S. Riffle, B.D. Freeman, D.R. Paul, Water Vapor Sorption, Diffusion, and Dilation in Polybenzimidazoles, *Macromolecules*, 51 (2018) 7197-7208.
- [63] A.F. Barton, *CRC handbook of solubility parameters and other cohesion parameters*, Routledge, 2017.
- [64] I. Smallwood, *Handbook of organic solvent properties*, Butterworth-Heinemann, 2012.
- [65] J.L. Gómez, G.A. Rodríguez, D.M. Cristancho, D.R. Delgado, C.P. Mora, A. Yurquina, F. Martínez, Extended Hildebrand solubility approach applied to nimodipine in PEG 400+ ethanol mixtures, *Revista Colombiana de Ciencias Químico-Farmacéuticas*, 42 (2013) 103-121.
- [66] A. Jouyban, *Handbook of solubility data for pharmaceuticals*, CRC Press, 2009.
- [67] T. Matsuura, *Synthetic membranes and membrane separation processes*, CRC press, 1993.
- [68] P. Musto, P. La Manna, J.D. Moon, M. Galizia, B.D. Freeman, *ACS Omega* **2018**, 3, 11592.
- [69] M. De Angelis, G. Sarti, F. Doghieri, NELF model prediction of the infinite dilution gas solubility in glassy polymers, *J. Membr. Sci.*, 289 (2007) 106-122.

- [70] V. Loiano, Q. Zhang, S. Luo, R. Guo, M. Galizia, Modeling Gas and Vapor Sorption and Swelling in Triptycene-Based Polybenzoxazole: Evidence for Entropy-Driven Sorption Behavior, *Macromolecules*, (2019).
- [71] G. Scherillo, L. Sanguigno, M. Galizia, M. Lavorgna, P. Musto, G. Mensitieri, Non-equilibrium compressible lattice theories accounting for hydrogen bonding interactions: Modelling water sorption thermodynamics in fluorinated polyimides, *Fl. Phase Eq.*, 334 (2012) 166-188.
- [72] G. Scherillo, L. Sanguigno, L. Sansone, E. Di Maio, M. Galizia, G. Mensitieri, Thermodynamics of water sorption in poly ( $\epsilon$ -caprolactone): A comparative analysis of lattice fluid models including hydrogen bond contributions, *Fl. Phase Eq.*, 313 (2012) 127-139.
- [73] G.C. Sarti, M.G. De Angelis, Calculation of the solubility of liquid solutes in glassy polymers, *AIChE Journal*, 58 (2012) 292-301.
- [74] T.C. Merkel, Z. He, I. Pinnau, B.D. Freeman, P. Meakin, A.J. Hill, Effect of nanoparticles on gas sorption and transport in poly (1-trimethylsilyl-1-propyne), *Macromolecules*, 36 (2003) 6844-6855.
- [75] P.R. Bevington, D.K. Robinson, J.M. Blair, A.J. Mallinckrodt, S. McKay, Data reduction and error analysis for the physical sciences, *Computers in Physics*, 7 (1993) 415-416.
- [76] G. Huvard, V. Stannett, W. Koros, H. Hopfenberg, The pressure dependence of CO<sub>2</sub> sorption and permeation in poly (acrylonitrile), *J. Membr. Sci.*, 6 (1980) 185-201.
- [77] W.J. Koros, A. Chan, D.R. Paul, Sorption and transport of various gases in polycarbonate, *J. Membr. Sci.*, 2 (1977) 165-190.
- [78] C.P. Ribeiro, B.D. Freeman, D.S. Kalika, S. Kalakkunnath, Aromatic polyimide and polybenzoxazole membranes for the fractionation of aromatic/aliphatic hydrocarbons by pervaporation, *J. Membr. Sci.*, 390 (2012) 182-193.

- [79] M. Galizia, M.G. De Angelis, G.C. Sarti, Sorption of hydrocarbons and alcohols in addition-type poly (trimethyl silyl norbornene) and other high free volume glassy polymers. II: NELF model predictions, *Journal of membrane science*, 405 (2012) 201-211.
- [80] G. Fleming, W. Koros, Dilation of polymers by sorption of carbon dioxide at elevated pressures. 1. Silicone rubber and unconditioned polycarbonate, *Macromolecules*, 19 (1986) 2285-2291.
- [81] J.D. Wind, S.M. Sirard, D.R. Paul, P.F. Green, K.P. Johnston, W.J. Koros, Carbon dioxide-induced plasticization of polyimide membranes: pseudo-equilibrium relationships of diffusion, sorption, and swelling, *Macromolecules*, 36 (2003) 6433-6441.
- [82] J.D. Wind, S.M. Sirard, D.R. Paul, P.F. Green, K.P. Johnston, W.J. Koros, Relaxation dynamics of CO<sub>2</sub> diffusion, sorption, and polymer swelling for plasticized polyimide membranes, *Macromolecules*, 36 (2003) 6442-6448.
- [83] A. Bos, I. Pünt, M. Wessling, H. Strathmann, CO<sub>2</sub>-induced plasticization phenomena in glassy polymers, *Journal of Membrane Science*, 155 (1999) 67-78.
- [84] A.F. Ismail, W. Lorna, Penetrant-induced plasticization phenomenon in glassy polymers for gas separation membrane, *Separation and purification technology*, 27 (2002) 173-194.
- [85] E.S. Sanders, Penetrant-induced plasticization and gas permeation in glassy polymers, *Journal of Membrane Science*, 37 (1988) 63-80.
- [86] J. Liu, Q. Xu, J. Jiang, Swelling and organic solvent nanofiltration of polymer membranes: Microscopic insights from molecular simulations, *Journal of Membrane Science*, (2018).
- [87] G. Cocchi, M.G. De Angelis, F. Doghieri, Solubility and diffusivity of liquids for food and pharmaceutical applications in crosslinked polydimethylsiloxane (PDMS) films: II. Experimental data on mixtures, *Journal of Membrane Science*, 492 (2015) 612-619.

- [88] J.C. Jansen, K. Friess, E. Drioli, Organic vapour transport in glassy perfluoropolymer membranes: A simple semi-quantitative approach to analyze clustering phenomena by time lag measurements, *Journal of membrane science*, 367 (2011) 141-151.
- [89] A. Tokarev, K. Friess, J. Machkova, M. Šipek, Y. Yampolskii, Sorption and diffusion of organic vapors in amorphous Teflon AF2400, *Journal of Polymer Science Part B: Polymer Physics*, 44 (2006) 832-844.
- [90] H. Borjigin, K.A. Stevens, R. Liu, J.D. Moon, A.T. Shaver, S. Swinnea, B.D. Freeman, J. Riffle, J.E. McGrath, Synthesis and characterization of polybenzimidazoles derived from tetraaminodiphenylsulfone for high temperature gas separation membranes, *Polymer*, 71 (2015) 135-142.
- [91] H. Vogel, C. Marvel, Polybenzimidazoles, new thermally stable polymers, *Journal of Polymer Science*, 50 (1961) 511-539.
- [92] J. Chiou, J.W. Barlow, D. Paul, Plasticization of glassy polymers by CO<sub>2</sub>, *Journal of Applied Polymer Science*, 30 (1985) 2633-2642.
- [93] M. Ferrari, M. Galizia, M. De Angelis, G. Sarti, Gas and vapor transport in mixed matrix membranes based on amorphous Teflon AF1600 and AF2400 and fumed silica, *Industrial & Engineering Chemistry Research*, 49 (2010) 11920-11935.
- [94] P. Chandra, W.J. Koros, Sorption and transport of methanol in poly (ethylene terephthalate), *Polymer*, 50 (2009) 236-244.
- [95] P. Li, T. Chung, D. Paul, Gas sorption and permeation in PIM-1, *Journal of membrane science*, 432 (2013) 50-57.

- [96] P. Li, T. Chung, D. Paul, Temperature dependence of gas sorption and permeation in PIM-1, *Journal of Membrane Science*, 450 (2014) 380-388.
- [97] K. Schult, D. Paul, Water sorption and transport in a series of polysulfones, *Journal of Polymer Science Part B: Polymer Physics*, 34 (1996) 2805-2817.
- [98] E.M. Davis, Y.A. Elabd, Water clustering in glassy polymers, *The Journal of Physical Chemistry B*, 117 (2013) 10629-10640.
- [99] M. Galizia, K.A. Stevens, D.R. Paul, B.D. Freeman, Modeling gas permeability and diffusivity in HAB-6FDA polyimide and its thermally rearranged analogs, *Journal of Membrane Science*, 537 (2017) 83-92.
- [100] J.S. Lee, W. Madden, W.J. Koros, Antiplasticization and plasticization of Matrimid® asymmetric hollow fiber membranes—Part A. Experimental, *Journal of Membrane Science*, 350 (2010) 232-241.
- [101] Y. Maeda, D. Paul, Effect of antiplasticization on gas sorption and transport. I. Polysulfone, *Journal of Polymer Science Part B: Polymer Physics*, 25 (1987) 957-980.
- [102] R. Hodge, T. Bastow, G. Edward, G. Simon, A. Hill, Free volume and the mechanism of plasticization in water-swollen poly (vinyl alcohol), *Macromolecules*, 29 (1996) 8137-8143.
- [103] P. Musto, F. Karasz, W. MacKnight, Hydrogen bonding in polybenzimidazole/polyimide systems: a Fourier-transform infra-red investigation using low-molecular-weight monofunctional probes, *Polymer*, 30 (1989) 1012-1021.
- [104] D. Tomlin, A. Fratini, M. Hunsaker, W.W. Adams, The role of hydrogen bonding in rigid-rod polymers: the crystal structure of a polybenzobisimidazole model compound, *Polymer*, 41 (2000) 9003-9010.

- [105] D.W. Van Krevelen, K. Te Nijenhuis, Properties of polymers: their correlation with chemical structure; their numerical estimation and prediction from additive group contributions, Elsevier, 2009.
- [106] J.M. Zielinski, J. Duda, Predicting polymer/solvent diffusion coefficients using free-volume theory, *AIChE Journal*, 38 (1992) 405-415.
- [107] M. Baiardo, G. Frisoni, M. Scandola, M. Rimelen, D. Lips, K. Ruffieux, E. Wintermantel, Thermal and mechanical properties of plasticized poly (L-lactic acid), *Journal of Applied Polymer Science*, 90 (2003) 1731-1738.
- [108] K.A. Stevens, Z.P. Smith, K.L. Gleason, M. Galizia, D.R. Paul, B.D. Freeman, *J. Membr. Sci.* **2017**, 533, 75.
- [109] M.S. Caceci, *Anal. Chem.* **1989**, 61, 2324.
- [110] M. Sanopoulou, P.P. Roussis, J.H. Petropoulos, *J. Polym. Sci. B: Polym. Phys.* **1995**, 33, 993.
- [111] E.B. Wilson Jr, *Phys. Rev.* **1934**, 45, 706.
- [112] Q. Liu, M. Galizia, K.L. Gleason, C.A. Scholes, D.R. Paul, B.D. Freeman, Influence of toluene on CO<sub>2</sub> and CH<sub>4</sub> gas transport properties in thermally rearranged (TR) polymers based on 3, 3'-dihydroxy-4, 4'-diamino-biphenyl (HAB) and 2, 2'-bis-(3, 4-dicarboxyphenyl) hexafluoropropane dianhydride (6FDA), *Journal of Membrane Science*, 514 (2016) 282-293.
- [113] J.D. Moon, M. Galizia, H. Borjigin, R. Liu, J.S. Riffle, B.D. Freeman, D.R. Paul, *Polymer* **2020**, 122170.
- [114] P. Musto, M. Galizia, P. La Manna, M. Pannico, G. Mensitieri, *Frontiers in chemistry* **2014**, 2, 1.
- [115] F.A. Long, D. Richman, *J. Am. Chem. Soc.* **1960**, 82, 513.

[116] G. Camera-Roda, G.C. Sarti, *Aiche J.* **1990**, 36, 851.



## APPENDICES

### Supporting information

#### Uncertainty on liquid methanol sorption measurement.

In this study, the blotting and weight method has been used to measure the solubility of organic liquids in Celazole<sup>®</sup>. However, when considering highly volatile liquids, such as methanol, the blotting and weight process must be very fast to prevent evaporative solvent loss. In Fig. S1, the weight of a thick (210  $\mu\text{m}$ ) and thin (32  $\mu\text{m}$ ) Celazole<sup>®</sup> sample after swelling in liquid methanol at 25°C is reported as a function of time. After blotting with a paper towel for 15 seconds, samples were left on the balance plate for 5 minutes and the balance reading was recorder every minute. As shown, at the end of the experiment, 5% and 9% of absorbed methanol evaporated from thick and thin films, respectively.

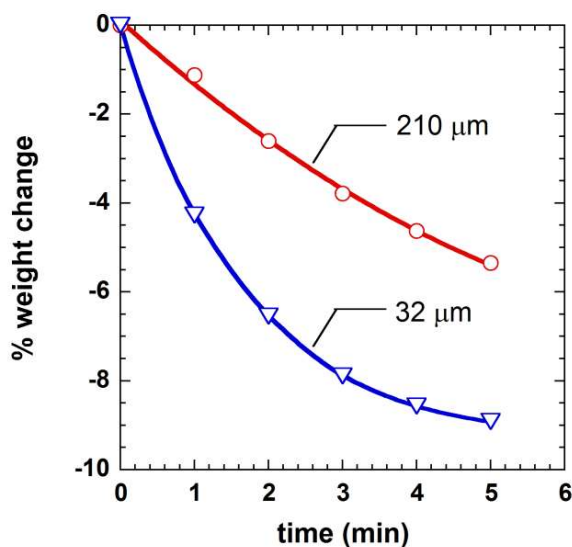


**Figure S1.** Weight of a thick (210  $\mu\text{m}$ ) and thin (32  $\mu\text{m}$ ) Celazole<sup>®</sup> sample after equilibration in liquid methanol as a function of time. Continuous lines are a guide for the eye.

The blotting and weight steps do not take more than 20 seconds and, in this timeframe, methanol evaporation is negligible if thick membrane specimens are used. This very slow evaporation rate provides further evidence that methanol strongly interacts with the polymer backbone, likely by forming hydrogen bonds. The methanol evaporative methanol loss can be estimated as a function of time using a simple Fickian model:

$$\%loss = 100 \times \frac{4}{\ell} \sqrt{\frac{\bar{D}t}{\pi}} \quad (\text{Eq. S1})$$

where  $\bar{D}$  is the average diffusion coefficient of liquid methanol in Celazole<sup>®</sup>, which was estimated to be about  $6 \times 10^{-6} \text{ cm}^2/\text{s}$ , and  $\ell$  is the film thickness (i.e., 210  $\mu\text{m}$ ). Based on this model, once the sample has been removed from the jar, all methanol should evaporate in less than 1 minute (i.e., after 1 min the sample should be methanol-free), which is not consistent with the experimental data presented above. This discrepancy indicates that methanol molecules are strongly bounded to the polymer backbone, and this interaction is likely the cause of the slow methanol evaporation from the sample.

### **Experimental proof of dilation isotropicity.**

Celazole<sup>®</sup> dilations in the two co-planar directions, x and y, match very well to each other (cf. Fig. S2), which is sufficient to conclude that, as expected for an amorphous, unoriented polymer, dilation is isotropic. Therefore, in the manuscript, the experimental dilation is expressed as the average of the dilations in the x and y directions.

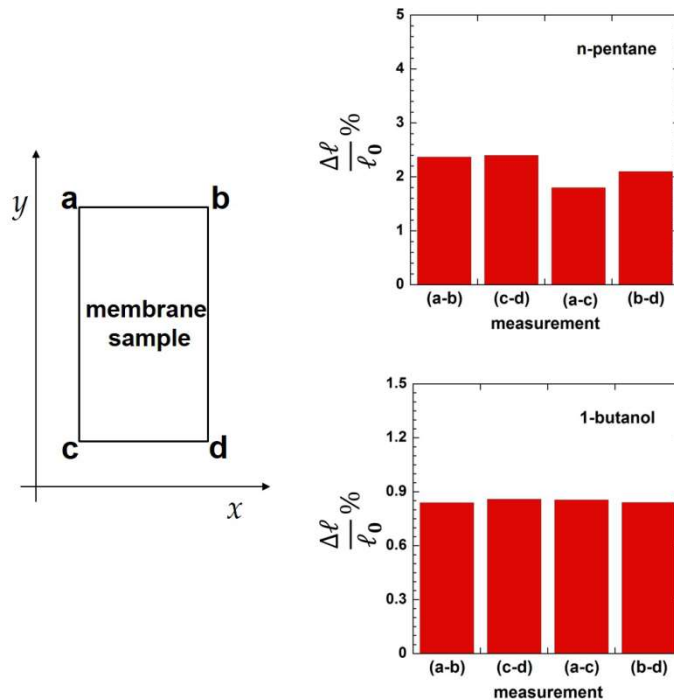


**Figure S2.** Celazole<sup>®</sup> dilation at 25°C in liquid *n*-pentane and 1-butanol measured in the coplanar *x* and *y* directions.

### Vapor sorption and diffusion measurement.

Methanol vapor sorption was measured using a constant volume, variable pressure (pressure decay) system. The system was kept at 25, 35, and 45 ± 0.1°C using a thermostatic water bath. Pressure was monitored with a MKS Baratron manometer (model 626C52TBE), whose full scale was 500 Torr. Penetrant activity was measured as the ratio between the final equilibrium pressure and the vapor pressure at the experimental temperature.

Before measuring vapor sorption, vacuum was pulled throughout the system for 24 hours, to ensure that all air gases were removed. As reported by Moon [1] and Musto [2], a residual amount of water, tenaciously bound to the polymer matrix, cannot be removed using this drying protocol. Complete polymer drying would require exposure to 200°C prior the sorption experiment. This

protocol, however, is out of experimental reach. So, vapor sorption experiments were run after drying the sample at the experimental temperature, as described previously by Moon et al. [1]. Sorption and diffusion experiments were performed stepwise. Vapor sorption was measured based on equilibrium pressure data, and diffusion coefficients were evaluated from the analysis of sorption kinetics using the Berens-Hopfenberg model (cf. Eq. 5) [3]. Due to the extremely low pressures, the ideal gas equation of state was used to convert pressures to mole numbers. Methanol was chosen as a model penetrant for vapor sorption experiments due to the relatively fast sorption kinetics and to facilitate the study of methanol induced plasticization. Sorption experiments with other organic vapors would be extremely time consuming due to the slow polymer relaxation.

### **Mechanical properties measurements**

Mechanical properties were measured using a Universal Testing Machine (model SSTM-2K, United Testing Systems, Fullerton, CA). Samples, prepared according to the ASTM D-1708-13 standard, were first soaked in liquid water and methanol at 25°C until reaching sorption equilibrium. Following this step, they were cut into a dog-bone shape and soaked again in the appropriate solvent for 24 h to minimize the effect of evaporation. Dry samples, to be used as baseline, were tested as well. All samples were about 200  $\mu\text{m}$  thick. After mounting the specimen into the grip, the mechanical test was run at a crosshead speed of 0.254 mm/min. Young's modulus was calculated from the initial slope of the stress-strain experimental curve [4, 5]. The final results were the average of at least 5 repeated measurements.

### **Methanol sorption and diffusion in Celazole<sup>®</sup> and PIM-1 at 25°C**

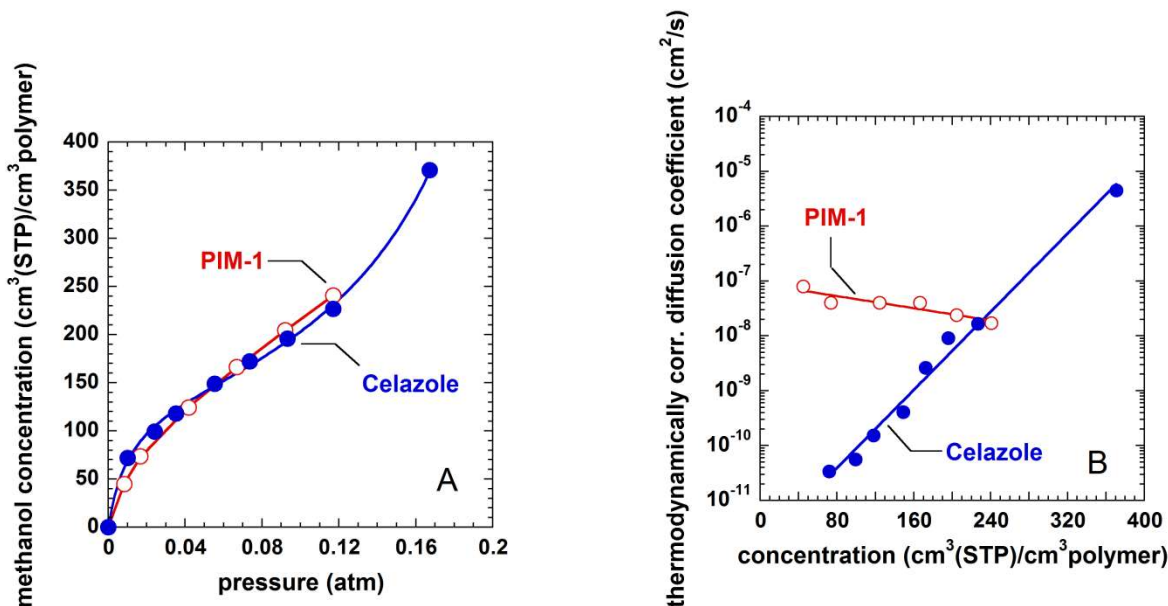
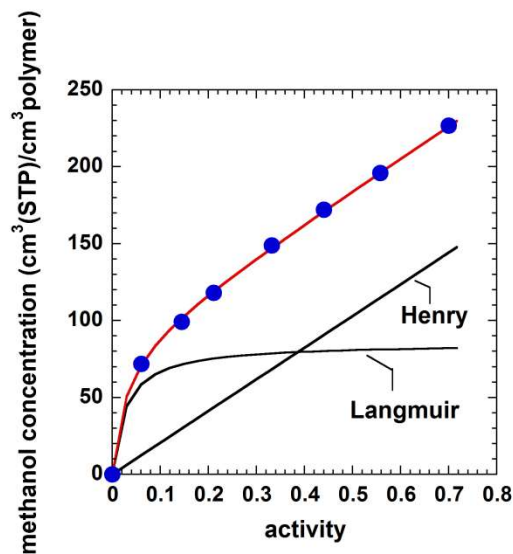


**Figure S3.** A) Methanol concentration in Celazole<sup>®</sup> and PIM-1 at 25°C as a function of pressure. B) Thermodynamically corrected methanol diffusion coefficient (i.e., mobility) in Celazole<sup>®</sup> and PIM-1 at 25°C as a function of concentration. Data for PIM-1 are from ref. [6].

As discussed in the manuscript, methanol sorption in PIM-1 and Celazole<sup>®</sup> at 25°C are comparable (cf. Fig. S3A).

At low-medium concentrations, methanol diffusion coefficient in PIM-1 exceeds that in Celazole<sup>®</sup> by three orders of magnitude (cf. Fig. S3B). This result is consistent with the larger fractional free volume exhibited by PIM-1 (i.e., 29%) relative to Celazole<sup>®</sup> (i.e., 12%). However, at medium-high concentrations, the penetrant accessible free volume of Celazole<sup>®</sup> increases substantially. Consistently, methanol diffusion coefficient in Celazole<sup>®</sup> increases and surpasses that in PIM-1. Methanol sorption does not plasticize PIM-1, whose FFV over the activity range 0-1 stays constant to about 29% or slightly decreases, due to blocking effect.

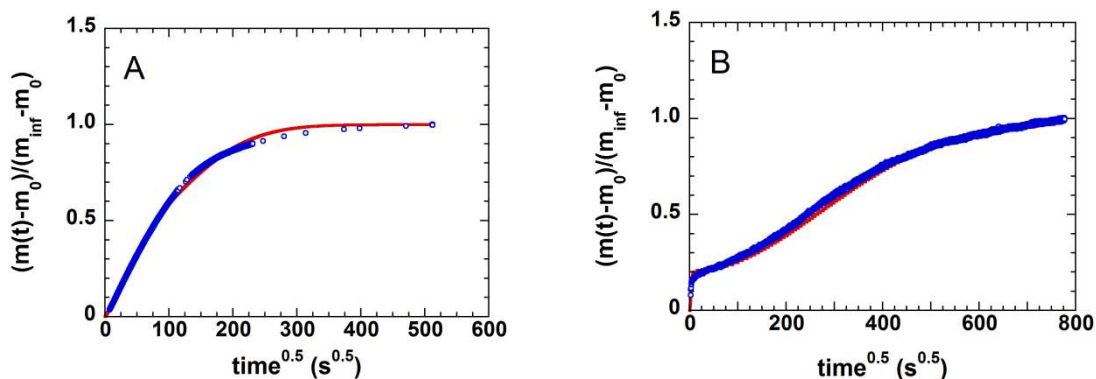
### Dual Mode analysis of methanol sorption in Celazole<sup>®</sup>

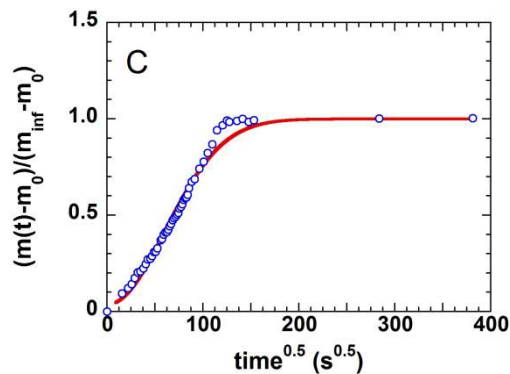


**Figure S4.** Dual mode fitting of methanol sorption data in Celazole<sup>®</sup> at 25°C. Henry's and Langmuir's sorption modes are represented along with the overall dual mode fitting.

In this study, Celazole<sup>®</sup> Langmuir's sites were considered saturated when the concentration in the Langmuir's mode didn't change by more than 0.5% between two subsequent sorption measurements. Based on this analysis, (cf. Fig. S4) saturation of Celazole<sup>®</sup> Langmuir's sites during methanol sorption occurs at an activity of about 0.22.

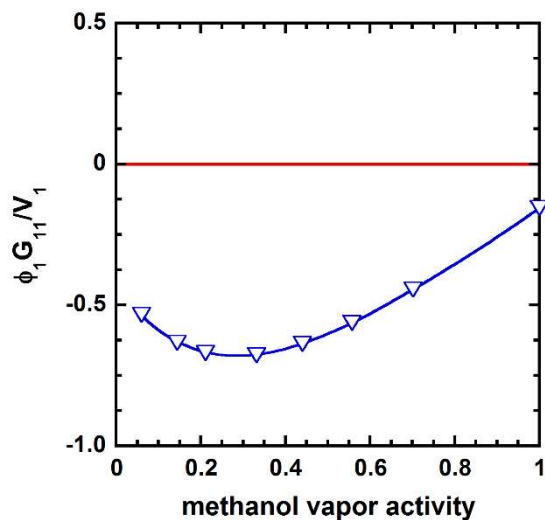
### Methanol sorption kinetics at 25°C





**Figure S5.** Methanol sorption kinetics in Celazole<sup>®</sup> at 25°C. Blue circles represent experimental data. Continuous red line represents the best fitting to the Berens-Hopfenberg model [3]. A Matlab<sup>®</sup> routine developed in house was used to model sorption kinetics. A) Differential activity jump 0-0.06. B) Differential activity jump 0.55-0.70. C) Activity jump 0-1 (i.e., liquid sorption kinetics).

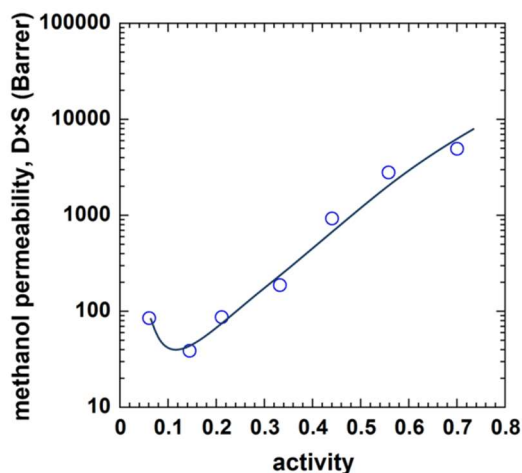
**Zimm-Lundberg analysis of methanol clustering.**



**Figure S6.** Methanol clustering integral in the activity range 0-1 [7]. Since the integral is always less than zero, methanol clustering in Celazole<sup>®</sup> can be considered negligible. Validation of this conclusion, however, would require a dedicated FTIR investigation which is underway.

### Methanol vapor permeability in Celazole<sup>®</sup>

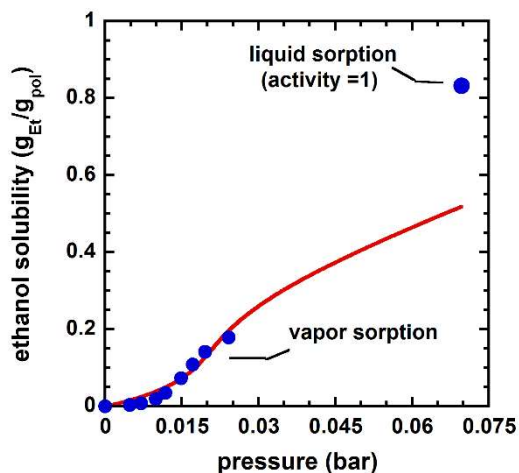
Methanol permeability in Celazole<sup>®</sup> at 25°C was calculated as the product of sorption and diffusion coefficients as a function of methanol activity in the external vapor phase (cf. Fig. S7). The initial decrease in methanol permeability is followed, at activity higher than 0.15, by a prominent increase, which is indicative of polymer plasticization.



**Figure S7.** Methanol permeability in Celazole<sup>®</sup> at 25°C, calculated using the solution-diffusion model, as a function of methanol activity. The continuous line is a guide for the eye.

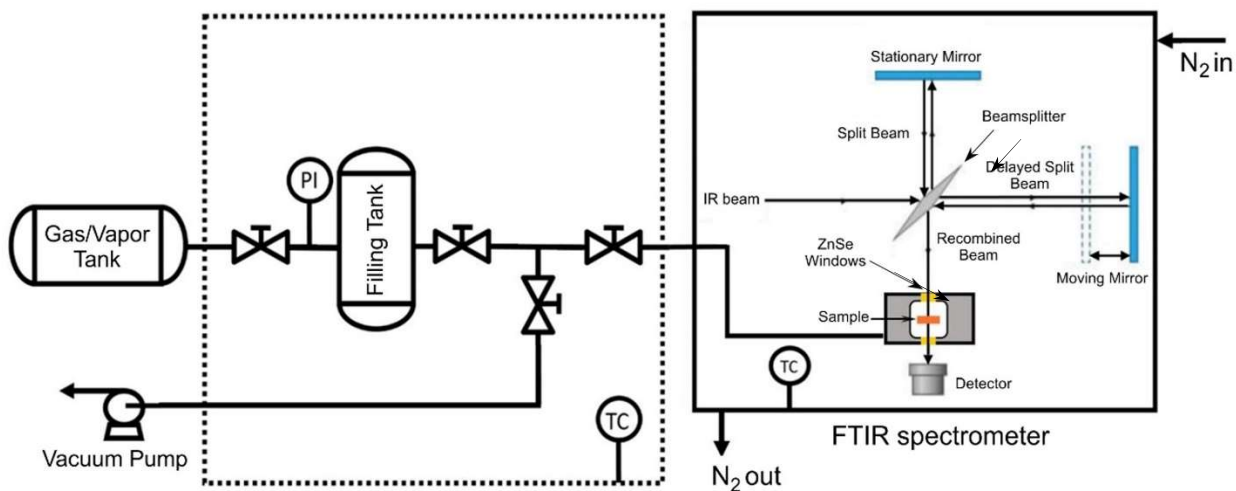
### Ethanol sorption in PTMSP



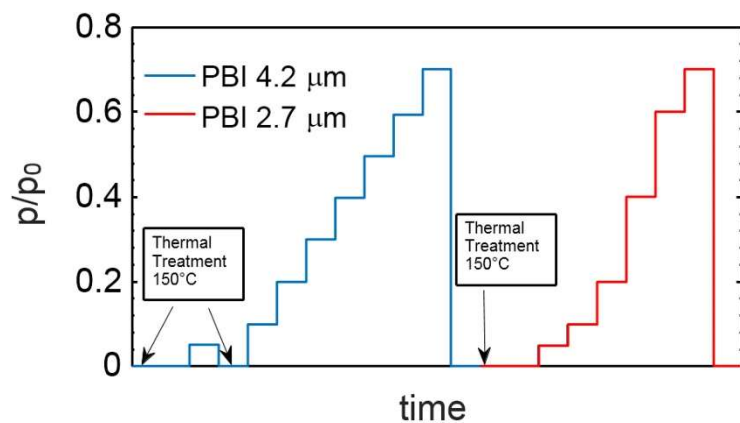


**Figure S8.** Ethanol sorption at room temperature in PTMSP in the activity range 0-1. Continuous line represents the NELF model fitting using the swelling coefficient,  $k_{sw}$ , retrieved from dilation data. The NELF model inability to account for ethanol clustering at high activity justifies the severe departure of the model calculation from experimental data at activity 1.

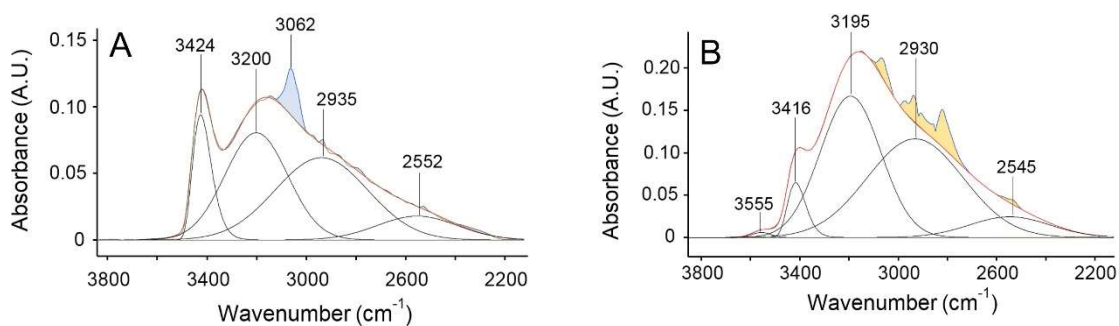
### FTIR Apparatus



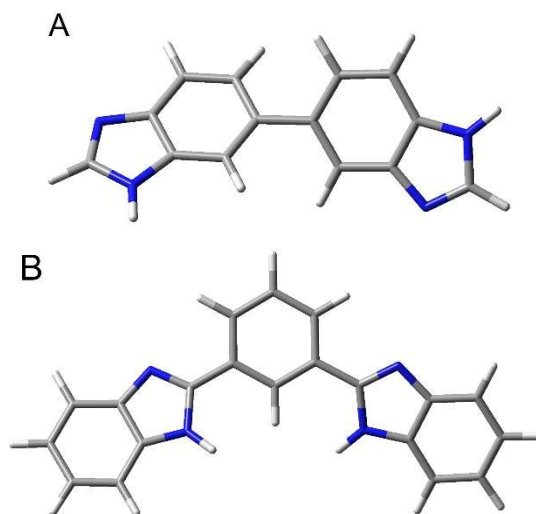
**Figure S9.** Experimental apparatus for time-resolved FTIR measurement of methanol sorption/desorption in PBI.



**Figure S10.** Isothermal sorption/desorption protocol at 25°C.



**Figure S11.** Curve fit analysis of the 3800 – 2180  $\text{cm}^{-1}$  range. A) dry PBI film. B) PBI film equilibrated at  $p/p_0 = 0.1$ .



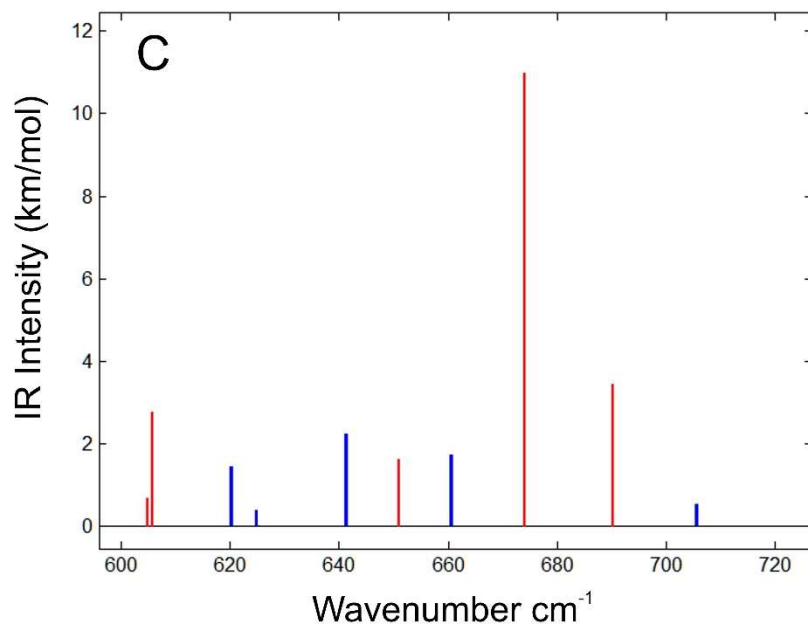


**Figure S12.** A) Model 1: 5,5'-Bi-1H-benzimidazole. B) Model 2: 2,2'-(1,3-Phenylene)bis(1H-benzimidazole). C) Calculated Infrared spectrum in the frequency range 600 – 720 cm<sup>-1</sup>. Model Chemistry: B3LYP/6-31G(d). Red bars refer to Model 2, Blue bars to Model 1.

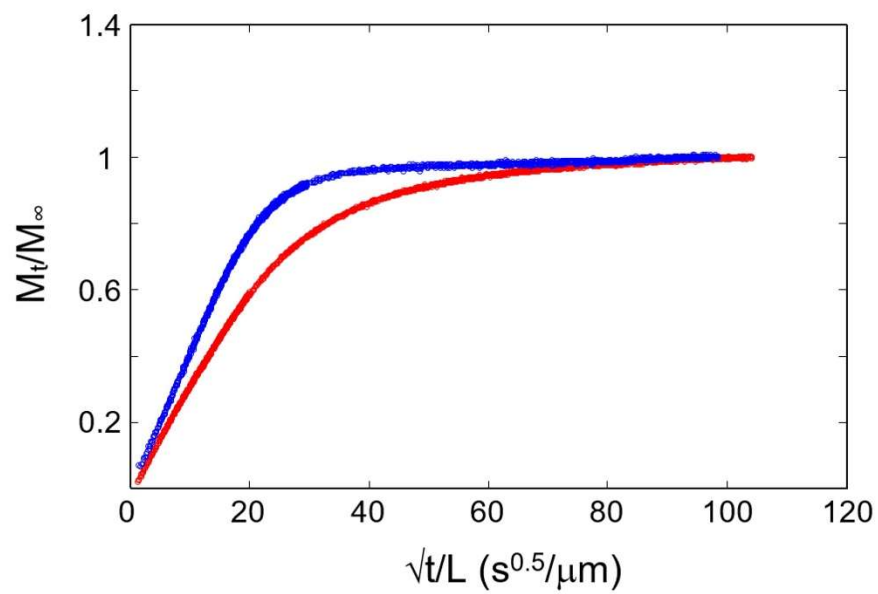


**Figure S13.** Sorption kinetics of methanol vapor in PBI at 25°C. Red dots: Integral test at  $p/p_0 = 0.05$  on a fully dried film. Blue dots: Integral test at  $p/p_0 = 0.05$  on a film containing 2.5 wt % of residual water.

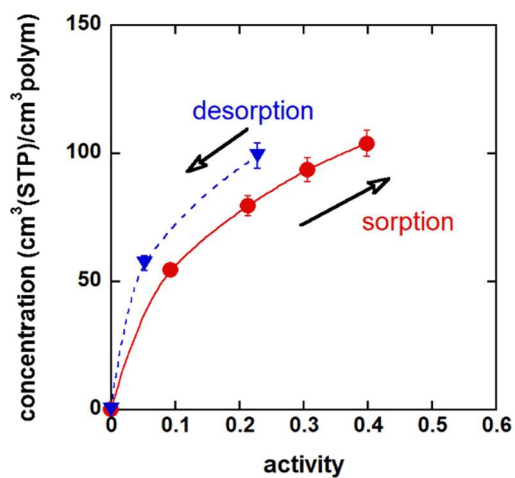


**Figure S14.** Barometric methanol sorption-desorption isotherm in PBI at 45°C.

## Publications, Oral Presentations, Awards

### Publications:

- V. Loianno, **K.P. Bye**, M. Galizia, P. Musto, *Plasticization mechanism in polybenzimidazole membranes for organic solvent nanofiltration: Molecular insights from in situ FTIR spectroscopy*, Journal of Polymer Science, 2020, 58, 2547-2560 (*invited contribution, selected as Journal cover page*).
- **K.P. Bye**, M. Galizia, *Fundamental origin of flux non-linearity in Organic Solvent Nanofiltration: Formulation of a thermodynamic/diffusion framework*, Journal of Membrane Science, 2020, 603, 118020
- **K.P. Bye**, V. Loianno, T.N. Pham, R. Liu, J.S. Riffle, M. Galizia, *Pure and mixed fluid sorption and transport in Celazole<sup>®</sup> polybenzimidazole: effect of plasticization*, Journal of Membrane Science, 2019, 580, 235-247
- M. Galizia, **K.P. Bye**, *Advances in organic solvent nanofiltration rely on physical chemistry and polymer chemistry*, Frontiers in Chemistry (Nature Publishing Group), 2018, 6, 511 (*invited Review*)

### Oral Talks & Poster presentations:

- **K.P. Bye**, *Fundamental Origin of Flux Non-Linearity in Organic Solvent Reverse Osmosis and Organic Solvent Nanofiltration*, **AIChE National Meeting**, S. Francisco, November 2020 (virtual oral talk)
- **K.P. Bye**, *Influence of molecular interactions, membrane swelling and plasticization on pure and mixed fluid transport in OSN membranes*, **NAMS Meeting**, Tempe, May 2020 (virtual poster presentation)
- **K.P. Bye**, *Influence of molecular interactions, membrane swelling and plasticization on pure and mixed fluid transport in OSN membranes*, **AIChE National Meeting**, Orlando, November 2019 (in person oral talk)

### Research Awards:

- NAMS Undergraduate Poster Competition Winner 2020
- NAMS Undergraduate Travel Award Grant Recipient 2020
- Al Clark Award for Undergraduate Research Recipient, University of Oklahoma 2020
- Outstanding Junior Researcher Award Recipient, University of Oklahoma 2019
- Phillips 66 Undergraduate Research Scholarship Recipient, University of Oklahoma 2019  
Undergraduate Research Opportunity Program funding recipient, University of Oklahoma 2018
- Astronaut Scholarship Finalist 2018

## **VITA**

### **Education**

University of Oklahoma, B.S. Chemical Engineering

- Graduated Summa Cum Laude, Cumulative GPA: 3.91
- Graduation Date: Spring 2020

University of Oklahoma, Accelerated M.S. Chemical Engineering

- Cumulative GPA: 4.0
- Anticipated Graduation Date: Spring 2021

### **Work Experience**

- Summer 2019: Process Engineering Internship at Renewable Energy Group
- Summer 2020: Process Engineering Internship at Burns and McDonnell
- Summer 2021: Full Rime Process Engineering Internship at Renewable Energy Group